Microfluidic high-content phenotypic screening on a *Caenorhabditis elegans* model

PAR

Maria Cristina LETIZIA

EPFL

ÉCOLE POLYTECHNIQUE
FÉDÉRALE DE LAUSANNE

Suisse
2018

Eva's only fault has been the one of wanting to know more, to experiment and search with her own sources the laws of the Universe and of her own body, and to refuse the teachings from "above". Eva, basically, represents the curiosity of science against the passive acceptance that belongs to faith.

— Margherita Hack

A mia madre e mio padre

Acknowledgements

I am tremendously grateful to all the people who have contributed - personally and professionally - to this Thesis. Firstly and foremost, I truly thank my supervisor Prof. Martin Gijs. Thank you Martin for hiring me, even if I had no previous experience in the field. I could not have made it tho this end without your constant technical and scientific guidance. Beside your precious and inspiring help during the different stages of my projects, I thank you for believing in me (often more than I could do!) and for always treating me with great humanity and respect, a quality that I strongly value in a supervisor. With your positive attitude and competence, you significantly contributed to make my PhD years this pleasant and stimulating. If ever I found myself managing a small group, I will try to be as professionally and personally supportive as you are. Thank you so much.

I am grateful to Prof. Carlotta Guiducci, Prof. Johan Auwerx, Prof. Marco Carminati and Prof. Andrew deMello, for accepting to read my Thesis, for their precious scientific criticism and their feedbacks.

I want to thank Melis for her help with all the possible administrative issues, for the French-Italian tandems, for the sincere chats and for being a friend. Despite being super busy, you have always found time to care about me.

I thank all the collaborators at Laboratory of Integrative Systems Physiology for helping me with the sample preparation and with the interpretation of the results. A special acknowledgment goes to Laurent, for turning biology into something I could understand, and to Vincenzo, for being so kind and always available to answer my questions and for introducing me to the power of "a' cazzimma" and "sta senza pensier".

I will never stop thanking Matteo, for his constant guidance during my PhD journey. I am grateful for the survival tricks and tips that you shared with me, thanks to which I eventually learned to stand on my own feet.

Thanks to all my past and present colleagues and friends at LMIS2, for being a fun and harmonious bunch of young scientists. I enjoyed hanging out with you, especially when nobody - including me - had to pretend to be smart 😄. I will miss our time together. A special thought to Roger and Baris, my fitness and chill-time buddies, for getting together where we needed to be. I also thank Tuan and Li, probably the most genuine and adorable weirdos I know, for the nice open-hearted chats and for offering their help many times. A very special acknowledgment goes to Raphaël, for his incredible patience

Acknowledgements

and countless help in revising most of my scientific works. He is a great scientist and person, I wish him all the best.

I thank all the friends I met in Lausanne in the last four years, especially Giulia, Enrica, Enrica, Laszlo, Rima, Aldo, Andrea, Annalisa, Pietro, Diego, Saska, Matteo and Svarricchio. You all left something memorable that I will always bring with me. I thank my friend Barbara, for making our weekend-train-trips something to wait for and for our "confessions" during the several pizza-beer evenings spent together.

I thank my lovely/grumpy friend Alessandra, for always staying in touch with me and for understanding so naturally even the latent aspects of my personality. I am tremendously grateful to my "polibavaglino" friends spread over Europe: "cu è riccu d'amici è poveru di guài". Vi voglio bene.

I truly thank the most extraordinary women (and brilliant scientist as well!) I met in this journey, Rima, Enrica and Enrica, for their authentic friendship and the uncountable laughs out of the blue. Each in a different way, you showed me how to spot light where anyone else would only see darkness. You probably don't realize how great you are. My Lausanne years would not have been this pleasant and remarkable without you.

Grazie a Fulvio e Stefania per essersi presi cura di me, specialmente durante la scrittura della tesi, e per avermi fatto sempre sentire di casa. Grazie per aver sinceramente gioito con me anche dei più piccoli successi.

I thank my brother Marco, who agreed to share his flat with his little sister. Thank you, Marco, for showing me how important it is to be committed and believe in what you do. Believe it or not, I also thank you for bringing entropy in our apartment, that otherwise would have been too clean and boring.

Un gigantesco grazie ai miei genitori, Paola e Nino (Pino), le persone più generose al mondo, per avermi aiutata e supportata, ovunque io fossi. Grazie per le valigie cariche di coccole (diciamo così...), grazie a cui io e Marco ci siamo sempre sentiti come a casa. Grazie Pino, per avermi trasmesso un po' della tua vena artistica e del tuo vivere con freschezza. Grazie mamma per non avermi mai detto "brava" e per avermi insegnato a non accontentarmi mai. "Cu zappa, zappa a so' vigna. Cu bonu a zappa, bonu a vinnigna". Grazie a nonna Marghe, la vera scienziata della famiglia, per il tuo amore infinito. Grazie anche per i maglioni caldi fatti con amore per sopravvivere nella fredda Svizzera e per avermi insegnato proverbi siciliani per ogni occasione. Trovarvi tutti a casa nei fine settimana a Milano è stata una gioia impagabile.

My deepest gratitude goes to Luca. You are my extra pair of shoulders and thanks to your positive leverage, today I believe in myself and I barely know what stress is. Thank you for your arms always open for me, through which you keep bringing sparkling joy to my life. You are my sunshine.

Lausanne, 19 Mars 2018   Cristina

Abstract

Caenorhabditis elegans is a performant model system for studying human biological processes and diseases and for pre-clinical phenotyping screenings of compounds. Microfluidics has been instrumental in enabling *C. elegans*-based drug assays, facilitating the worm handling and bringing robust and reproducible analysis protocols. In this Thesis, I present phenotypic assays on *C. elegans*, enabled by microfluidic devices conveniently designed.

First, I propose a strategy to track different phenotypic traits of individual worms over their life-cycle. Phenotypes - as duration of the different developmental stages, length, diameter and fluorescent stress response at each developmental stage, fertility and sex fate - were quantified for each animal, resulting in high-content phenome data. The method was validated by analyzing the worm response to pharmacological and genetic compounds known to activate mitochondrial stress-response pathways in different species. Interestingly, the analysis revealed specific sub-populations that allowed separating single worms as responders or non-responders to a treatment, thereby elucidating pharmaceutical or therapeutic responses still overlooked.

Second, I propose a design-of-experiment approach to characterize the concentration-dependent effect of the drug doxycycline on the duration of *C. elegans* development. 13 experiments were performed following a Doehlert design, where different doxycycline concentrations were tested, while varying also temperature and food amount, which are known to influence the duration of the *C. elegans* development. A microfluidic platform was designed to test the doxycycline effect on isolated worms, with full control of temperature and feeding over the development. Our approach allowed maximizing the understanding of the effect of this antibiotic on the *C. elegans* development and paving the way towards a standardized and optimized drug testing process.

Third, envisioning a platform where *C. elegans* on-chip feeding is fully controlled and food consumption could be quantified as additional phenotype, I describe a method to measure the concentration of solutions of *Escherichia coli* bacteria. I designed an opto-electronic device that was integrated with and optically aligned to a microfluidic chip. The absorbance of a bacterial solution was calculated according to the Lambert-Beer's law. The device was tested and calibrated, obtaining a linear relation between the absorbance and the concentration of the solutions. Afterwards, the change of the turbidity of the solution on the long-term was assessed. Based on our observations, a

Abstract

simple mathematical model for the change of absorbance over time was hypothesized.

In another study I performed a motility-based phenotypic assay on *C. elegans*, to quantify the worm glucose uptake. Adult worms were isolated in a micro-chamber, a glucose solution was injected and short videos were recorded, from which a motility score was extracted.

Last but not least, in the frame of a collaborative project, I designed a 3D-printed micro-channel to immobilize a single adult worm to perform metabolic phenotyping on a worm subsection via nuclear magnetic resonance spectroscopy.

Envisioning a pivotal role for *C. elegans* in the drug screening pipeline, a unique microfluidic platform, integrating all the phenotypic assays described in this Thesis, would allow for robust, fast and cost-effective high-content screenings of compounds on this simple yet powerful model system.

Keywords: *Caenorhabditis elegans*, microfluidics, lab on chip, phenotype, phenotypic assay, high-content screening, heterogeneity, design of experiment, *Escherichia coli*, absorbance, nuclear magnetic resonance, microfabrication, SU-8, soft lithography, PDMS

Résumé

Caenorhabditis elegans est un modèle animal idéal pour l'étude des processus et maladies de la biologie humaine mais aussi pour le criblage préclinique de nouvelles molécules. La microfluidique a joué un rôle déterminant dans la mise au point de tests pharmaceutiques basés sur *C. elegans* en facilitant leur manipulation et l'établissement de protocoles d'analyse robustes et reproductibles. Dans cette Thèse, je présente des dispositifs microfluidiques conçu spécifiquement pour le criblage phénotypique de *C. elegans*.

Premièrement, je décris une stratégie pour suivre les différents traits phénotypiques individuels des nématodes au long de leur cycle de vie. Ces marqueurs - la durée des différentes étapes du développement, la longueur, le diamètre et la réponse au stress à chaque stade de développement, la fertilité et le sexe - ont été quantifiés pour chaque animal, résultant en une description à haute densité du phénome. La méthode a été validée en analysant la réponse des nématodes à des traitements pharmacologiques et génétiques connus pour activer les voies mitochondriales de réponse au stress chez différentes espèces. L'analyse a révélé des sous-populations spécifiques qui ont permis de séparer les vers en répondeurs ou non-répondeurs à un traitement,suggérant de nouvelles réponses pharmacologiques ou thérapeutiques.

Deuxièmement, je propose une approche expérimentale pour caractériser l'effet de la doxycycline sur la durée du développement de *C. elegans*. 13 expériences ont été réalisées en suivant un plan de Doehlert pour tester différentes concentrations de doxycycline. Les effets de la température et de la quantité de nourriture, dont l'influence sur la durée du développement de *C. elegans* est connue, ont aussi été étudiés. Une plateforme microfluidique a été conçue pour tester l'effet de la doxycycline sur le développement de vers isolés, avec un contrôle total de la température et de l'alimentation. Notre approche a permis d'améliorer notre compréhension de l'effet de cet antibiotique sur le développement de *C. elegans* et ouvre la voie vers un processus normalisé et optimisé de criblage.

Troisièmement, une méthode pour mesurer la concentration de solutions de bactéries *Escherichia coli* est développée en préparation d'une plate-forme où l'alimentation des vers est entièrement contrôlée et quantifiée comme phénotype supplémentaire. J'ai conçu un dispositif optoélectronique qui a été intégré à un puce microfluidique. L'absorbance d'une solution bactérienne a été calculée selon le Lambert-Beer loi. L'appareil a été testé et calibré, obtenant une relation linéaire entre l'absorbance et la concentration en bactéries des solutions. Ensuite, le changement de la turbidité de la solution sur le long

Résumé

terme a été évalué. Sur la base de nos observations, un modèle mathématique simple pour le changement de l'absorbance dans le temps a été émis.

Dans une autre étude, j'ai réalisé un test phénotypique basé sur la motilité de *C. elegans*, pour quantifier l'effet du glucose. Des vers adultes ont été isolés dans une micro-chambre, une solution hautement concentrée en glucose a été injectée et de courtes vidéos ont été enregistrées, à partir desquelles un score de motilité était extrait.

Enfin dans le cadre d'un projet collaboratif, j'ai conçu des microcanaux par impression 3D pour immobiliser un seul ver adulte. Un phénotypage métabolique sur une section du ver a ensuite été réalisé par spectroscopie de résonance magnétique nucléaire.

En envisageant un rôle central pour *C. elegans* dans les tests pharmaceutiques, une unique plate-forme microfluidique intégrant tous les tests phénotypiques décrits dans cette thèse permettrait un criblage à haute densité robuste et rentable sur ce modèle animal simple mais puissant.

Mots-clés : *Caenorhabditis elegans*, microfluidique, laboratoire sur puce, phénotype, test phénotypique, criblage à haut contenu, hétérogénéité, plan d'expérience, *Escherichia coli*, absorbance, résonance magnétique nucléaire, microfabrication, SU-8, lithographie, PDMS

Sommario

Il nematode *Caenorhabditis elegans* rappresenta un ottimo modello per lo studio di alcuni processi e malattie della biologia umana e per screening fenotipici di molecole a livello pre-clinico. La microfluidica è stata una disciplina determinante nel testare molecole e composti chimici sul *C. elegans*, perchè rispetto ai tradizionali protocolli sperimentali manuali, consente di automatizzare gli esperimenti, rendendo le conseguenti analisi robuste e riproducibili. In questa Tesi, presento diversi saggi fenotipici svolti su *C. elegans*, resi possibili dallo sviluppo *ad hoc* di diversi chip microfluidici.

In primo luogo, presento una strategia per monitorare diversi fenotipi di singoli animali durante il loro ciclo di vita. Fenotipi - come la durata delle diverse fasi di sviluppo, la lunghezza e il diametro degli animali, la risposta allo stress per ogni fase di sviluppo, così come fertilità e determinazione del sesso - sono stati quantificati per ciascun animale, ottenendo così un set di dati fenoticipi "high-content", cioè ad alto contenuto informativo. Questo metodo è stato validato analizzando la risposta degli animali a composti sia farmacologici sia genetici, noti per attivare in altre specie risposte biologiche accomunate da stress a livello mitocondriale. L'analisi ha rivelato la presenza di sotto-gruppi, che hanno permesso di classificare i singoli nematodi come reattivi o non-reattivi al trattamento, chiarendo così alcuni meccanismi farmacologi e terapeutici finora ignorati.

In secondo luogo, presento un "design of experiment", ovvero un piano di esperimenti pensati *ad hoc*, per studiare come il tempo di sviluppo del *C. elegans* vari in funzione della dose dell'antibiotico doxiciclina. Abbiamo condotto 13 esperimenti secondo un "design of experiment" di tipo Doehlert, in cui sono state somministrate diverse dosi di doxiciclina, variando allo stesso tempo anche la temperatura e la quantità di nutrimento, due fattori noti per influenzare a loro volta il tempo di sviluppo del *C. elegans*. È stata progettata una piattaforma microfluidica per testare l'effetto della doxiciclina su nematodi isolati, con pieno controllo della temperatura e della quantità di nutrimento. Il nostro approccio ha permesso di massimizzare la comprensione dell'effetto di questo antibiotico sullo sviluppo del *C. elegans* e pone le basi per futuri protocolli standardizzati e ottimizzati per testare farmaci.

In terzo luogo, immaginando una piattaforma microfluidica in cui l'alimentazione del *C. elegans* sia completamente controllata e in cui il consumo di cibo possa essere quantificato come ulteriore fenotipo, presento un metodo per misurare la concentrazione di soluzioni di batteri *Escherichia coli*, di cui questi nematodi si nutrono. Ho progettato un dispositivo

opto-elettronico integrato e otticamente allineato con un chip microfluidico. L'assorbanza della soluzione è stata calcolata in base alla legge di Lambert-Beer. Il dispositivo è stato testato e calibrato, ottenendo una relazione lineare tra l'assorbanza e la concentrazione delle soluzioni. In seguito ci siamo chiesti come la turbidità della soluzione vari nel lungo termine e, sulla base di risultati sperimentali, è stato ipotizzato un semplice modello matematico per il cambiamento di assorbanza nel tempo.

In un altro studio ho eseguito un ulteriore saggio fenotipico basato sulla motilità dei *C. elegans*, utilizzata come parametro per quantificare l'assorbimento del glucosio da parte dei nematodi. *C. elegans* adulti sono stati isolati in una micro-camera, una soluzione di glucosio è stata somministrata e sono stati quindi registrati brevi video da cui è stata quantificata la motilità dei *C. elegans*.

Ultimo ma non meno importante, nel quadro di un progetto collaborativo, ho progettato un microcanale, in seguito fabbricato con un' innovativa stampante 3D, per immobilizzare un singolo nematode adulto, al fine di estrarre fenotipi di tipo metabolico, tramite spettroscopia di risonanza magnetica nucleare.

Immaginando un processo di screening dei farmaci in cui il *C. elagans* sia un modello chiave e insostituibile, una piattaforma microfluidica comprensiva di tutti i test fenotipici descritti in questa tesi, aprirebbe la strada a screening veloci, affidabili ed economici.

Parole chiave: *Caenorhabditis elegans*, microfluidica, lab on chip, fenotipo, saggio fenotipicp, screening "high-content", eterogeneità, "design of experiment", *Escherichia coli*, assorbanza, risonanza magnetica nucleare, microfabbricazione, SU-8, soft-litografia, PDMS

Contents

Contents

List of Figures

List of Tables

1 Introduction

1.1 *Caenorhabditis elegans* as a model system

Caenorhabditis elegans (*C. elegans*) has become an attractive model in biological research since the early 1960s, when Dr. Sydney Brenner realized that fundamental questions about cellular differentiation and interaction, as well as organ development, could not be answered by studying either simple unicellular model organisms, e.g. bacteria, or too complex and higher-order animals, e.g. mammals. A genetically amenable and multicellular model organism simpler than mammals, was therefore needed. The ideal solution proved to be the roundworm *C. elegans*, a 1 mm-long nematode, with short development time and life span, and transparent: the phenomena of cellular differentiation and organ development could be finally followed in a quasi real-time fashion, directly under the microscope.

Dr. Brenner's publication in 1974 appointed *C. elegans* as a novel experimental model organism [1]. By establishing and using the nematode *C. elegans* as an experimental model system, possibilities were opened to follow cell division and differentiation from the fertilized egg to the adult. Sydney Brenner, together with John Sulston and Robert Horvitz, won the Nobel Prize in Physiology or Medicine in 2002, for having exploited *C. elegans* to investigate key genes regulating organ development and programmed cell death, and having shown that corresponding genes exist in higher species, including human.

Since then, this animal has never lost his charm and it is nowadays a powerful model for biological research. *C. elegans* has a short life cycle development (~ 3 days) from egg to adult and a relatively short life span of around 2 weeks, which makes this animal a very convenient model to investigate developmental processes and aging. Its neuronal circuitry has been mapped and its genome completely sequenced. Moreover, in the laboratory environment *C. elegans* primarily feeds on *E. coli* bacteria, which can be manipulated to express double-stranded RNA for the gene of interest. This represents a powerful technique for gene silencing and investigation of loss-of-function phenotypes

[2]. Furthermore, *C. elegans* shares many biological features with humans, such as the development of muscles, nerves, digestive tract, production of eggs and sperm. *C. elegans* and humans also share a high number of genes - 40% of worms' genes have their human counterpart - and molecular pathways [3]. Transgenic and mutant worms contribute to modeling Alzheimer's, Parkinson's and Huntington's diseases and to the discovery of compounds that can treat these neurodegenerative diseases [4], [5]. Moreover, these nematodes are transparent during all stages of embryonic and larval development, which enables the observation of cells and organs development, as well as the visualization of gene expression and signaling pathways, also thanks to the availability of a large number of fluorescent reporter-gene strains. *C. elegans* worms are predominantly hermaphrodite, with males making up approximately 0.1% of wild-type populations. Hermaphrodite adults have 959 somatic cells and their complete lineage is known [6]. This nematode has one of the simplest and - by far - the best characterized nervous systems [7]. However, despite this simplicity, both physiological behaviors – e.g. feeding, locomotion, egg-laying – as well as complex behavioral traits – e.g. sensory responses, social behaviors, learning – can be observed and studied in worms. For all these "natural gifts", *C. elegans* is a powerful tool for drug discovery and for the understanding of the molecular and genetic mechanisms underlying certain human diseases.

Generally, in a drug discovery process, thousands of chemicals with a disease relevance are tested to find so-called leads, *i.e.* small molecules with potential for drug development (Figure 1.1) [8]. The first step is usually performed *in vitro*, using either a biochemical assay or a cell-based assay. The former consists in investigating the interaction of a compound with an isolated target in an *in vitro* environment. On the other hand, the cell-culture approach allows a more realistic interaction in a more physiological environment [9]. Afterwards, preclinical testing of a drug in animal models is performed, providing valuable data on the expected clinical performance of the drug [10]. Phenotypic assays are developed by modeling a human disease in an animal model through genetic manipulation, such as mutation of human disease gene orthologs, transgenic expression of human disease genes, or gene knockout [9]. This phase, usually lasting about 2.5 years, allows narrowing the number of compounds to a few molecules. About 6 years of clinical trials are performed on humans, before the successful molecule is finally selected.

In this drug screening scenario, *C. elegans* is an excellent candidate for whole animal-based high-throughput screening and would nicely feed the drug discovery pipeline, between cell-based assays and tests on rodents (Figure 1.2). In fact, its ability to mimic human disease cannot be reproduced by *in-vitro* or cellular-based models, and offers higher chances of identifying drugs that will ultimately be more efficacious in humans; moreover, being a whole organism, it allows evaluating simultaneously the drug efficacy, toxicity, absorption and distribution, and offers a broad range of scorable phenotypes; furthermore, the availability of genetic tools as RNAi feeding library simplifies the identification of drug targets [11]. Finally, the maintenance costs of *C. elegans* are orders of magnitude lower than the ones related to rodents, and the use of *C. elegans* in drug screening processes does not raise ethical concerns.

10'000 molecules

DISCOVERY
High-throughput
screening

5 years

250 molecules

PRECLINICAL
Laboratory and
animal testing

2.5 years

5 molecules

PHASE I CLINICAL TRIAL
20-100 volunteers.
Safety and dosage

1.5 years

PHASE II CLINICAL TRIAL
100-500 volunteers.
Efficacy and side effects

2 years

PHASE III CLINICAL TRIAL
1000-1500 volunteers.
Long-term use

2.5 years

1 molecule

FDA REVIEW

Figure 1.1 – An overview of the typical drug development pipeline. Starting with several thousands of molecules, the first 5 year-long step allows selecting about 250 molecules, typically by performing high-throughput screening *in vitro*, using either biochemical assays or cell-based assays. Afterwards, preclinical testing of a drug on animals is performed, providing valuable data on the expected clinical performance of the drug. After this 2.5 year-long phase, the number of compounds is narrowed down to a few molecules. Afterwards, about 6 years of clinical trials are performed on volunteers, until the successful molecule is finally selected for Food and Drug Administration (FDA) approval.
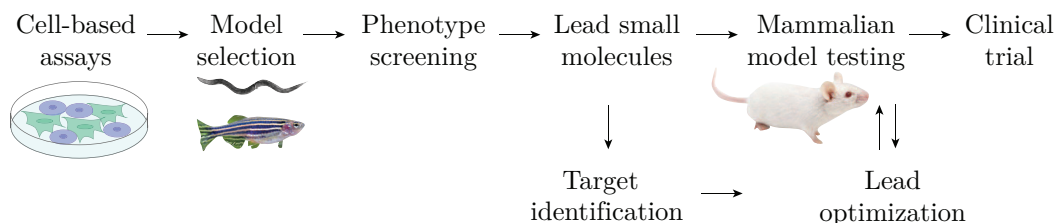
Figure 1.2 – Strategy for phenotype-based drug discovery. In phenotype-based assays in small models such as *C. elegans*, no *a priori* knowledge is required about the mechanisms underlying a disease process. In these phenotypic assays, a human disease is mimicked on a simple animal model. Once an assay is established, compounds are screened manually or by high-throughput methods. Once potential lead molecules are identified, genetic, biochemical and computational approaches can be iteratively applied to find the drug target and optimize lead molecules on rodents, before moving to clinical trials. Figure adapted from [12].

Traditionally, *C. elegans* is maintained in laboratories on nematode growth medium (NGM) agar poured into petri dishes. Plates are seeded with *E. coli* bacteria to feed worms. However, traditional *C. elegans* maintenance is tremendously tedious and time-consuming, because most of the procedures are performed manually by a laboratory technician [13]. For example, to avoid worms crawling and starvation, worms need to be daily transferred to NGM plates with fresh and abundant bacteria: the most common method is to manually pick single animals by using a worm picker and transfer them to the new fresh plate. Moreover, if the assay requires only worms of a precise age, worm synchronization is necessary. In this case, worms of the desired stage are picked and transferred in a new plate and cultured. As alternative, the un-synchronized population can be immersed in a solution of bleach and caustic soda, which is lethal for all the population except the embryos, which are protected by the egg shell: those surviving embryos will be placed in a fresh plate and, once they hatch, the newborn synchronized larvae will be cultured.

Beside the risk of damaging or killing the animals, traditional well-plate-based drug tests present many limitations. In fact, when the drug of interest is spotted on the NGM plate, an unknown amount of the compound is absorbed by the agar, making the worm exposure to the drug difficult to determine and the experiments poorly reproducible. Moreover, NGM-based approaches strongly limit precise spatio-temporal control of the administered drug. This limitation becomes particularly severe when a dose-test needs to be performed, as tuning the drug concentration to the worm response becomes extremely time-consuming and requires repetitive manual worm transfer in different NGM plates previously prepared with the different drug doses to test.

In order to improve the understanding of a disease, its therapeutic targets, the mechanisms of action of a compound on *C. elegans*, alternative interdisciplinary approaches should be used, which make the drug testing process on *C. elegans* more robust, more reproducible, less costly and less error-prone. During the last decade, more technological approaches towards the automation of *C. elegans* culture and quantification of phenotypes

have been presented. In this direction, many well-based approaches were developed [9], [11]. A pioneering approach for large-scale screening of drugs using *C. elegans* was proposed in 2006 [14]. Worm manipulation was automated using the COPAS BIOSORT instrument (Union Biometrica, US), and over 14 thousands of compounds were screened. Semi-automated image acquisition was performed and phenotypes such as growth, lethality, motility and other morphological features were identified. Despite this approach allowed the identification of about 300 active molecules, it was limited by the visual scoring of the phenotypes and by the fact that the assays were performed on well-shaped agar plates [14]. The same year, an agar-free approach was described, where *C. elegans* nematodes were cultured in liquid-filled in well-plates, allowing automated handling by pipetting robots [15]. Avoiding the use of agar plates left place to the use of robotic worm handlers and to more automated imaging platforms. This approach, however, was limited to the larval 1 (L1) worm size. A more automated screening process, featuring automated worm transfer, image acquisition and data analysis was published in 2010 [16]. However, this approach, successfully used to quantify protein accumulation into the worm intestine, required rather expensive laboratory equipment: animals were sorted using the COPAS BIOSORT, and a dedicated high-content screening instrument was subsequently used to automatically capture images and another to perform automated data analysis. An alternative method for worm sorting was based on the so-called live-animal fluorescence activated cell sorter (laFACS), that allowed to sort worms according to the fluorescent measured signal [17]. Beside sorting, fluorescent signals were also used as phenotypic read-outs performed on worms in 1536-well plates [18]. However, a plate reader was used to measure the overall fluorescence signal in the well, but no images were captured.

Beside requiring expensive machines, most of these approaches were conceived for cells analyses, and imaging and data analysis could not be easily adapted to *C. elegans* applications. Moreover, worms in liquid environment are highly motile and therefore inherently more challenging to image. Another limitation resides in the fact that worms in liquid media tend to settle to the micro-well bottom, which makes robotic pipetting and worms transfer challenging.

Microfluidics platforms have been recently emerged as powerful tool for phenotyping screening on *C. elegans* [9], [19]–[21]. Microfluidic chips can easily be set up with standard microscopy instruments. Moreover, micro-channel dimensions matching worm size facilitate precise handling of the nematodes. Worms can be easily loaded into the device by injecting a worm suspension in a buffer medium - typically M9 or S medium - and sorted based on their size [22], [23]. This automatic manipulation allows for realizing reproducible experimental conditions, contrasting with the traditional manual manipulation performed by biologists, which is laborious, time-consuming and leads to the risk of damaging worms while handling [24]. Moreover, microfluidic technology allows controlled flow and precise chemical stimuli delivery [25]. It is possible to test a new compound or the same compound at a new concentration on the same worm population in the chip, just by washing away the previous compound and injecting the new one. One of the most important applications of microfluidics has been high-throughput automated

screening of worm populations, as it can greatly reduce the time required to study each worm and allows collecting a great amount of data [26]. Multiple output parameters can be monitored per experiment on the long term. Moreover, image processing tools enable automation and reduce human bias; they are vital to handle the data collected in many experiments.

1.2 Microfluidic systems, an overview

Lab-on-chip microfluidic systems potentially allow shrinking an entire laboratory to a chip, enabling the implementation of analytical protocols using low reagent volumes, short processing times, in a flexible way and potentially at low cost. During the past two decades, microfluidic systems have been developed rapidly and have contributed to the development of many clinical and molecular diagnostic instruments [9], [27]–[30]. There are several advantages of scaling down standard laboratories devices from the decimeter scale to the 100 μm scale. Micro-channel height and width being in the micrometer scale, microfluidic devices consume very low fluid volumes, therefore requiring less reagents and related costs, and producing less waste. A linear reduction by a factor of 10^3 translates to a volume reduction by a factor of 10^9: instead of handling 1 L or 1 mL, a microfluidic system could easily work with volumes down to 1 nL or 1 pL. Such small volumes allow for very fast analysis, efficient detection protocols, which becomes particularly advantageous when large amounts of sample are unavailable. Thanks to the small channel size, microfluidic chips can have high compactness, which opens the possibility for massive chip parallelization and for high-throughput analyses [31]. Moreover, with channel dimensions matching a biological's sample size, microfluidic devices have allowed the manipulation of biological entities as small as a cell, paving the way for safe platforms for chemical or biological studies, where a multitude of functions can be integrated and automated [28], [31].

Interestingly, the interplay between many different forces and the change of the relative importance of these forces in the micro-regime as compared to the macro-regime, need to be taken into account [27]. Surface effects that often can be neglected at the macro-scale become increasingly dominant in microfluidic circuits. From a physics point of view, liquid phenomena such as laminar flow, fluidic resistance, diffusion and capillary forces become dominant at the micrometer scale and need to be considered in the design of a microfluidic device.

The flow regime is characterized by the Reynolds number Re, which is the ratio of inertial forces to viscous forces, defined by Equation 1.1, where v is the mean flow velocity, D is the channel diameter, ρ is the fluid density and μ is the fluid viscosity [32].

$$Re = \frac{vD\rho}{\mu} \tag{1.1}$$

Re helps predicting the flow pattern. If $Re < 2000$, a laminar flow profile is observed, while turbulences and inertial forces dominate for higher *Re* [33]. Typically, due to the small dimensions of a micro-channel, $Re \ll 100$, which makes the flow pattern predictable and allows the transport of biological entities in a very controlled and deterministic way. In a Poiseuille flow regime, the fluid is driven through a long, straight and rigid channel by imposing a pressure difference ΔP between the two ends of the channel. The average flow rate Q of a liquid within a micro-channel is proportional to the imposed pressure difference, according to Equation 1.2

$$Q = \frac{\Delta P}{R},\tag{1.2}$$

being R the fluidic resistance of the channel [27]. For straight rectangular channels with width w and height h, when $h < w$, the fluidic resistance is given by the Poiseuille Equation 1.3:

$$R = \frac{12\mu L}{1 - 0.63\dfrac{h}{w}}\frac{1}{h^3 w}.\tag{1.3}$$

Beside pressure gradients, another interesting aspect of the device operations is the passive motion of particles in presence of a concentration gradient *via* Brownian motion, known as diffusion [27], [31]. The velocity of the spherical diffusing particle is given by the diffusion constant D, which is defined by Einstein Equation 1.4

$$D = \frac{k_B T}{6\pi r \mu},\tag{1.4}$$

where k_B is the Boltzmann's constant, T is the temperature in Kelvin and r is the radius of the diffusing particle. In a time interval t, the root mean square distance l travelled by a particle is given by Equation 1.5

$$l = \sqrt{2Dt}.\tag{1.5}$$

Consequently, in the same time interval t and in absence of an external force field, small molecules can travel longer distances than large molecules.

Furthermore, microfluidic chips have intrinsically larger surface-to-volume ratio, due to the small length scale of the channels [27], [31]. Such larger surface area can be exploited to increase the rate of heat and mass transfer. Moreover, the large surface-to-volume ratio makes capillary forces and surface tension more dominant phenomena in micro-channels.

From an engineering point of view, a microfluidic system is made of a set of operation units, such as fluid transport, metering, mixing, particle separation/concentration *etc*, each of which is committed to a building block. In fact, a microfluidic system normally

consists of micro-channels for sample transportation and active elements to manipulate the sample, such as pumps, valves, mixers, separators/concentrators [31], [34].

Pumping strategies usually rely on mechanical pressure, electro-osmotic force, heat transfer, electro-wetting, *etc.* As an alternative, passive microfluidic systems exist, where fluid is driven by forces such as gravity, capillary action, absorption or pressure generated by manual action [35].

Microvalves are widely used to regulate and control the activation of flow, as well as to seal samples [31], [36]. If microvalves include a moving part actuated by magnetic, electric, piezoelectric or thermal actuation methods, they are classified as active, as opposed to passive microvalves. The formers are usually complex and costly, as they require external equipment. The latters - on the other hands - are simpler and easy to miniaturize and integrate in the fluidic system. Passive microvalves can have moving parts that open in response to a forward flow or can simply rely on channel geometry and capillary forces [36].

Micromixers are other important fluidic components, which usually rely either on particle diffusion or on chaotic advection [31], [37]. Chaotic advection can significantly improve mixing and it is achieved by breaking the flow pattern by inserting obstacles or structures in the micro-channel [38]. Other micromixers are instead actuated by external energy inputs, including electrokinetic, acoustic, magnetic sources or integrated micropumps and microvalves [31].

1.3 Thesis outline

In this Thesis, I present different phenotypic assays on *C. elegans* nematodes that were enabled by the use of microfluidic devices that I opportunely designed. The state of the art related to each phenotypic assay is provided in the introductory part of each corresponding Chapter.

In the technology-oriented Chapter 2, I illustrate the fabrication of the microfluidic devices that I designed. Briefly, the chip layout was transferred to a photomask, that was later used to transfer the pattern on SU-8 photoresist coated on a silicon wafer. Such a wafer was then used as a mold to obtain in a further step a polydimethylsiloxane (PDMS)-glass microfluidic device. The last part of Chapter 2 gives an illustration of the setup that I assembled and used to perform the experiments described in the following Chapters.

In Chapter 3, I describe a new strategy to track different phenotypic traits of individual *C. elegans* nematodes throughout their full life-cycle – *i.e.* their embryonic and post-embryonic development. Phenotypes - such as duration of the different stages of development, length, diameter and fluorescent stress response at each stage of development, fertility and sex fate - were monitored and quantified for each animal, resulting in high-content phenome data at single-worm resolution.

In Chapter 4, a design-of-experiment approach to characterize the concentration-dependent effect of the drug doxycycline on the duration of *C. elegans* development is proposed. To cover the experimentation space, 13 experiments were designed and performed following a 3-factors Doehlert design, where different doxycycline concentrations were tested, while varying also temperature and food amount, which are known to influence the duration of the *C. elegans* development. We designed a microfluidic platform to isolate and culture *C. elegans* larvae, while testing the doxycycline effect with full control of temperature and feeding over the entire development.

Envisioning a microfluidic platform where *C. elegans* on-chip feeding is fully controlled and food consumption could be quantified as additional phenotype, I propose a method to measure the concentration of solutions of *Escherichia coli* bacteria, which is described in Chapter 5. I designed an opto-electronic device that was integrated with and optically aligned to a microfluidic chip. The absorbance of a bacterial solution was calculated according to the Lambert-Beer's law. The device was tested and calibrated with different bacterial solutions of known concentration, obtaining a linear relation between the absorbance and the concentration of the injected solutions.

In another study, described in Chapter 6, I measured *C. elegans* motility as a parameter to quantify the glucose uptake, upon exposure to either a high glucose concentration or to the molecule dynasore. For this purpose, I isolated adult worms in a microfluidic chamber, I injected the compound under investigation and recorded short videos, from which a motility score was extracted for each tested condition.

Last but not least, in the frame of a collaborative project, I designed a 3D-printed micro-channel to trap and immobilize a single adult *C. elegans* to perform metabolic phenotyping on a worm subsection via nuclear magnetic resonance spectroscopy. These results are presented in Chapter 7.

Finally, in Chapter 8, I summarize this work and provide a future outlook, envisioning microfluidic-based phenotypic screenings on *C. elegans* as a pivotal step in the drug screening pipeline.

2 Fabrication of microfluidic devices and experimental setup

Abstract This Chapter illustrates the fabrication of the microfluidic devices that I designed. Briefly, for all the designs, the chip layout was transferred to a photomask, that was later used to transfer the pattern on SU-8 photoresist coated on a silicon wafer. Such a wafer was then used as a mold to obtain in a further step a PDMS-glass microfluidic device.

The fabrication of the different photomasks and molds was carried out at the Center of MicroNanoTechnology, at EPFL. The fabrication and assembling of the microfluidic chip was performed using the Laboratory of Microsystems facilities.

In the last part of the chapter, I describe the microfluidic setup that was conceived, assembled and used to perform the experiments described in Chapters 3, 5, 6 and 7.

In order to perform the experiments described in Chapter 4, a dedicated setup was designed, which is detailed in Section 4.3.1.

2.1   Mask fabrication

The layout of the microfluidic chip was designed by using the computer-aided design software Clewin. The photomask fabrication was carried out at EPFL Center of Micro-NanoTechnology (CMi). A 5"×5" blank mask made of a transparent glass plate covered by a layer of chromium and chromium oxide and by a layer of positive photoresist on top (sketch in Figure 2.1a) was used. First, a high-speed pattern generator (VPG200, Heidelberg, Germany) transferred the design pattern by rastering the mask surface with a high-power laser beam (λ=355 nm) that opportunely exposed the photoresist (Figure 2.1b), that was then developed (developer AZ351B, Clariant, Germany) and rinsed (Figure 2.1c). The remaining photoresist pattern acted as a mask during subsequent wet etching in an acid/oxidizer solution of the chromium layer (Figure 2.1d), which was consequently removed, leaving on the glass plate transparent windows replicating the initial pattern. Finally, the layer of non-exposed photoresist was stripped (Figure 2.1e) in a butyrolactone solution.
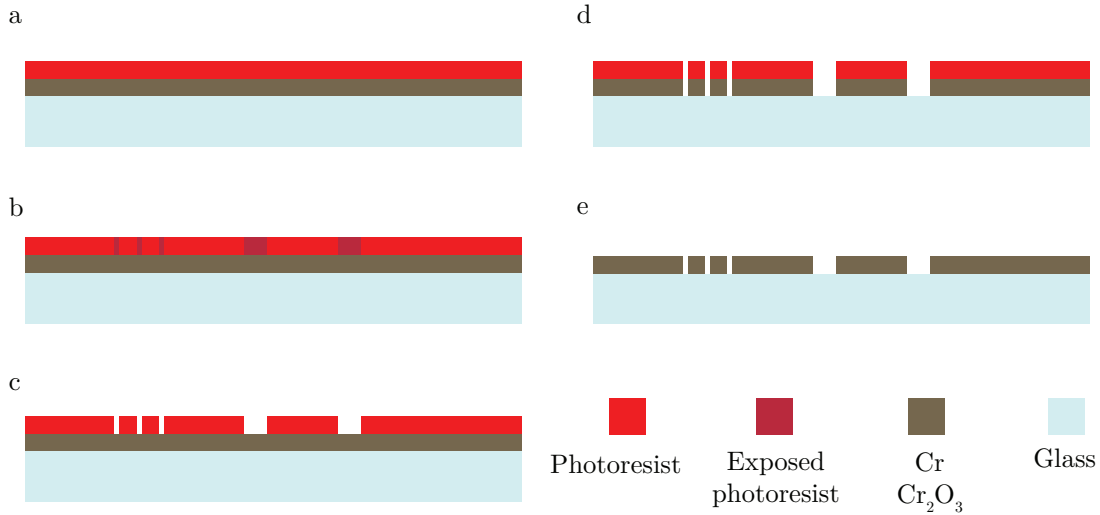
Figure 2.1 – Schematic of the process-flow to fabricate of a photomask. a) 5"×5" photomask made of a transparent glass plate and a thin layer of chromium and chromium dioxide, covered with positive photoresist. b) A high-power and high-speed laser source (λ=355 nm) exposes the photoresist, transferring a design previously made. c) The exposed photoresist is developed and rinsed. d) The chromium layer is etched, transferring in this way the design on the glass plate. e) The photoresist is removed by stripping.

2.2   Mold fabrication

The microfluidic devices presented in Chapters 3, 4, 5 and 6 were fabricated starting from a silicon mold (100/p/ss/0.1-100, single-side polished 10 cm-wafer) patterned with

negative photoresist SU-8 (Gersteltec, Switzerland) following a design customized to the experimental application.

The wafer was first cleaned with an oxygen plasma etcher (GigaBatch, PVA TePla, Germany) (Figure 2.2a). For the chip designs that required the fabrication of a SU-8 layer thicker than 40 μm (such as the one described in Chapters 4 and 5), the wafer was first coated with an SU-8 adhesion layer to improve the following adhesion of the thicker SU-8 layer on the substrate. Otherwise, the layer of the desired thickness was directly patterned on silicon. To pattern the adhesion layer, SU-8 was spin-coated at 1176 rpm to achieve a 2-μm thickness (LSM200 coater, Sawatec, Switzerland) (Figure 2.2b); the photoresist was then soft-baked following the standard soft-baking curves, reaching a maximum temperature of 90 °C (LSM200, Sawatec, Switzerland) (Figure 2.2c), and exposed in mask-less mode to UV light (λ=365 nm, MJB4, Heidelberg Instruments, Germany) (Figure 2.2d).

Using the same machines, the SU-8 layer of the desired thickness was then patterned, either directly on silicon or on the adhesion layer. After spin-coating (Figure 2.2e), the SU-8 was soft-baked (Figure 2.2f) and exposed to light (Figure 2.2g) using the mask fabricated following the process flow described in Figure 2.1. Afterwards, post-exposure bake (LSM200, Sawatec, Switzerland) (Figure 2.2h) and development of the non-exposed SU-8 in propylene glycol methyl ether acetate (PGMEA) and isopropanol (IPA) (Figure 2.2i) were performed.

The process flow was optimized to prevent SU-8 delamination from the substrate (Figure 2.3a, red arrows), which was due to over-polymerization of the photoresist. To avoid this undesired effect, several exposure doses were tested, where the exposure time was progressively reduced by 10% (Figure 2.3b), 20% (Figure 2.3c) and 30% (Figure 2.3d), starting from the exposure time recommended by the resist producer. The decrease of the exposure time determined an increase in the number of cracks in the SU-8 (Figure 2.3c-d, red arrows). However, as the presence of these small defects did not affect the further fabrication steps, we opted for a decrease of the exposure time by 30%.

The last photolithographic step was the hard-bake of the SU-8 pattern (Figure 2.2j) and was only performed to fabricate those chips that required an additional 90 μm SU-8 layer on top of the first one, such as the ones described in Chapters 3 and 6. This step consisted in a 6 h-long baking step during which the temperature was first increased from 30 °C to 130 °C at a rate of 1 °C/min, then kept at 130 °C for 2 h and finally brought down to 30 °C at the same rate. Thanks to the hard-bake, in fact, the thermal, chemical and physical stability of the first 40 μm SU-8 layer was significantly improved, in order to prevent it from damaging during the patterning of the second 90 μm SU-8 layer. Moreover, the hard-bake step completed the polymerization of the photoresist, removing therefore the cracks on the first SU-8 layer. The beneficial effect of hard-bake can be appreciated in Figure 2.4. Compared to the mask design (Figure 2.4a), the pattern fabricated without applying the hard-bake step clearly showed abnormal features and
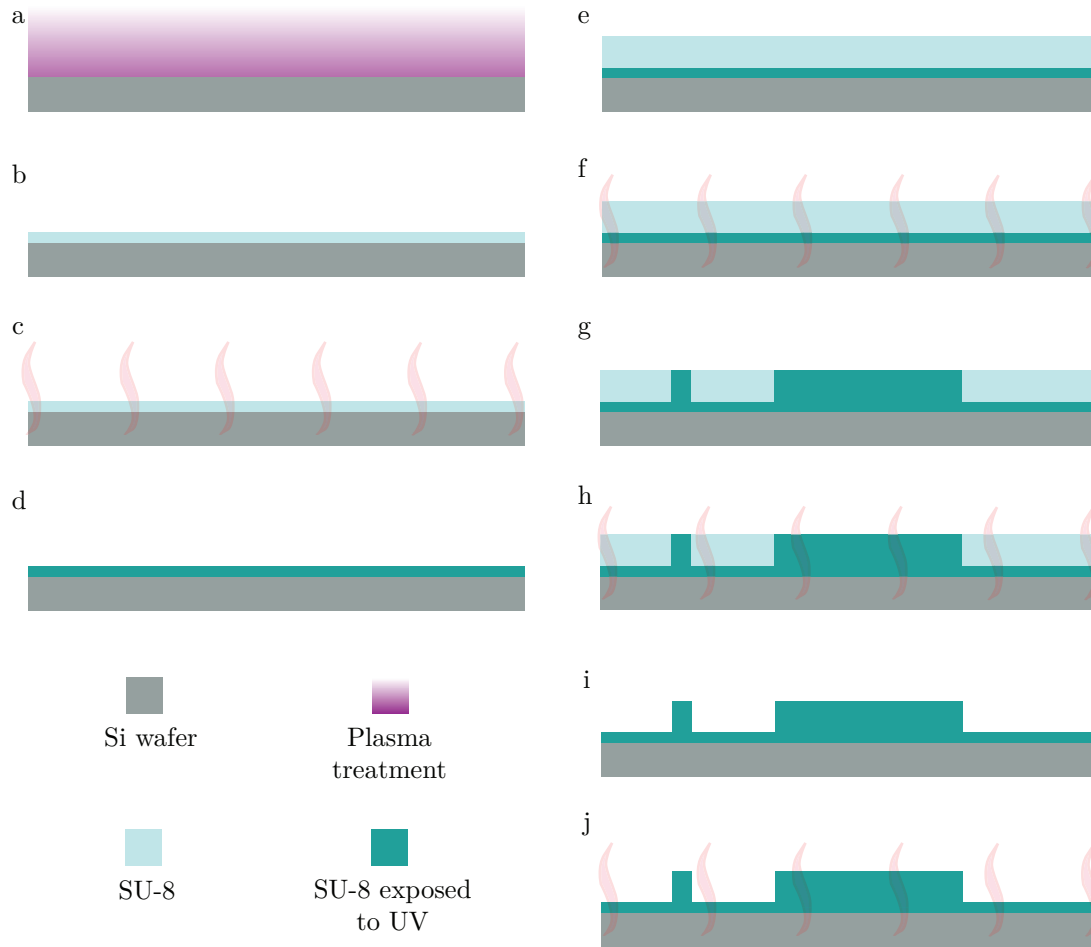
Figure 2.2 – Schematic of a SU-8 patterning process-flow. a) Oxygen plasma cleaning of the silicon wafer substrate. b) Spin-coating of the 2 μm SU-8 adhesion layer. c) Soft-bake of the 2 μm SU-8 adhesion layer. d) Mask-less exposure of the 2 μm SU-8 adhesion layer. e) Spin-coating of additional SU-8 layers of either 40, 60, 80 or 90 μm-thickness. f) Soft-bake of SU-8 photoresist. g) Exposure of the photoresist using a previously fabricated photomask. h) Post-exposure bake of the SU-8 photoresist. i) Development of the non-exposed SU-8 photoresist. j) Hard-bake performed only on the thick SU-8 layer, before patterning of an eventual additional SU-8 photoresist.
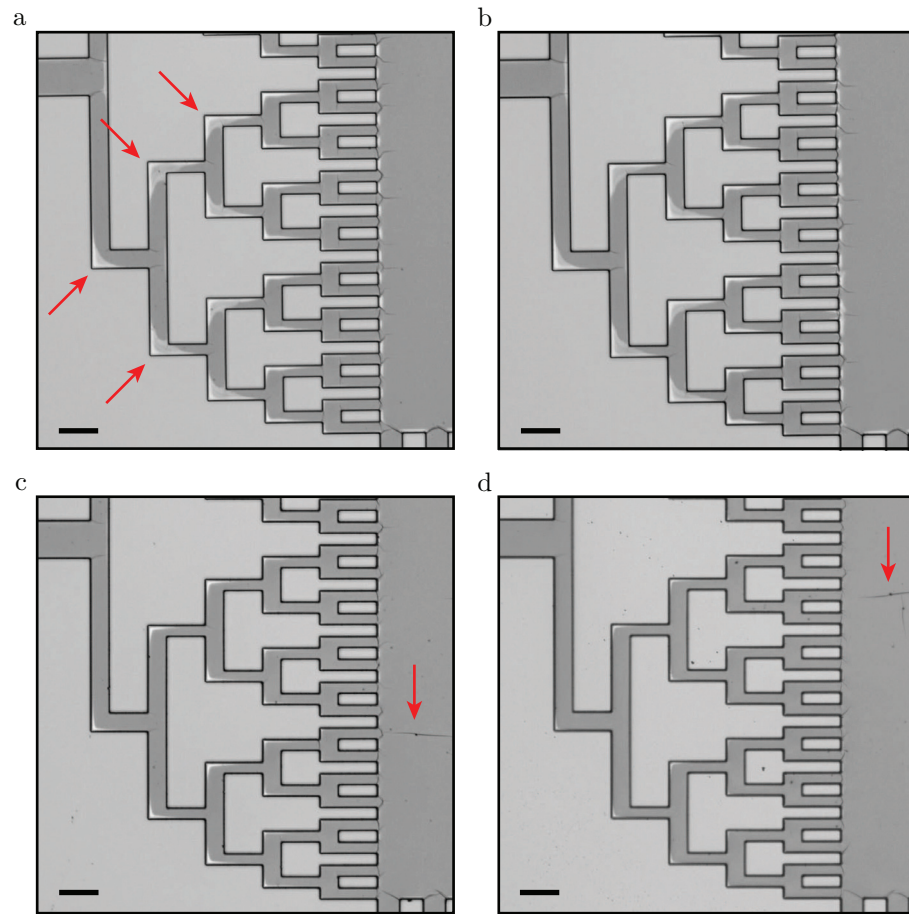
Figure 2.3 – Detail of representative 40 μm SU-8 micro-channels patterned upon different exposure doses. a) Pattern obtained using the exposure dose recommended by the resist producer, in this case 166 mJ/cm^2. SU-8 delaminated in some spots (lighter corners pointed by the red arrows) typically due to over-exposure. b) Pattern obtained by reducing the exposure dose by 10%, still showing severe delamination. c) Pattern obtained by reducing the exposure dose by 20%, showing improved adhesion of SU-8 to the substrate. Cracks (red arrow), however, appear due to insufficient polymerization. d) Pattern obtained by reducing the exposure dose by 30%, showing significantly improved adhesion and some cracks (red arrow). Scale bar = 100 μm.

a

b

c

40 μm SU-8,
1st layer

90 μm SU-8,
2nd layer
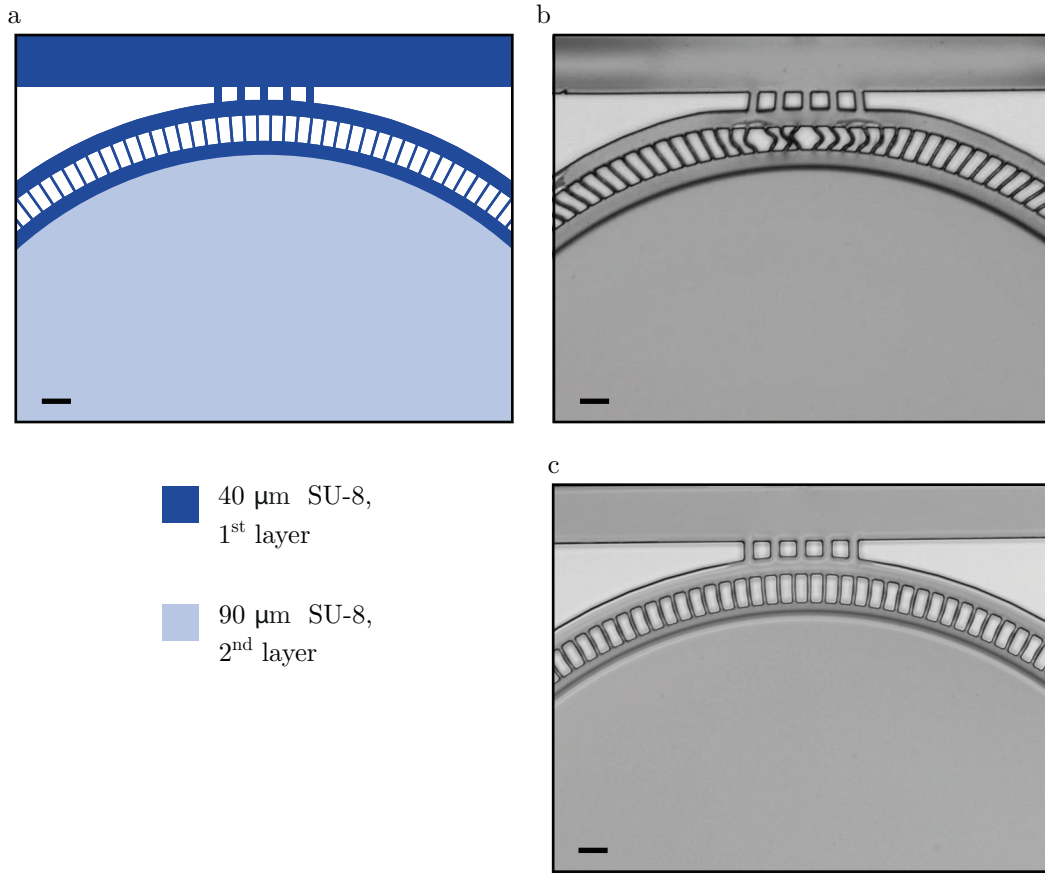
Figure 2.4 – Chemical and thermal stress on a representative portion of a SU-8 mold. a) Design of the chip, where the 40 μm-thick SU-8 is colored in dark blue and the second 90 μm-thick layer on top of the first is colored in light blue. b) Pattern with abnormal configuration and poor adhesion, as channels are no longer straight and are laying on different focal planes, indicating detachment. This undesired result was due to chemical and thermal stresses on the first 40 μm-thick layer upon fabrication of the superior 90 μm-thick layer. c) Pattern obtained by performing a hard-bake. The design accurately replicates the mask design in panel a). Scale bar = 50 μm.

poor adhesion, due to chemical and thermal stresses occurring during the fabrication of the top layer (Figure 2.4b). On the other hand, when a hard-bake was performed, the resulting pattern accurately replicated the mask design (Figure 2.4c). After hard-bake, the second 90 μm SU-8 layer was patterned using the same steps described in Figure 2.2e-i for the fabrication of the first layer.

2.3 Fabrication and assembling of the microfluidic chip

The microfluidic devices are prepared by soft lithography [39], using PDMS (Sylgard 184 Dow Corning) and glass. A SU-8/silicon mold (see Figure 2.5a) was placed in a container. The PDMS base was thoroughly mixed with the curing agent at a 10:1 weight ratio,
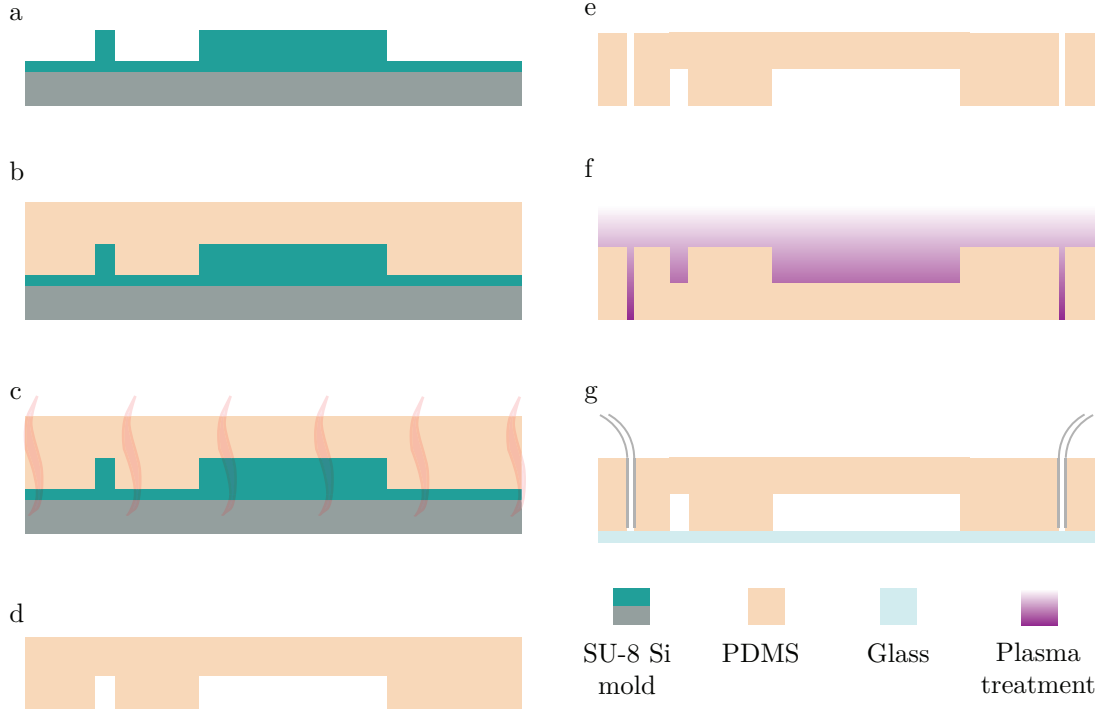
Figure 2.5 – Schematic of fabrication of a PDMS-glass chip by replica molding. a) SU-8 and silicon mold obtained by photolithography as described in Figure 2.2. b) The mixture of PDMS base and curing agent is poured on the mold, until the desired thickness is achieved. c) The PDMS mixture is cured at 80 °C for 1 h in an oven. d) Each PDMS chip is diced and removed from the mold, and e) holes are punched to create fluidic connections. f) The clean surfaces of PDMS and glass slide are activated by air plasma before the bonding step. g) Tubes are inserted into the PDMS holes.

starting in this way the curing process. The mixture was poured on the mold into the container, until the desired PDMS thickness was achieved (Figure 2.5b). If air bubbles were entrapped, the whole container was kept under vacuum until evacuation of all the bubbles. In order to accelerate the curing process, the container was cured at 80 °C for 1 h (Figure 2.5c). Afterwards, the solidified PDMS was removed from the mold (Figure 2.5d), each PDMS chip was diced and fluidic inlets and outlets were made by punching holes into it (Figure 2.5e). The PDMS chip was then bonded with a 26 mm × 76 mm glass slide upon air-plasma activation of both surfaces (Figure 2.5f). Finally, tygon tubes with 0.51 mm inner and 1.52 mm outer diameters (Fisher Scientific, Switzerland) were plugged in the PDMS holes (Figure 2.5g).

2.4 Experimental setup

The microfluidic chip (Figure 2.6a) was integrated onto an inverted microscope (Figure 2.6b) (Axio Observer, Zeiss, Germany) equipped with two illumination systems: (i) a

precisExcite High-Power LED Illumination system (Visitron, Puchheim, Germany) for brightfield imaging and (ii) a Lambda DG4 illumination system (Sutter instruments, Novato, CA, US) for fluorescence imaging. A black and white camera (ORCA-ER, Hamamatsu, Japan) (Figure 2.6c) was connected to the microscope optical path and controlled by VisiView Premier Image acquisition software (Visitron, Puchheim, Germany). The microscope was equipped with a motorized xyz-stage (Figure 2.6d) that had an ASI piezo controller for z-displacement (Visitron, Puchheim, Germany). The automated imaging process was controlled using VisiView. The microfluidic operations were controlled using Nemesys syringe pumps (Figure 2.6e) and relative control software (Cetoni, Korbussen, Germany). Given the relatively long time scale of each experiment, the syringe dedicated to *E. coli* delivery was provided with a stirring system in order to prevent bacteria from sedimenting at the bottom of the syringe. I placed a magnetic rod (1 mm × 1 mm × 2 mm) (Supermagnete, Uster, Switzerland) inside the syringe (Figure 2.6f). A rigid tube with small magnet rods blocked inside and fixed to the axis of a DC motor 6/9 V (Arduino, Ivrea, Italy) was positioned adjacent to the syringe (Figure 2.6g). The rotation of the motor axis and its rods induced agitation in the magnet inside the syringe. The rotation of the motor axis was controlled by a microcontroller (Arduino, Ivrea, Italy) and it was synchronized to the syringe control, so that *E. coli* was stirred before being injected in the microfluidic system.
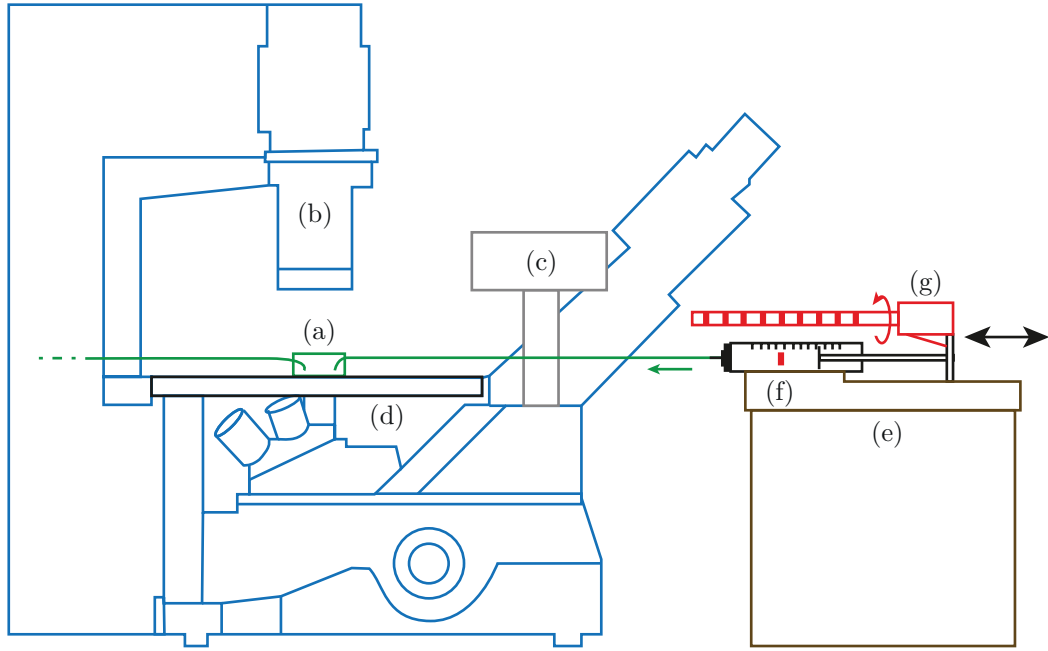
Figure 2.6 – Microfluidic setup. a) Microfluidic device with tubings plugged inside. b) Inverted optical microscope, (Axio Observer, Zeiss, Germany). c) Black and white camera, Hamamatsu, Japan. d) Motorized xyz-stage with an ASI piezo controller for z-displacement (Visitron, Puchheim, Germany). e) Syringe pumps (Nemesys, Cetoni, Germany). f) Magnetic rod (1 mm × 1 mm × 2 mm) (Supermagnete, Uster, Switzerland) placed inside the syringe. g) Rigid tube with small magnet rods blocked inside, fixed to the axis of a DC motor 6/9 V (Arduino, Ivrea, Italy) and positioned adjacent to the syringe.

3 Individualized multi-phenotypic response to drug and genetic cues of a *C. elegans* population

Abstract Complex molecular and cellular interactions in multicellular organisms can lead to heterogeneous phenotypic responses to treatments. This makes individual responses more informative than population-averaged read-outs for fine analysis. Intra-population variability should be appreciated when testing new compounds to identify phenotypic predictors of the therapeutic outcome. In this Chapter, I present a new strategy to monitor different phenotypic traits of individual *C. elegans* nematodes throughout their life-cycle. Single worms were isolated and cultured from egg to adulthood in a microfluidic device, in which phenotypic changes during development could be quantified. Specifically, the method was validated by analyzing the response of *C. elegans* to pharmacological and genetic treatments used to alter the mitochondrial unfolded protein response (UPR^{mt}). Importantly, the extensive single-worm phenotyping information revealed, in many cases, specific sub-populations that would otherwise be undetectable. From this phenome data, single worms could be classified as responders or non-responders to a treatment. Evaluating the heterogeneity in response and its markers with this method, it would be possible to elucidate pharmaceutical or therapeutic deviations that are still being overlooked.

This chapter is an adapted version of the following publications:

- **M. C. Letizia**, M. Cornaglia, R. Trouillon, V. Sorrentino, L. Mouchiroud, M. S. B. Sleiman, J. Auwerx and M. A. M. Gijs, "Microfluidics-enabled phenotyping of a whole population of *C. elegans* worms over their embryonic and post-embryonic development at single-organism resolution", *Microsystems and Nanoengineering*, manuscript accepted.
- **M. C. Letizia**, M. Cornaglia, V. Sorrentino, J. Auwerx and M. A. M. Gijs, "A microfluidic platform for an automated monitoring of *C. elegans* embryo-to-adulthood development at single organism resolution". Proc. of 20th International

Conference on Miniaturized Systems for Chemistry and Life Sciences (microTAS 2016), Dublin, Ireland, October 2016.
Oral presentation

- **M. C. Letizia**, M. Cornaglia, R. Trouillon, M. A. M. Gijs, "Microfluidic high-content screening in a *C. elegans* model at single animal-resolution". Proc. of 39th International Conference of the IEEE Engineering in Medicine and Biology Society (EMBC2017), Jeju Island, Korea, July 2017.
Oral presentation and **poster** presentation

3.1 Introduction

Heterogeneity in response to drugs or treatments can impede the quality of care, thus spurring the development of individualized therapeutic strategies [40], [41]. The growing interest in personalized medicine is moving pharmacological research towards the preliminary identification of sub-groups of patients who will benefit from a certain treatment, and separating them from those for whom the treatment will not be effective or even deleterious. Such *a priori* knowledge would allow tailoring the treatment to the characteristics of each individual, rather than to a population-averaged behavior. To capture the individual variability, longitudinal experiments are needed, where large datasets are collected while maintaining the possibility to observe the response of a single entity. Big data approaches can be applied to identify different sub-groups, correlate them with markers and phenotypes and therefore provide new patterns predicting the response to the drug or treatment.

Given the cost and high attrition rate of human clinical trials, animal models are still widely used in early stages of drug development to elucidate the therapeutic mechanisms and to extrapolate the drug response to humans. The nematode *C. elegans* is a popular animal model for the analysis of complex traits, such as metabolism and aging, at the molecular, cellular, organ and organismal levels [42]. However, the vast majority of the current biological knowledge, for any model, is largely based on population measurements, hiding potentially relevant individual behaviors. In the case of *C. elegans*, the majority of the experimental repertoire is based on analyzing and phenotyping large groups of individuals, hindering the crucial individualized spatiotemporal mapping. The importance of a phenotypic analysis at single-individual resolution becomes even more crucial when performing RNAi phenotypic screenings, where significant population variability is expected, and overall phenotypes cannot fully capture the complexity of the response. Microfluidics has been instrumental in enabling single-worm analysis with robust, high-throughput and reproducible screenings [19], [20], [26], [43]. However, it was not exploited for systematic longitudinal phenotypic profiling of whole organisms. A platform allowing single-worm based multi-phenotypic measures upon a specific treatment would pave the way for high-content, individualized analysis and possibly targeted follow-up treatments. In this context, this Chapter describes an innovative chip-based strategy for the precise analysis of the heterogeneous response to pharmacological or genetic treatments – and the resulting identification of heterogeneous biomarkers or phenotypes – amongst a controlled *C. elegans* population. In this endeavor, as illustrated in Figure 3.1, a microfluidic platform was designed to isolate naturally-synchronized embryos upon egg laying into single-worm chambers, where their identity was preserved during their life-cycle. Several phenotypes were monitored for each animal, resulting in high-content phenome data for each experimental condition. Once all the individual phenotypes are extracted, one can match the different experimental conditions with phenotypic signatures. Multivariate methods were employed to navigate the datasets and identify only the most important phenotypes for each experimental condition. Phenotypic clusters corresponding to dif-
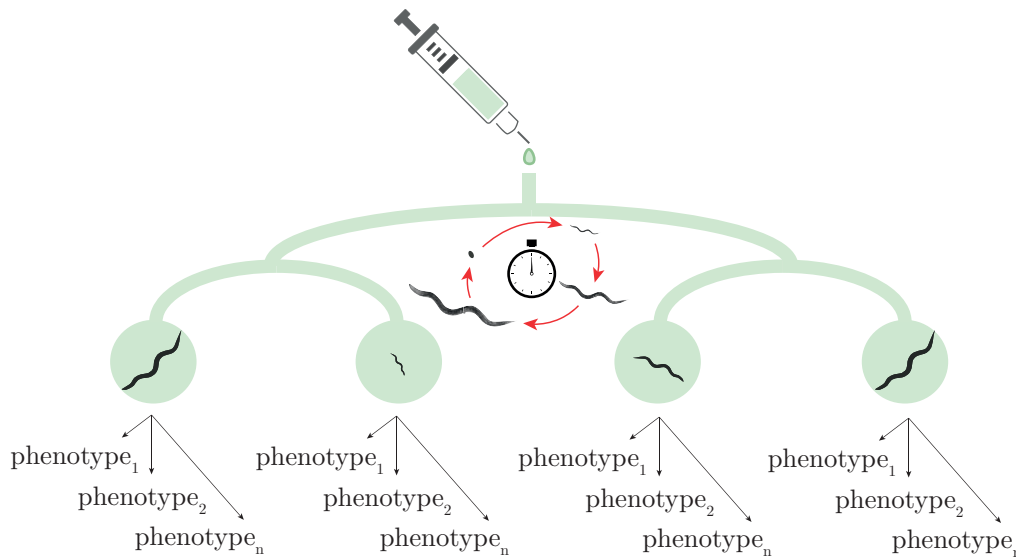
Figure 3.1 – Illustration of the single-worm based approach to extract different phenotypes upon testing of a pharmacological of genetic compound over the full life-cycle.

ferent sub-populations of single worms were identified, highlighting intra-population heterogeneity. Moreover, I validated the method by analyzing the response of *C. elegans* to pharmacological and genetic tools used to activate the mitochondrial unfolded protein response (UPR^{mt}), a stress-response that is conserved across species [44]–[46]. The single-worm based analysis method was employed to identify different treatment-dependent markers for mitochondrial stress. Interestingly, while mild intra-population variations were observed after drug treatments, several worm sub-populations with markedly different stress biomarkers appeared after RNAi feeding.

3.2 An automated platform for isolation and monitoring of single *C. elegans* organisms during embryonic and post-embryonic development

A microfluidic chip for the phenotypical analysis and biomarker identification at single-worm level throughout its life-cycle was designed and fabricated in PDMS and glass (Figure 3.2a), following the fabrication steps described in Chapter 2. To perform the experiments, the setup described in Section 2.4 was used. First, a non-synchronized population of *C. elegans* was loaded in the parent culture chamber (Figure 3.2b,c). Dedicated filters were fitted to outlet Out1 to retain only young adult (YA) worms in the chamber and wash younger worms out. Afterwards, those YA worms were fed with *E. coli* bacteria until egg production. Once laid, embryos were transported by the flow to the progeny culture chamber matrix (Figure 3.2b,d), consisting of an array of 16 single-worm chambers, each fitted with a trap for single-embryo capture (Figure

3.2. An automated platform for isolation and monitoring of single *C. elegans* organisms during embryonic and post-embryonic development
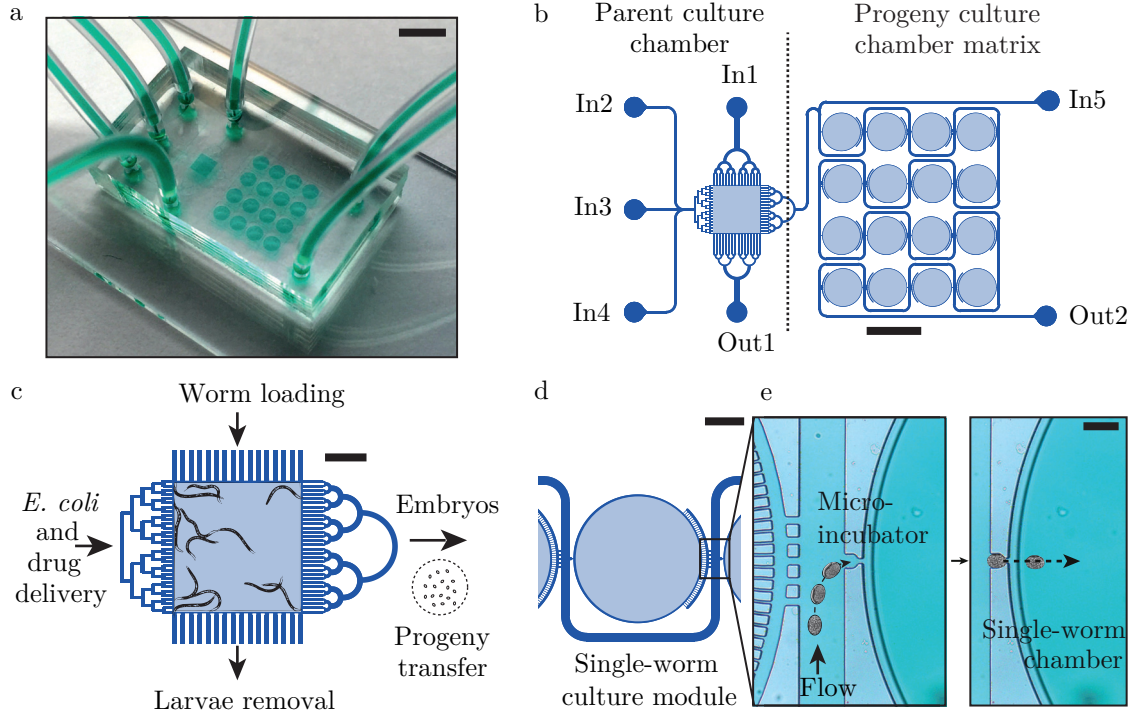
Figure 3.2 – Automated platform for isolation and monitoring of single *C. elegans* organisms during full life-cycle. a) Picture of the microfluidic device. Scale bar = 5 mm. b) Schematic of the microfluidic device, showing the parent culture chamber and the progeny culture chamber matrix. Scale bar = 2 mm. c) Zoom on the parent culture chamber including typical drawings of young adult (YA) *C. elegans*. Scale bar = 500 μm. d) Schematic representation of a module of the progeny culture chamber matrix. Scale bar = 200 μm. e) Sketch of the egg hydrodynamic trapping in a single-embryo micro-incubator and its transfer in the adjacent single-worm chamber. Scale bar = 100 μm.
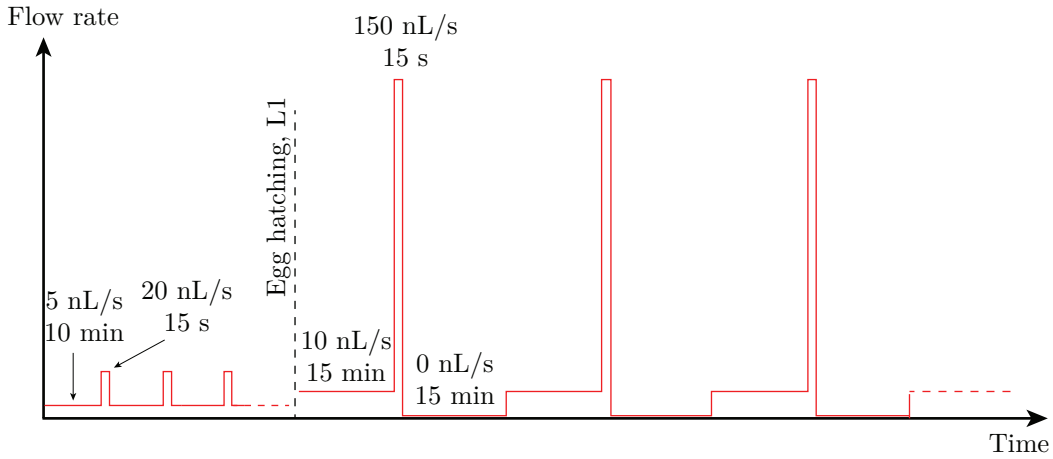
Figure 3.3 – Bacterial flow profile used to perfuse the single worm chamber array over the full experiment. Different flow profiles, adapted to the worm's stage of development, were chosen for embryonic and larval development.

3.2e). Through hydrodynamic trapping the embryos occupied consecutive traps, forming a naturally-synchronized population. Using this approach, the traditional aggressive bleaching step for embryo isolation and the time-consuming manual synchronization procedures were avoided [13].

The single-embryo traps were presented and discussed in a previous study published by our group [47]. The device used in the current work pushes further this concept by connecting a worm-culture chamber to each single-embryo trap (Figure 3.2d,e). With this approach, the new-born larva remains isolated and can be cultured until adulthood onset, allowing for the first time the on-chip monitoring of embryonic and post-embryonic development. In fact, after capture, each embryo was simultaneously injected from the micro-incubator to the adjacent single-worm chamber by high flow rate, exploiting PDMS elasticity (Figure 3.2e). Each chamber is also provided with filters (5 μm-spacing) to allow medium flow while preventing L1 worms from escaping.

A flow profile adapted to larval age was developed, in order to provide enough nutrients to the progeny generation (Figure 3.3). During the embryonic twitching-hatching stage and L1 stage, a repetitive loop flow profile of 5 nL/s for 10 min and 20 nL/s for 15 s was delivered, in order to prevent the newborn larvae from escaping through the single-embryo micro-incubator, as the incubator aperture dimension matched the L1 size. Afterwards, a loop flow profile of 10 nL/s for 15 min, 150 nL/s for 15 s and 0 nL/s for 15 min was used, in order to refresh *E. coli* bacteria in the chambers, to avoid stressing the worms with continuous hydrodynamic forces.

The acquisition system (see Section 2.4) was programmed so that brightfield (exposure time = 2 ms) and fluorescent (exposure time = 150 ms) pictures were recorded every 7 min on each position. A Zeiss 20$\times$ NA 0.22 objective was used for imaging of single-embryos in the micro-incubator, while a Zeiss 4$\times$ NA 0.075 objective was used for imaging of each single-worm chamber. A single picture was taken to capture each worm at a time-point, as

the field of view of the objective was large enough to accommodate the whole single-worm chamber. An immobilization method was not needed, as the mobility of the worms was low. Indeed, the presence of optimized amounts of food along the duration of the whole experiment limited food-seeking behavior and motion. To capture sharp fluorescent pictures, the exposure time was finely tuned to avoid extensive animal movement within the exposure time window. The fluorescent picture was captured 150 ms (fluorescent exposure time) after the brightfield picture. Afterwards, the motorized stage moved to the following single-worm chamber and waited 3 seconds for stabilization, before brightfield and fluorescent pictures were shot. In this way, the full array could be imaged in about 50 s. Considering the typical timescale of the evolution of the development of the worms (∼10 h for embryonal development and 2-5 days for larval development), this imaging routine was not expected to introduce a development mismatch between the different worms.

3.3 Optimization of the hydrodynamic trapping

The single-worm culture module (Figure 3.2d) was considered as a system described by fluidic resistances. The resistance given by the serpentine channel $R_{channel}$ is in parallel with R_{eq}, which is the resistance given by the embryo micro-incubator, the single-worm chamber and the filters, in series (see Figure 3.4a). The embryo delivered towards the progeny culture chamber matrix is guided by the flow towards the single-embryo micro-incubator, because $R_{channel} > R_{eq}$. Once one single-embryo micro-incubator is occupied, R_{eq} increases becoming higher than $R_{channel}$ and the coming embryos occupy the next available trap. In this way, hydrodynamic trapping ensures that all the micro-incubators are consecutively occupied in an automated way.

In very first approximation, the resistances were estimated by considering the pressure drop between inlet and outlet of each single-worm culture module along the two parallel fluidic paths and imposing equal pressure difference along them, assuming Poiseuille flow conditions [48] and using Poiseuille Equation 1.3. However, losses due to the design geometry - such as channel bends or changing in the cross section - were neglected in this way. Therefore, the design of the microfluidic device was later optimized through the results of a systematic experimental characterization. The trapping efficiency was estimated for 6 similar versions of our device, featuring varying bends or lengths of the serpentine channel, varying number and shape of the filters, and therefore varying $R_{channel}/R_{eq}$. Four examples are given in Figure 3.4a, b, c and d. For these tests, 30 μm polystyrene beads were employed as trapping objects to mimic *C. elegans* embryos, and the capture efficiency was defined as the percentage of traps containing a single bead over the total number of available trapping sites, for a constant amount of beads injected into the microfluidic device. From our experimental analysis, we could conclude that a ratio $R_{channel}/R_{eq}$ of 2.6 maximizes the system trapping efficiency (83%) (Figure 3.4e). This configuration also ensured that each chamber was occupied by only one bead at a
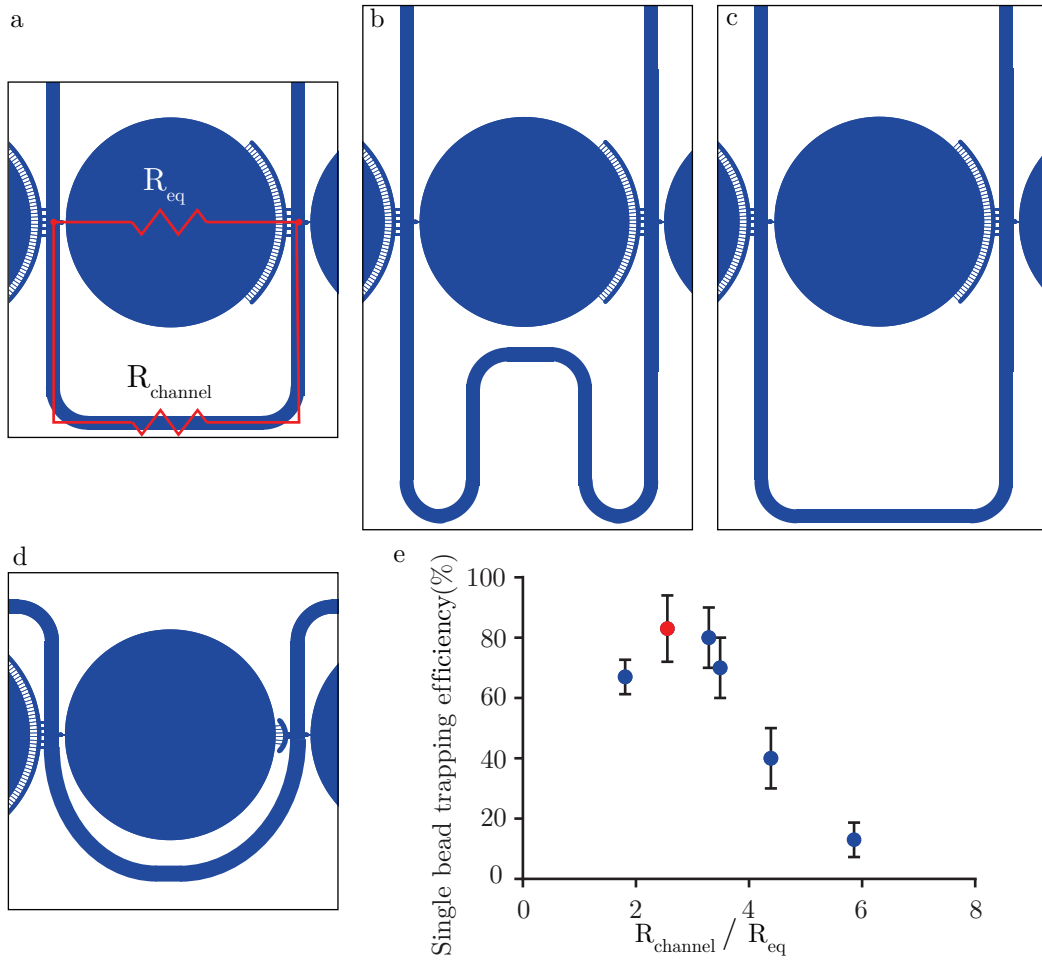
Figure 3.4 – Experimental design optimization to improve the efficiency of the hydrodynamic trapping. a-d) Four (out of 6) exemplifying chip designs featuring different $R_{channel}/R_{eq}$ ratio, fabricated and tested to calculate the trapping efficiency. e) Results of the experimental characterization of the trapping efficiency. The highest efficiency (83%) was obtained for a $R_{channel}/R_{eq}$ of $\sim$2.6 (red dot). Data is shown as average $\pm$ standard deviation (SD).

time, and was therefore chosen to perform the experiments.

3.4   High-content phenotypic analysis at single-organism resolution

Starting from embryo collection in the progeny culture chamber matrix, I identified the milestones commonly used to characterize embryonic and larval development [49], [50], detailed in Figure 3.5a. *C. elegans* embryos, laid upon beginning of gastrulation, were immediately trapped in the embryo-incubator array. Bean stage and twitching onset were observed in the single-embryo incubator, while egg hatching was detected in the single-worm chamber. The duration of each larval stage could be unambiguously

a

| Gastrula | Bean stage | Twitching onset | L1 - L2 | L2 - L3 | L3 - L4 | L4 - YA | A |

b

| Embryo viability | Length | Diameter | Gene expression | Sex fate | Fertility |

Figure 3.5 – Identified phenotypes for single-worm based analysis. a) Illustration of the parallel time-lapse imaging, here shown only for three representative worms, enabled on the worm array within the progeny culture chamber matrix during the full life-cycle. Arrows point at the molts seen as detached from the worm body. Scale bar = 50 μm. b) Illustration of the quantified phenotypic markers, namely embryo viability or hatching rate, worm length and diameter at the vulva at the stages L1, larval 2 (L2), larval 3 (L3), L4 and YA, the fluorescence expression of the gene of interest at the stages L1, L2, L3, L4 and YA, the sex fate and the percentage of fertile adult worms.

evaluated by measuring the time interval between consecutive moltings, which identify the actual biological transitions amongst the different larval stages (L1 to larval 4 (L4)), up to the YA stage. Adulthood onset was defined by the vulva protrusion, which normally coincides with the appearance of first self-fertilized embryos inside the worms, and which determined the end of the life-cycle and therefore of the experiment. Beside the development times, other important phenotypes were extracted for each animal (Figure 3.5b). First, the hatching rate was calculated to evaluate the embryo viability. Then, the average body length and diameter at the vulva, as well as the expression of a gene of interest via fluorescent read-out, were extracted for each larval stage of development. The sex fate (hermaphrodite or male) and the fertility rate were also recorded.

3.4.1   Phenotypic biomarker analysis of an UPR^{mt} reporter strain

UPR^{mt} is a stress response that maintains mitochondrial proteostasis via a system of chaperones and proteases controlling mitochondrial protein folding, assembly and degradation [44], [51], [52], as reviewed in [45]. It is a prototypical hormetic stress response, with deleterious or positive effects depending on the level of stress applied to the organism [53]. In *C. elegans*, UPR^{mt} activation is observed upon perturbation of the electron transport chain (ETC), as shown by downregulation of *cco-1*, a nuclear DNA-encoded component of ETC complex IV [44], or upon perturbation of mitochondrial proteostasis, as seen after loss-of-function of the protease *spg-7* [52]. Additionally, inhibition of mitochondrial translation, genetically via silencing of mitochondrial ribosomal genes such as *mrps-5* and pharmacologically by using the antibiotic doxycycline, induces both nematode and mammalian UPR^{mt} [51], [54]. UPR^{mt} induction during larval development in *C. elegans* leads to lifespan extension and reduced mitochondrial function [44], [51], as well as developmental delay and decreased brood size [44], [51], [55]. However, the relevance of these biomarkers to the lifespan extension, as well as accurate quantification and relative differences of these phenotypes due to various mitochondrial stressors are still being overlooked.

High-content phenotypic data on *hsp-6p::gfp* worms, a nematode UPR^{mt} reporter strain [56], was obtained by extracting biologically-informative phenotypic markers from the images. The durations of the developmental stages along the life-cycle – gastrula-bean stage (t(E1)), bean-twitching stage (t(E2)), twitching-hatching stage (t(E3)), duration of L1 stage (t(L1)), duration of L2 stage (t(L2)), duration of L3 stage (t(L3)), duration of L4 stage (t(L4)) and duration of YA stage (t(Y4)) – were systematically quantified for individual worms (16 per array, Figure 3.6a) and averaged over the array (Figure 3.6b). In the absence of treatment, the duration of these stages matched those reported for worms cultured on agar plates at the same temperature [57]. Moreover, 97% of the trapped embryos developed, while the rest did not hatch. 100% of the worms became fertile hermaphrodite adults, as internal eggs were observed (Figure 3.7a). The average worm lengths, corresponding to the skeleton (later abbreviated as length at L1 stage (L(L1)), length at L2 stage (L(L2)), length at L3 stage (L(L3)), length at L4 stage (L(L4)) and length at YA stage (L(YA))), and diameters measured at the vulva (later abbreviated as diameter at L1 stage (D(L1)), diameter at L2 stage (D(L2)), diameter at L3 stage (D(L3)), diameter at L4 stage (D(L4)) and diameter at YA stage (D(YA))), were also obtained (Figure 3.7b). The basal induction of the *hsp-6p::gfp* was quantified as a reporter of the UPR^{mt} activation by processing the fluorescent images to extract the signal-to-background ratio (SBR). The linear SBR increase over time (Figure 3.7c) suggests that the UPR^{mt} pathway is weakly activated in basal conditions [51], [56]. The fluorescent signal per worm area at each larval stage (fluorescent signal at L1 stage (F(L1)), fluorescent signal at L2 stage (F(L2)), fluorescent signal at L3 stage (F(L3)), fluorescent signal at L4 stage (F(L4)) and fluorescent signal at YA stage (F(YA))) was also computed (Figure 3.7d).
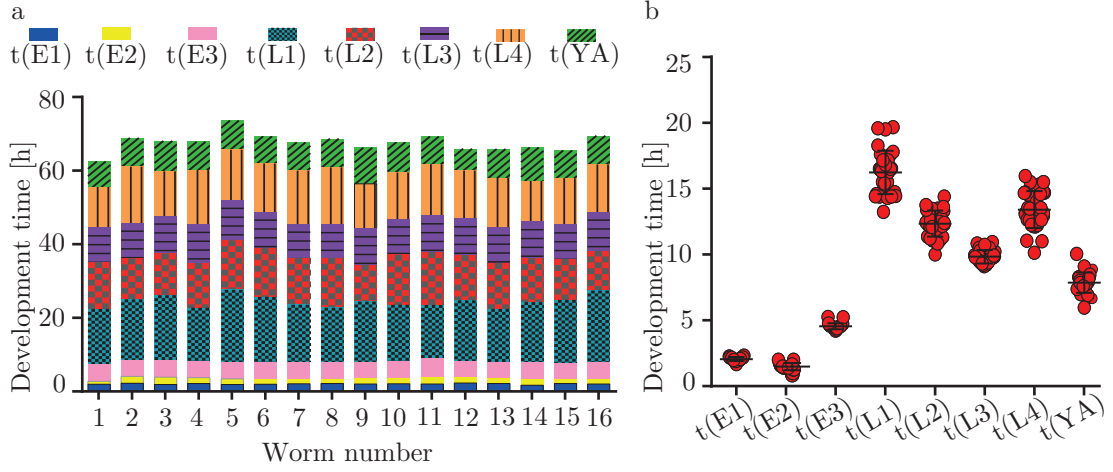
Figure 3.6 – Duration of the main embryonic and larval developmental phases for the *hsp-6p::gfp* worms at single-organism resolution. a) Duration of the main embryonic and larval developmental phases, observed for a matrix of 16 worms. b) Durations of embryonic and larval developmental stages. Each dot represents the duration of a precise developmental stage for one worm. Average ± SD values are superimposed. N=16.

3.5 Individualized response to pharmaceutical cues

3.5.1 Nicotinamide riboside homogeneously affects multiple facets of larval development

We tested the effect of nicotinamide riboside (NR), known for boosting the intra-cellular levels of the oxidized form of nicotinamide adenine dinucleotide (NAD+) [58]. NR promotes mitochondrial biogenesis by increasing cellular NAD+ levels and therefore sirtuin activity, thus elevating the mitochondrial proteins expression and the UPR^{mt} induction [59]. With our phenotyping platform, we investigated the effect of NR on the *C. elegans* life-cycle and mitochondrial stress response. A significant effect of NR on the life-cycle was observed, as revealed by hierarchical cluster analysis (HCA) (Figure 3.8a) and PCA (Figure 3.8b and Table 3.1) (more details about the performed statistical analysis in Section 3.7.4). In this case, PCA showed that all the investigated treated animals reacted to NR in a homogeneous fashion.

 NR slightly prolonged the embryonal bean-twitching phase t(E2) (Figure 3.9a) and embryo viability was not compromized, compared to the control group (Figure 3.9b). Moreover, NR severely extended the larval development time by 75% on average (Figure 3.9c), while reduced larval length and diameter were measured (Figure 3.9d,e). Moreover, the animals showed proper gonad development and 75% of the treated organisms were fertile (Figure 3.9f), as presence of internal eggs was observed (Figure 3.9g). Furthermore, data showed a slight decrease in *hsp-6p::gfp* expression in the NR-treated population with respect to the control (Figure 3.9h), indicating that UPR^{mt}, and so mitochondrial stress, was weakly activated by NR.
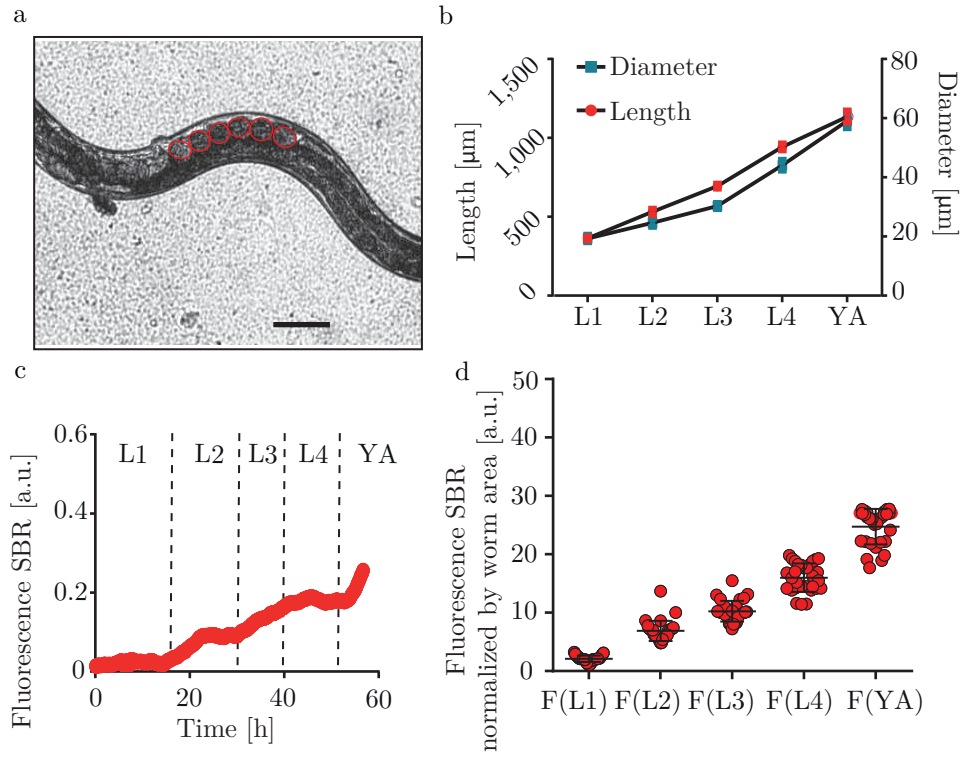
Figure 3.7 – Phenotypic analysis on a control strain at single-organism resolution. a) Brightfield picture of an adult worm. The red circles indicate internal embryos. Scale bar = 50 μm. b) Average length and diameter at each larval stage. Graph points are expressed as average $\pm$ SD. c) Quantification of *hsp-6p::gfp* expression as SBR for the full life-cycle. d) Quantification of *hsp-6p::gfp* expression as SBR normalized by worm size at each larval stage. N = 31.

Figure 3.8 – Phenotypic footprint of phenotypes of the control group and the NR-treated group. a) HCA of phenotypes of the control group and the NR-treated group. b) PCA of phenotypes of control and NR-treated groups. Single-worm data are arranged according to the first and the second PC of worms phenotypes.

Phenotype	PC 1 (73.3% of variance)		PC 2 (6.5% of variance)	
	Coordinates	Contributions	Coordinates	Contributions
t(E1)	-0.038	0.010	0.021	0.007
t(E2)	0.238	0.064	0.430	0.134
t(E3)	-0.012	0.003	0.059	0.018
t(L1)	0.252	0.068	0.107	0.033
t(L2)	0.098	0.026	0.137	0.043
t(L3)	0.294	0.079	0.222	0.069
t(L4)	0.342	0.092	0.116	0.036
t(YA)	**0.418**	**0.113**	0.252	0.078
L(L1)	-0.192	0.052	-0.139	0.043
L(L2)	-0.093	0.025	-0.129	0.040
L(L3)	-0.097	0.026	-0.078	0.024
L(L4)	-0.135	0.036	-0.101	0.032
L(YA)	-0.142	0.038	-0.069	0.022
F(L1)	-0.235	0.063	**0.434**	**0.135**
F(L2)	**-0.393**	**0.106**	**0.528**	**0.164**
F(L3)	-0.293	0.079	**0.360**	**0.112**
F(L4)	-0.266	0.072	0.003	0.001
F(YA)	-0.178	0.048	0.031	0.010

Table 3.1 – Coordinates and contributions of PCs 1 and 2 as result of PCA of phenotypes of control and NR-treated group. Phenotypes with significant contribution are marked in bold.
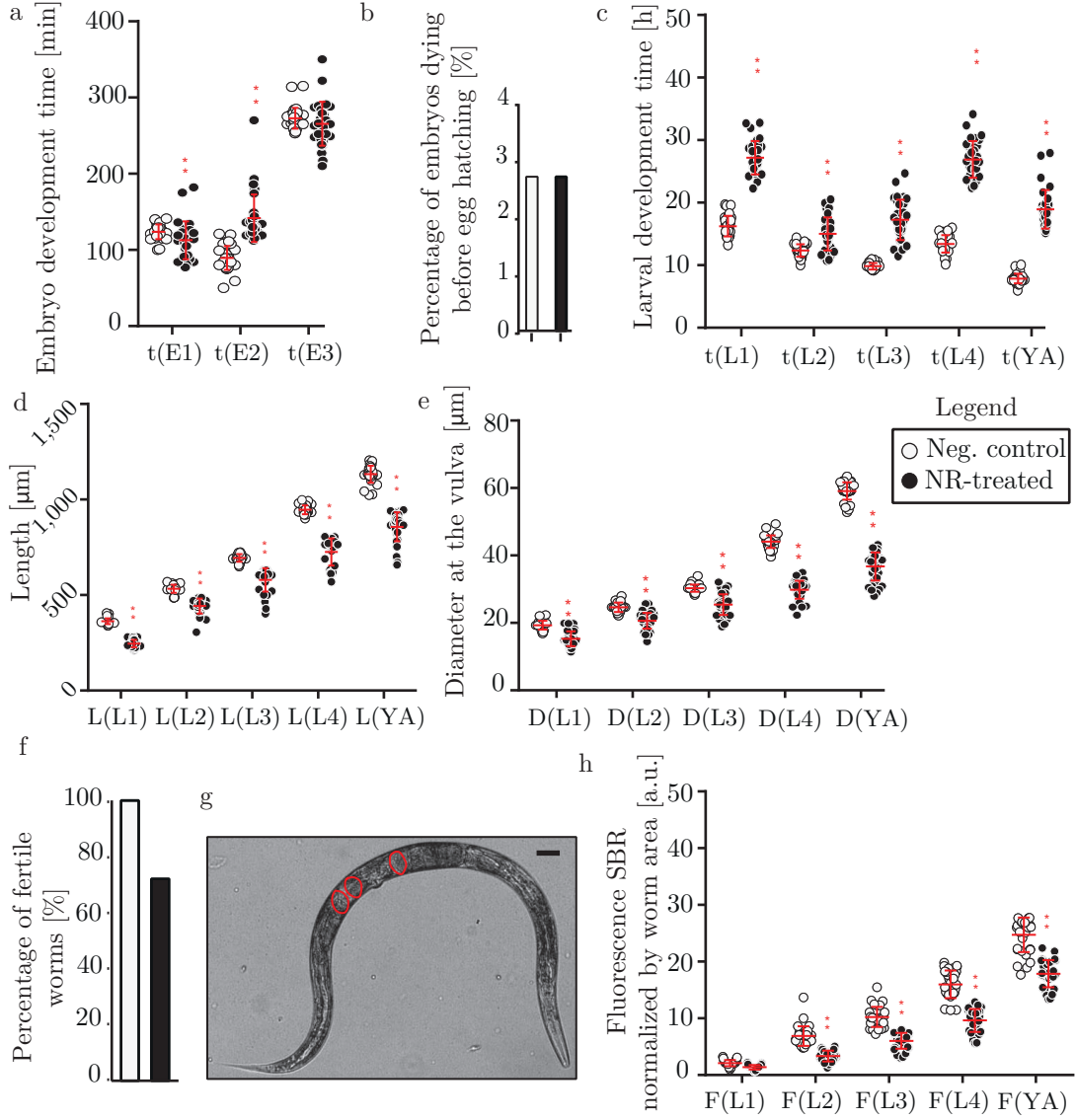
Figure 3.9 – Effect of NR on the *C. elegans* life-cycle. a-f, Comparison between control and treated worms of a) the durations of embryonic developmental stages, b) the percentage of embryos dying before egg hatching, c) the durations of larval developmental stages, d) the lengths and e) diameters at each larval stage, and f) the percentage of fertile adults. g) Brightfield picture of an adult treated worm. Red circles point at internal embryos. Scale bar = 50 μm. h) Comparison of SBR normalized by worm size at each larval stage between control and treated worms. N= 31 for control; N= 31 for the NR treatment. Untreated *hsp-6p::gfp* worms are used as controls (Dataset in Figures 3.6, 3.7).

Phenotype	PC 1 (78.8% of variance)		PC 2 (5.2% of variance)	
	Coordinates	Contributions	Coordinates	Contributions
t(E1)	-0.035	0.011	-0.140	0.049
t(E2)	0.292	0.092	-0.098	0.034
t(E3)	0.024	0.007	0.061	0.021
t(L1)	0.253	0.080	-0.050	0.018
t(L2)	0.191	0.060	0.066	0.023
t(L3)	**0.337**	**0.106**	-0.069	0.024
t(L4)	**0.326**	**0.103**	-0.075	0.026
t(YA)	**0.688**	**0.217**	-0.172	0.060
L(L1)	-0.049	0.015	-0.034	0.012
L(L2)	-0.085	0.027	-0.036	0.013
L(L3)	-0.089	0.028	-0.054	0.019
L(L4)	-0.117	0.037	-0.042	0.015
L(YA)	-0.133	0.042	0.027	0.010
F(L1)	0.034	0.011	**0.655**	**0.230**
F(L2)	0.125	0.039	**0.461**	**0.162**
F(L3)	0.103	0.032	**0.460**	**0.162**
F(L4)	0.157	0.050	0.177	0.062
F(YA)	0.135	0.042	0.169	0.059

Table 3.2 – Coordinates and contributions of PCs 1 and 2 as result of PCA of phenotypes of control and doxycycline-treated groups. Phenotypes with significant contribution are marked in bold.

3.5.2 Doxycycline prolongs larval development and induces sub-population-specific phenotypic changes

The platform was used to phenotypically characterize the effect of doxycycline, a pharmacological inducer of the UPR^{mt} [51]. HCA (Figure 3.10a) and PCA (Figure 3.10b and Table 3.2) were first run on the dense dataset to identify features of interest, and provide an overall phenotypic footprint of the effect of doxycycline on the treated worm population. This antibiotic induced severe deviations from control, as treated animals showed longer development time, confirming the doxycycline role in prolonging the animal development and extending its lifespan.

Interestingly, the unexpected permeability of the eggshell to doxycycline induced two different responses on the embryo population. The doxycycline treatment proved to be lethal for 9.4% of the embryos, that died before hatching (Figure 3.11a). This response is in line with the effect of other mitochondrial stressors [60], [61]. On the other hand, the embryo development of the surviving eggs was severely delayed (3.11b), especially during the bean-twitching phase t(E2). This effect was also observed in a previous study using a genetic mutation to induce mitochondrial stress [47]. As predicted by HCA and PCA, the impact of doxycycline was even more severe on the larval development time (3.11c) and size (3.11d and 3.11e), which featured a 1-fold or higher increase over the negative control,
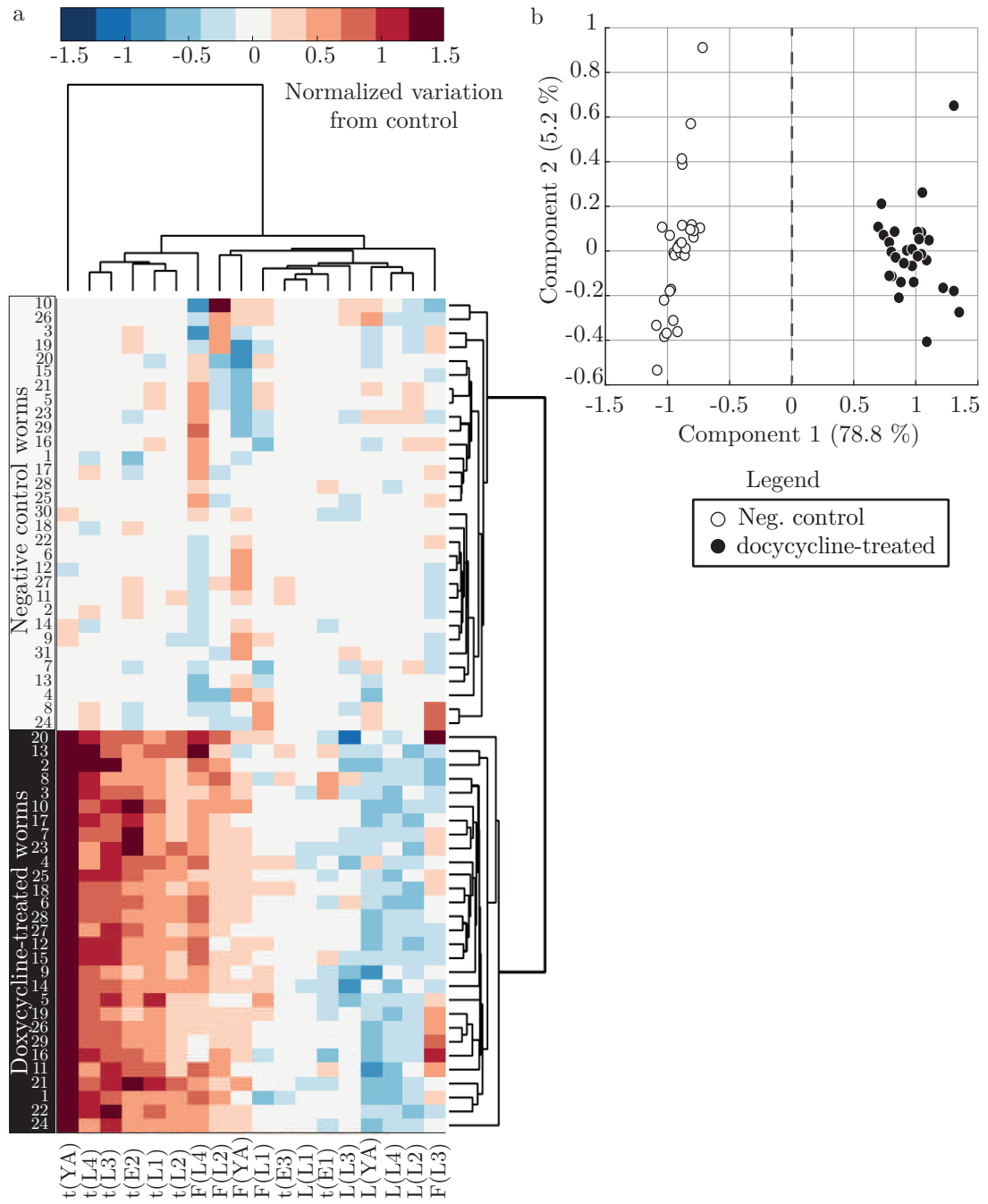
Figure 3.10 – Phenotypic footprint of phenotypes of the control group and the doxycycline-treated group. a) HCA of phenotypes of control and doxycycline-treated groups. b) PCA of phenotypes of control and doxycycline-treated groups. Single-worm data are arranged according to the first and the second PC of worms phenotypes.

especially for the L4 and the YA stages. This observation agrees with previous reports showing a similar delay in larval development when the electron transport chain function is compromised genetically [62]. Indeed, during the L3-L4 stages, mitochondria undergo a period of dramatic proliferation [63], making it the critical time-window, during which mitochondrial perturbations can have large impact on *C. elegans* larval development [62]. Moreover, doxycycline not only impaired gonad development and caused infertility (3.11f), but also pushed 8% of the individuals towards male development (3.12). These findings suggest that doxycycline exerts profound effects on developmental processes relying on mitochondrial support, favouring a shift towards male progeny formation, similar to what is observed with other sources of stress [64], but, interestingly, only in a subgroup of the population. Finally, the tracking of *hsp-6p::gfp* expression (3.11g), showed an overall increase starting at the L2 larval stage, which confirms the induction of mitochondrial stress by doxycycline, followed by the UPR^{mt}.

3.6   Individualized response to genetic cues

hsp-6p::gfp worms were treated with RNAi against either *mrps-5* [51] or *cco-1* [44], to investigate variations in the levels of gene silencing amongst the individuals. Briefly, RNAi technology takes advantage of the cell natural machinery, facilitated by short interfering RNA molecules, to effectively knock down expression of a gene of interest. This method can be used to identify and functionally assess genes that potentially participate in disease phenotypes. In addition, it provides an efficient mean for blocking expression of a specific gene and evaluating its response to chemical compounds or changes in signaling pathways [65].

3.6.1   RNAi treatment on *mrps-5* gene induces three sub-population-specific responses

Worms treated with *mrps-5* RNAi showed a heterogenous response during larval development, as revealed by HCA and PCA (Figure 3.13 and Table 3.3).

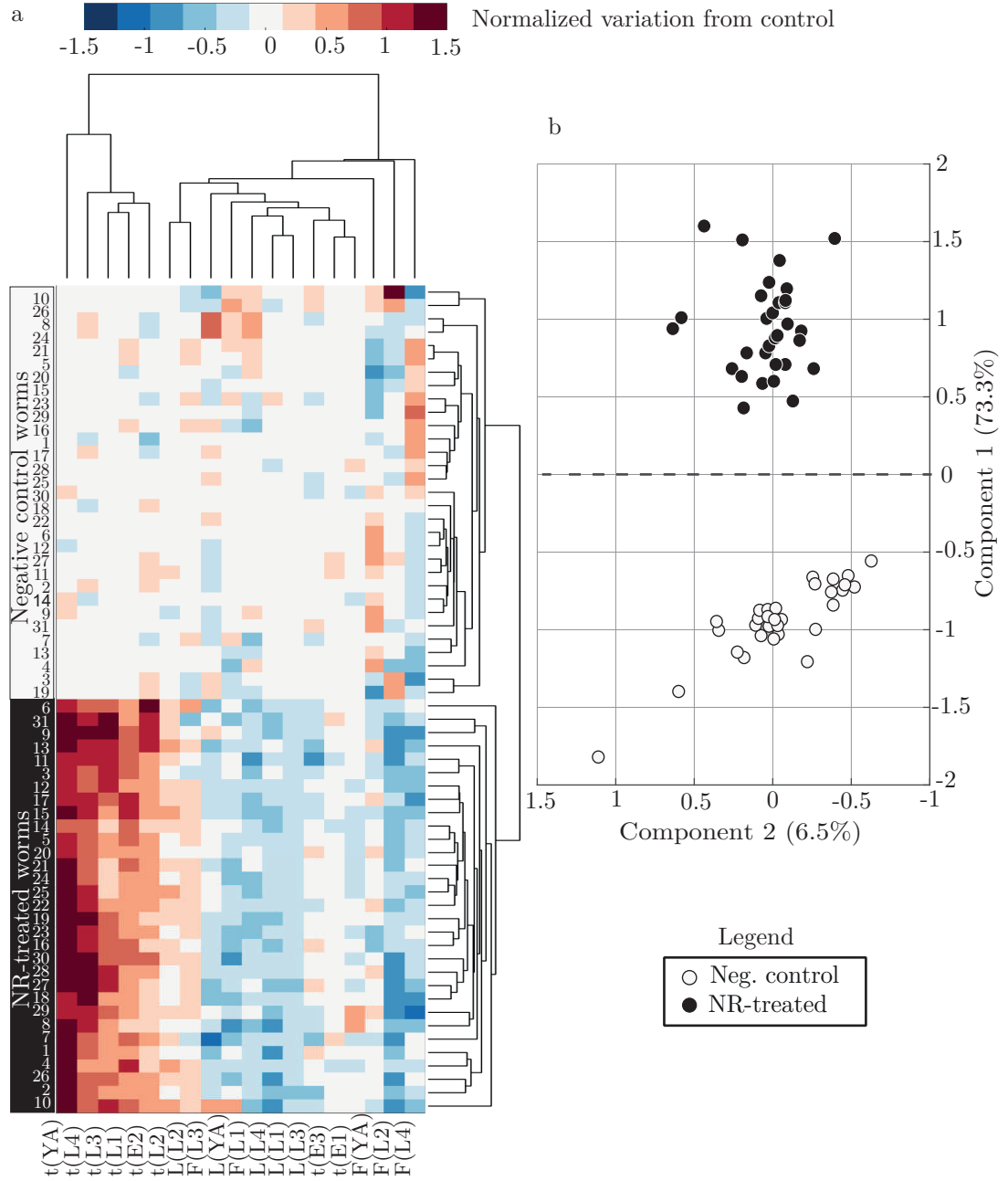 Interestingly, the embryo development was homogeneously delayed (Figure 3.14a). Moreover, 12.5% of the embryos died before hatching (Figure 3.14b). Overall, the phenotypic data of the surviving larvae indeed revealed longer development times (Figure 3.14c) and smaller body volumes (Figure 3.14d,e). However, a deeper observation of the phenotypes allowed separating the treated worms in 3 sub-populations, group 1, 2 and 3, accounting respectively for 46%, 15% and 39% of the treated animals. The treatment strongly prolonged the development times (Figure 3.14c), reduced the sizes (Figure 3.14d,e) and strongly activated UPR^{mt} (Figure 3.14f,g) of group 1. Group 2 showed a stronger developmental delay during L3 and L4 (Figure 3.14c) and a strong fluorescent activation at L4 (Figure 3.14f). Also group 3 showed a delayed development compared to control (Figure 3.14c). However, these animals did not complete the life-cycle, as
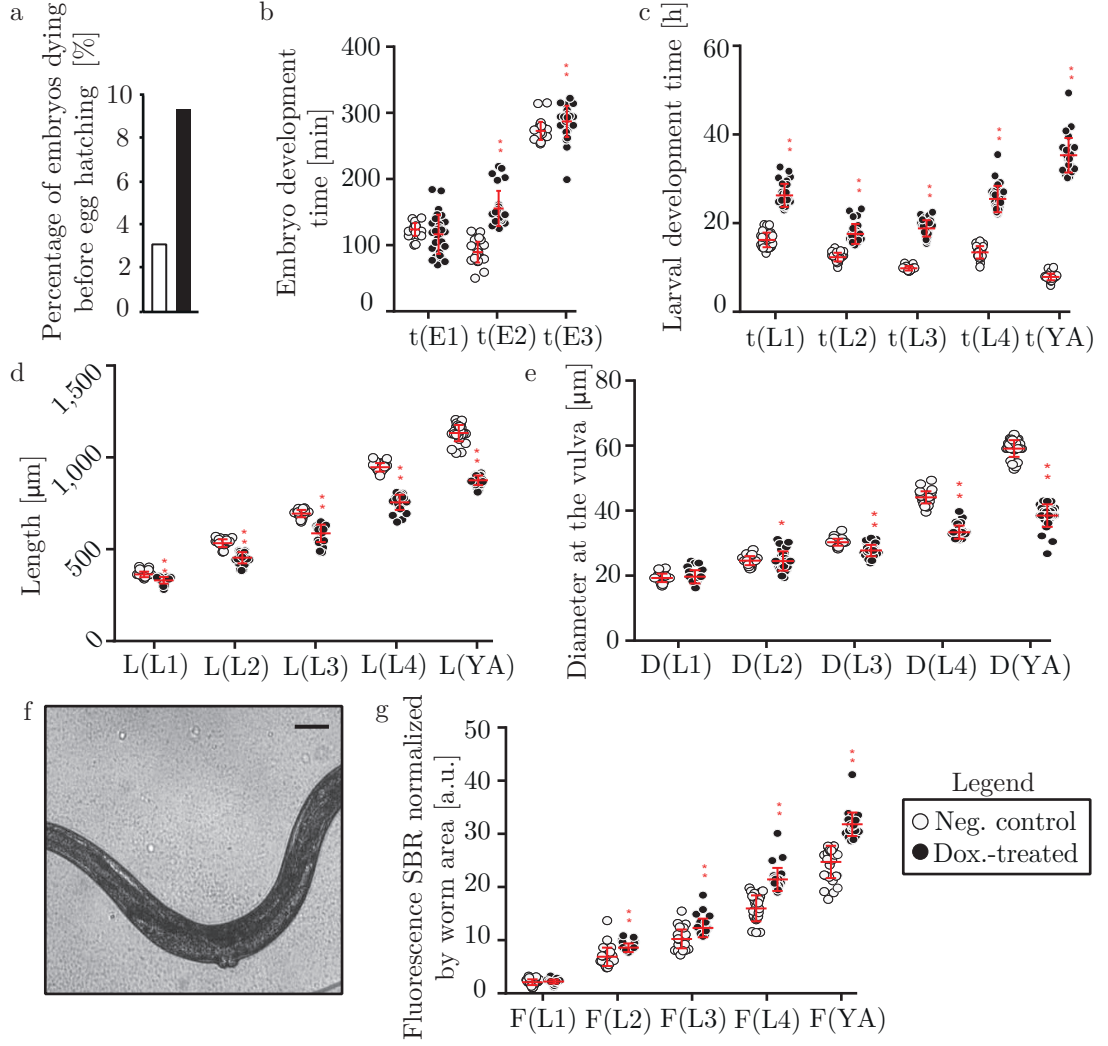
Figure 3.11 – Effect of doxycycline on the *C. elegans* life-cycle. a-e, Comparison between control and treated worms of a) percentage of embryos dying before egg hatching, b) the durations of embryonic developmental stages, c) the durations of larval developmental stages, d) the lengths and e) diameters at each larval stage. f) Brightfield picture of an adult treated worm showing no presence of eggs in the body. Scale bar = 50 μm. g) Comparison of SBR normalized by worm size at each larval stage between control and treated worms. N= 31 for control; N= 29 for the doxycycline treatment. Untreated *hsp-6p::gfp* worms are used as controls (Dataset in Figures 3.6, 3.7).
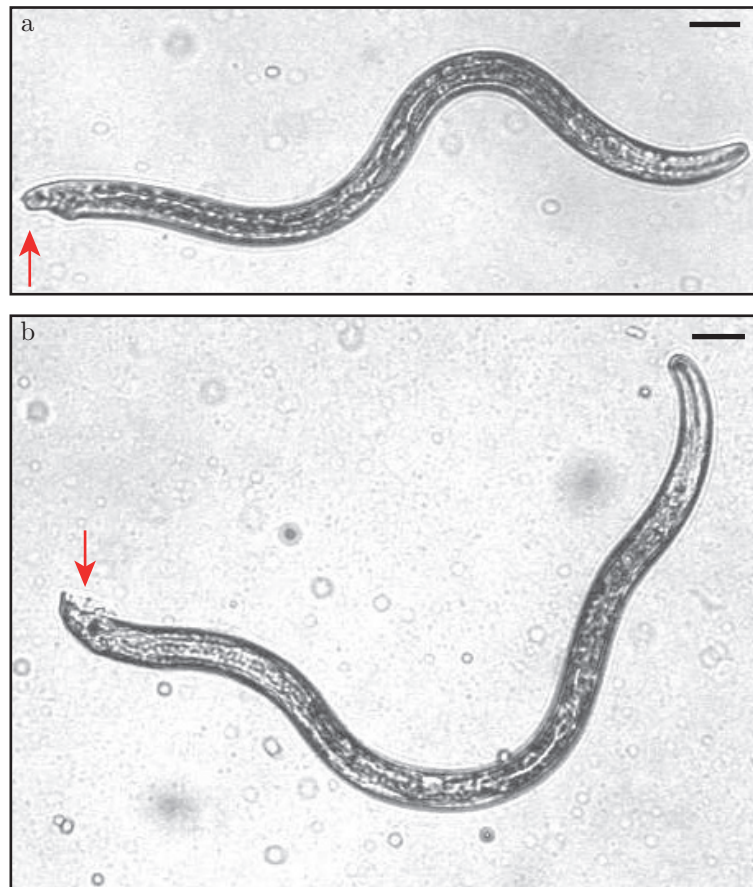
Figure 3.12 – Male individuals upon doxycycline treatment. a,b) Brightfield pictures of the two adult treated worms that expressed a male sex. The arrows point at the typical blunt-ended male tail. Scale bar = 50 μm.

Phenot.	PC 1 (50.6% of variance)		PC 2 (33.2% of variance)		PC 3 (5.2% of variance)	
	Coordin.	Contrib.	Coordin.	Contrib.	Coordin.	Contrib.
t(E1)	0.071	0.030	-0.048	0.014	0.078	0.024
t(E2)	0.115	0.048	-0.147	0.042	-0.246	0.075
t(E3)	0.002	0.001	0.004	0.001	0.098	0.030
t(L1)	-0.009	0.004	-0.278	0.079	-0.017	0.005
t(L2)	-0.005	0.002	-0.234	0.067	0.137	0.042
t(L3)	0.106	0.044	**-0.393**	**0.112**	0.254	0.078
t(L4)	0.056	0.023	**-0.452**	**0.129**	**0.549**	**0.168**
t(YA)	**0.852**	**0.357**	-0.138	0.039	-0.218	0.067
L(L1)	-0.065	0.027	0.127	0.036	0.066	0.020
L(L2)	-0.060	0.025	0.076	0.022	0.041	0.013
L(L3)	-0.021	0.009	0.083	0.024	0.043	0.013
L(L4)	-0.002	0.001	0.136	0.039	0.149	0.046
L(YA)	0.168	0.071	**0.467**	**0.133**	0.091	0.028
F(L1)	-0.074	0.031	0.262	0.075	**0.420**	**0.129**
F(L2)	0.101	0.042	0.102	0.029	0.104	0.032
F(L3)	0.108	0.045	0.153	0.044	0.137	0.042
F(L4)	0.207	0.087	0.110	0.031	**0.478**	**0.147**
F(YA)	**0.366**	**0.153**	0.292	0.083	0.138	0.042

Table 3.3 – Coordinates and contributions of PCs 1, 2 and 3 as result of PCA of phenotypes of control and RNAi-treated group on *mrps-5* gene. Phenotypes with significant contribution are marked in bold.
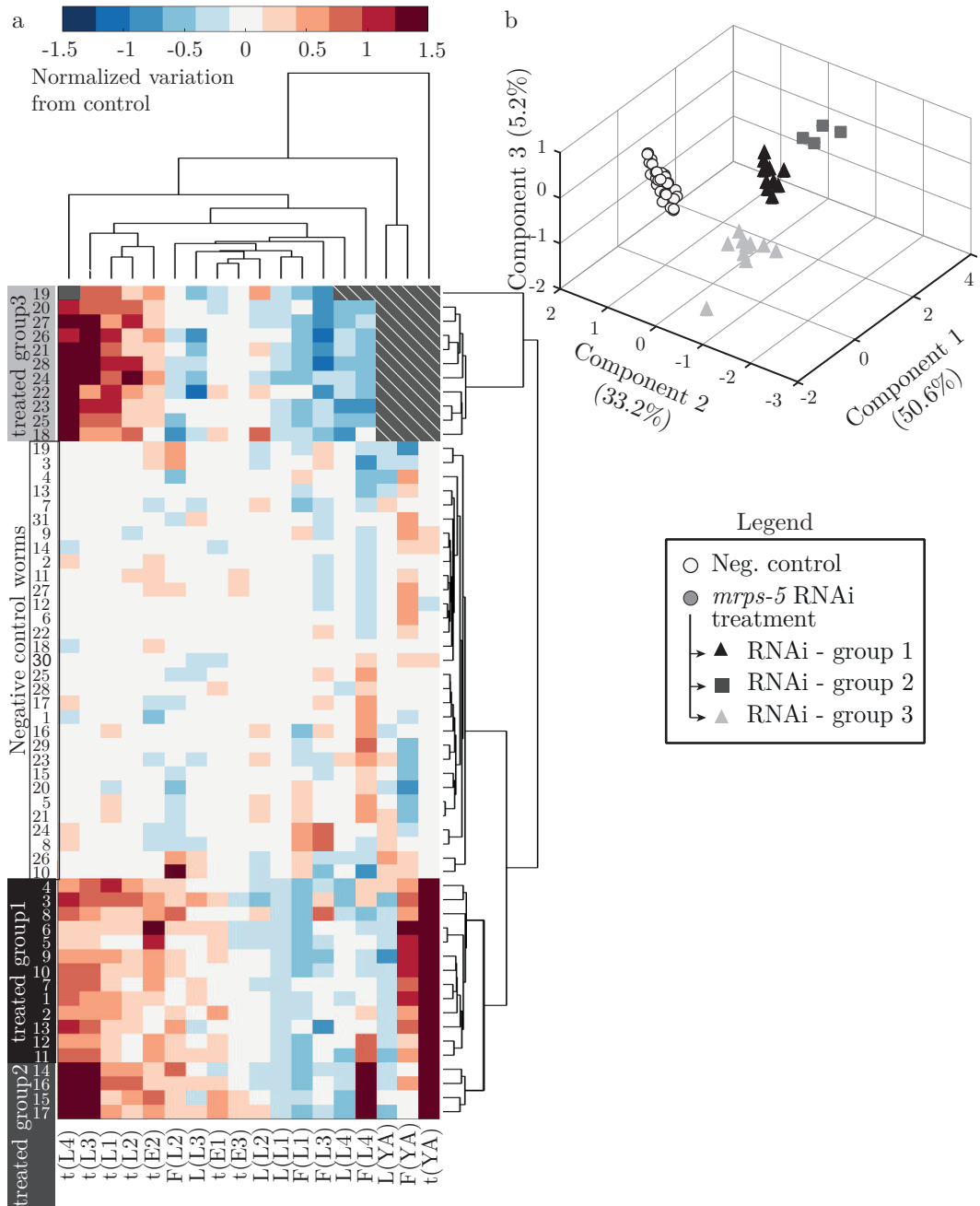
Figure 3.13 – Phenotypic footprint of phenotypes of the control group and the *mrps-5*-treated group. a) HCA of phenotypes of the control group and the *mrps-5*-treated group. The grey dashed area indicates missing data points, corresponding to the worms who did not complete their development. b) PCA of phenotypes of control and *mrps-5*-treated groups. Single-worm data are arranged according to the first, second and third PC of worms phenotypes.

Phenotype	PC 1 (61.7 % of variance)		PC 2 (24.6 % of variance)	
	Coordinates	Contributions	Coordinates	Contributions
t(E1)	-0.030	0.011	-0.096	0.028
t(E2)	0.027	0.010	0.258	0.075
t(E3)	0.004	0.001	-0.068	0.020
t(L1)	0.074	0.028	0.330	0.096
t(L2)	0.054	0.020	0.193	0.056
t(L3)	0.058	0.022	**0.471**	**0.137**
t(L4)	**0.483**	**0.180**	0.024	0.007
t(YA)	**0.686**	**0.256**	0.324	0.095
L(L1)	-0.014	0.005	-0.062	0.018
L(L2)	-0.003	0.001	-0.008	0.002
L(L3)	0.008	0.003	0.049	0.014
L(L4)	0.219	0.082	-0.337	0.098
L(YA)	0.169	0.063	**-0.416**	**0.121**
F(L1)	-0.049	0.018	-0.055	0.016
F(L2)	.0078	0.029	-0.175	0.051
F(L3)	0.116	0.043	-0.088	0.026
F(L4)	**0.286**	**0.107**	-0.265	0.077
F(YA)	**0.321**	**0.120**	-0.207	0.060

Table 3.4 – Coordinates and contributions of PCs 1 and 2 as result of PCA of phenotypes of control and RNAi-treated group on *cco-1* gene. Phenotypes with significant contribution are marked in bold.

they never reached the YA stage (Figure 3.14c). Moreover, UPR^{mt} activation in group 3 was very weak (Figure 3.14f,g), compared to worms from the previous groups and even from the control. Finally, 93% of worms were infertile (Figure 3.15a), as confirmed by impaired gonad development and absence of internal progeny (3.15b).

3.6.2 RNAi treatment on *cco-1* gene induces two sub-population-specific responses

A similar heterogeneity was observed after *cco-1* RNAi treatment upon HCA and PCA (Figure 3.16 and Table 3.4).

  RNAi on *cco-1* gene homogeneously induced a significant difference on t(E2) and t(E3) (Figure 3.17a). Moreover, 22% of the embryos died before hatching (Figure 3.17b). The analysis of the dendrogram and heat map resulting from the HCA, as well as PCA (Figure 3.16), revealed the presence of subgroups 1 and 2, accounting respectively for 72% and 28% of the treated worms. Larval development times and body volumes were similar to control during the L1 and L2 stages for both subgroups (Figure 3.17c-e). However, the UPR^{mt} activation was attenuated in group 2 during these first larval stages (Figure 3.17f,g) compared to both the control and group 1. Interestingly, group 2 worms died
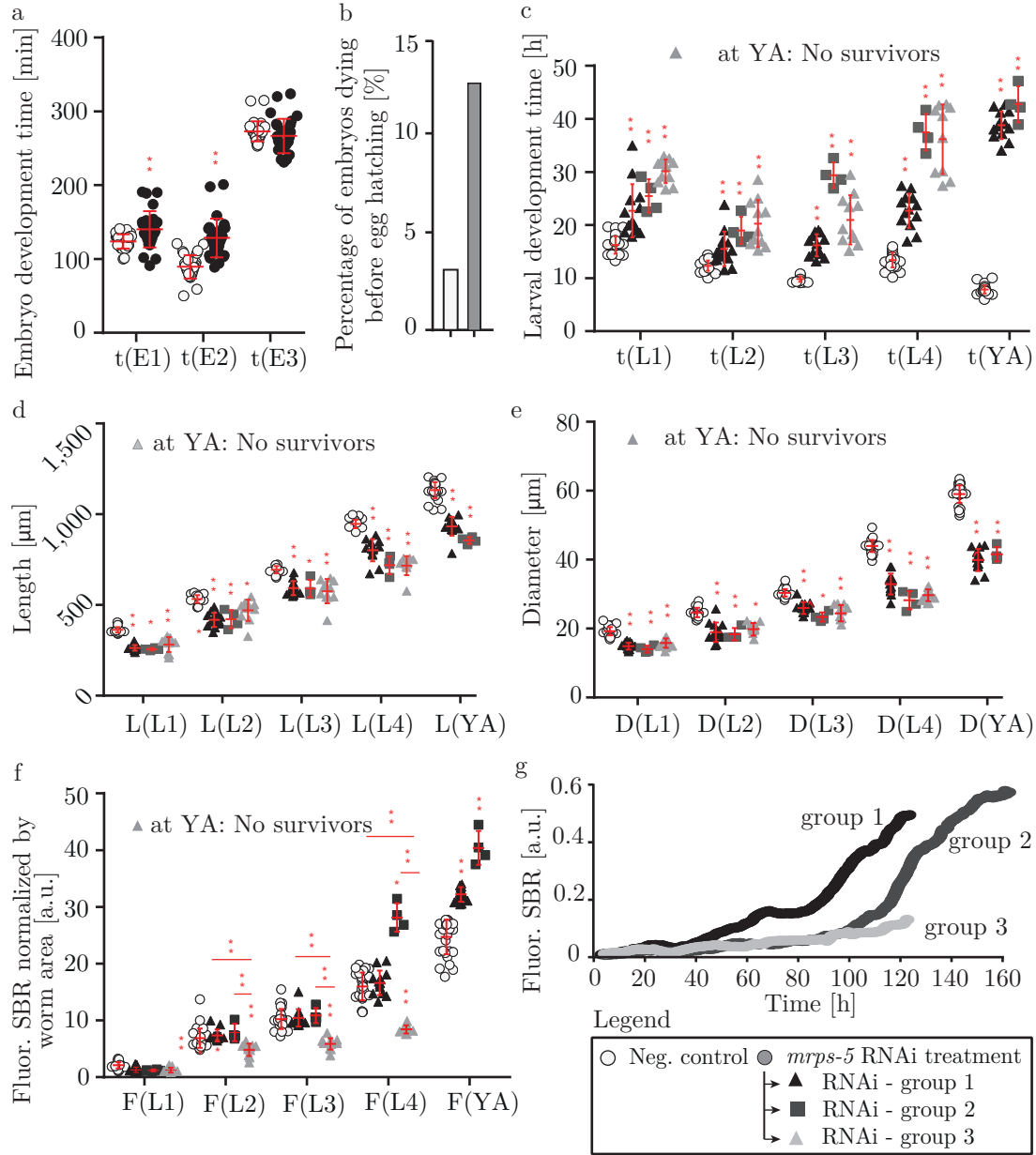
Figure 3.14 – Effect of *mrps-5* RNAi treatment on the *C. elegans* life-cycle. Comparison between control and treated worms of a) the durations of embryonic developmental stages and b) the percentage of embryos dying before egg hatching. c-f, Comparison between control and sub-populations corresponding to groups 1, 2 and 3 of treated worms of c) the durations of larval developmental stages, d) the lengths and e) the diameters at each larval stage, and f) SBR normalized by worm size at each larval stage. g) Quantification of fluorescent *hsp-6p::gfp* expression as SBR for full life-cycle from group 1, group 2 and group 3 of treated worms. N= 31 for control; N= 28 for the *mrps-5* treatment. Untreated *hsp-6p::gfp* worms are used as controls (Dataset in Figures 3.6, 3.7).

Figure 3.15 – Effect of *mrps-5* RNAi treatment on the *C. elegans* fertility. a) Comparison of the percentage of fertile adults between control and treated worms. b) Brightfield picture of an adult treated worm. Scale bar = 50 μm. N= 31 for control; N= 28 for the *mrps-5* treatment. Untreated *hsp-6p::gfp* worms are used as controls (Dataset in Figures 3.6, 3.7).

after the L3 stage, thus not completing their life-cycle (Figure 3.17c). Moreover, even if worms from group 1 survived, impaired gonad development and 100% infertility were observed (Figure 3.18).

Our analysis showed that alteration of the mitochondrial function through genetic manipulation leads to remarkable changes during the developmental phases, which are strongly dependent on mitochondrial activity. Interestingly, as expected in a RNAi approach, populations treated with *mrps-5* and *cco-1* RNAi showed a significant heterogeneity during larval development.

3.7 Materials and methods

3.7.1 Image processing

Image processing was performed with ImageJ software and Matlab R 2015b software (MathWorks, US), on each stack of brightfield and fluorescent worm images. Brightfield pictures were processed in order to spot bean stage onset, twitching onset, hatching, molting times and appearance of protruded vulva for each individual. The number of surviving embryos was assessed by counting the number of hatching eggs. For each larval stage, length and diameter (or width, as the worms are assumed cylindrical) were calculated and averaged over 5 brightfield pictures at the central time point of the larval stage for each individual. In order to assess fertility, we looked for the presence of internal embryos from self-fertile reproduction after vulva protrusion. To extract fluorescent SBR ratio, the region of interest (ROI) corresponding to the worm area was first segmented in the whole stack. We performed background subtraction and applied a median filter in order to remove salt-and-pepper noise. SBR was then calculated for each picture as defined in Equation 3.1

$$SBR = \frac{I_{ROI} - I_{BG}}{I_{BG}} \tag{3.1}$$

45
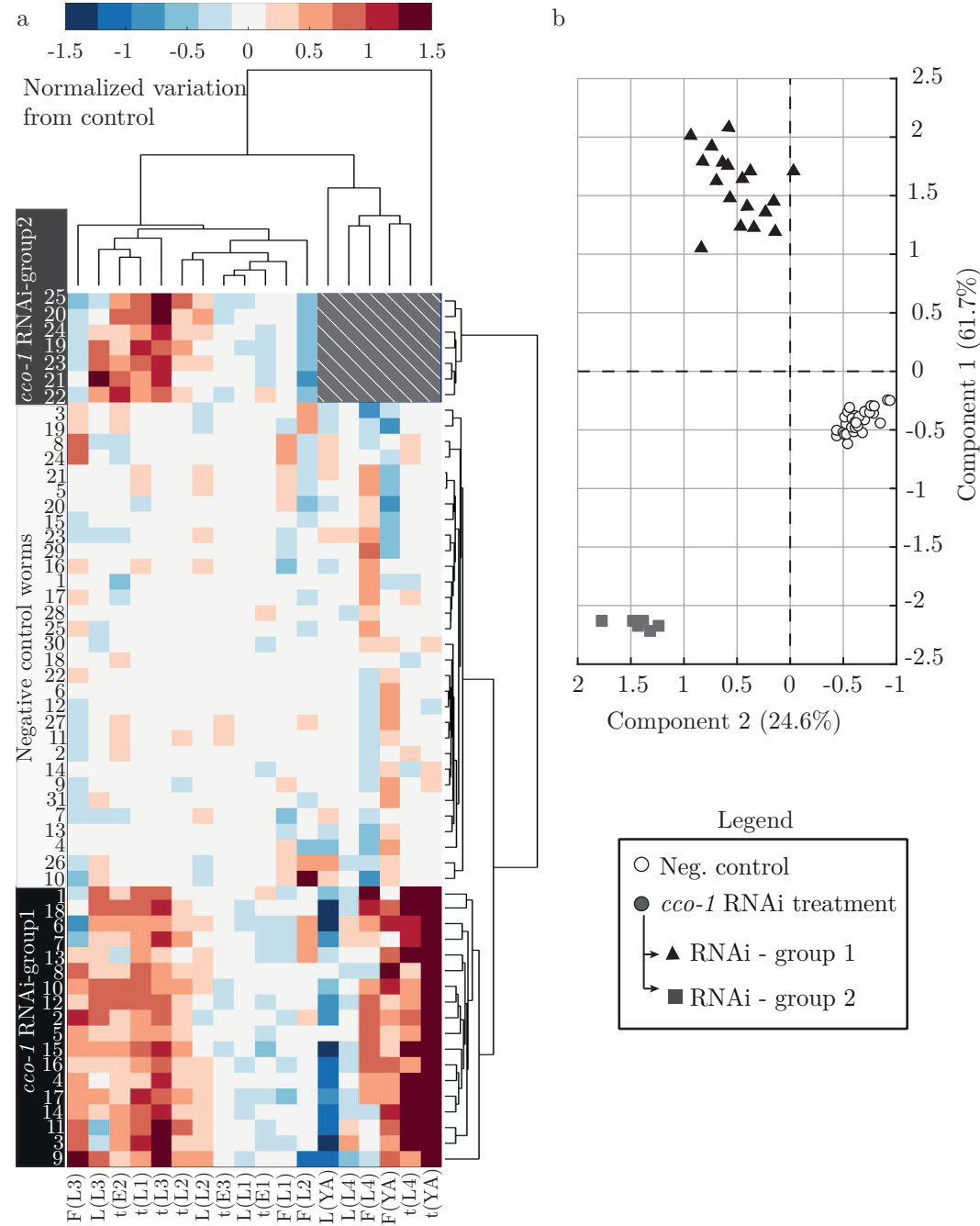
Figure 3.16 – Phenotypic footprint of phenotypes of the control group and the *cco-1*-treated group. a) HCA of phenotypes of the control group and the *cco1*-treated group. The grey dashed area indicates missing data points, corresponding to the worms who did not complete their development. b) PCA of phenotypes of control and *cco-1*-treated groups. Single-worm data are arranged according to the first and second PC of worms phenotypes.
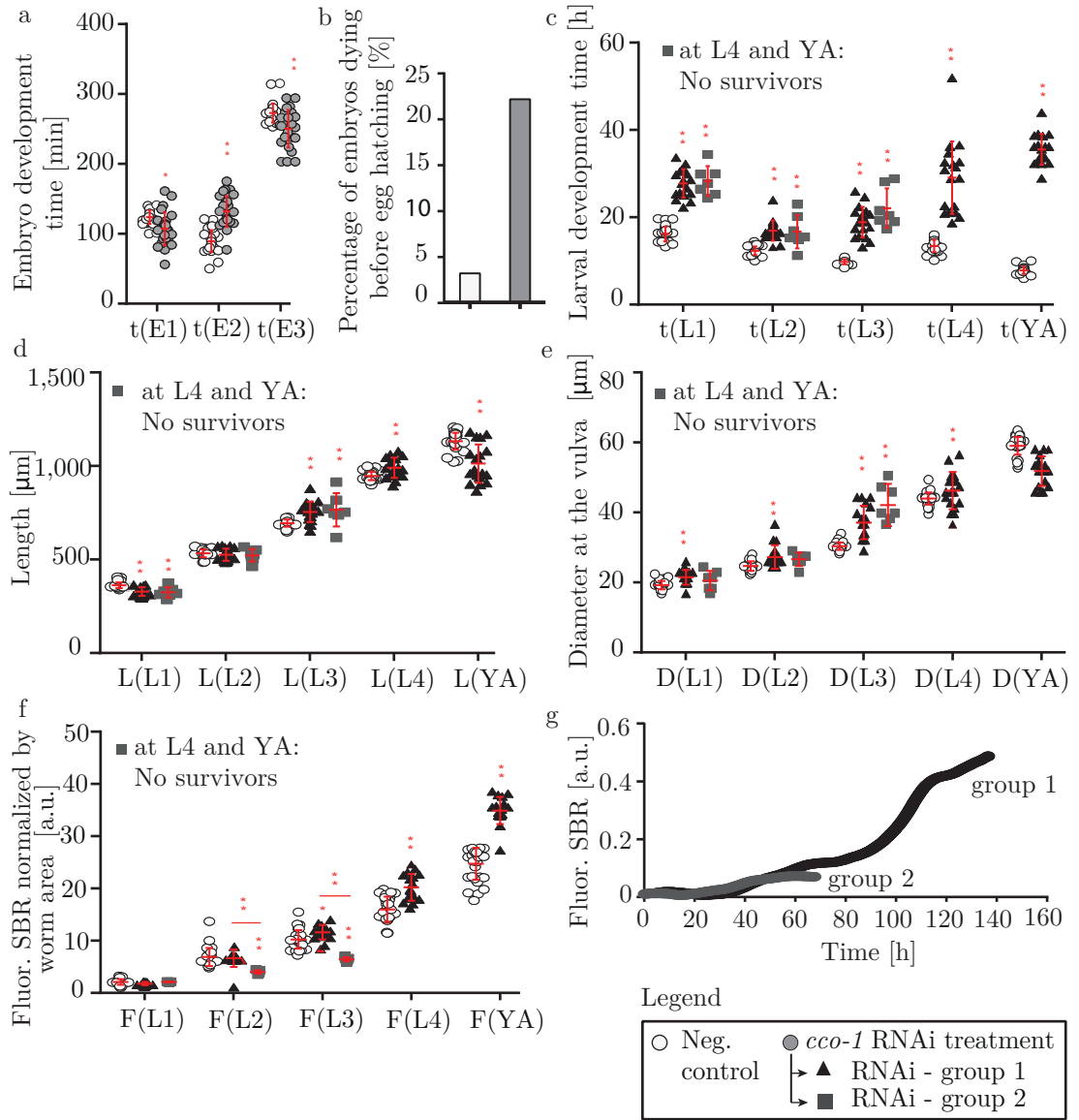
Figure 3.17 – Effect of *cco-1* RNAi treatment on the *C. elegans* life-cycle. Comparison between control and treated worms of a) the durations of embryonic developmental stages and b) the percentage of embryos dying before egg hatching. c-f, Comparison between control and sub-populations corresponding to groups 1 and 2 of treated worms of c) the durations of larval developmental stages, d) the lengths and e) the diameters at each larval stage, and f) SBR normalized by worm size at each larval stage. g) Quantification of fluorescent *hsp-6p::gfp* expression as SBR for full life-cycle from group 1 and group 2 of treated worms. N= 31 for control; N= 25 for the *cco-1* treatment. Untreated *hsp-6p::gfp* worms are used as controls (Dataset in Figures 3.6, 3.7).

Figure 3.18 – Effect of *cco-1* RNAi treatment on the *C. elegans* fertility. Brightfield picture of an adult treated worm. Scale bar = 50 μm.

with I$_{ROI}$ the average intensity of the signal in the ROI and I$_{BG}$ the average intensity of the background. In order to remove noise and artifacts from the obtained SBR, a moving average filter (length of moving window = 10 frames) was applied on the stack.

3.7.2   Experimental model and subject detail

C. elegans strains were cultured at 20 °C on NGM 90 mm Petri dishes seeded with *E. coli* strain OP50. The strain used in this study was the SJ4100 (zcIs13[hsp-6p::GFP]), provided by the Caenorhabditis Genetics Center (University of Minnesota). For studies in untreated conditions, *hsp-6p::gfp* worms were plated on regular NGM plates at the L4, and collected about 12 hours later at the stage of YA for injection in the system. For the doxycycline treatment, a concentration of 30 μg/mL was chosen to trigger UPR^{mt} in *hsp-6p::gfp* worms. Adult gravid worms were placed on control plates and removed after 6 hours after egg laying. YA worms from the second generation were then collected for introduction in the microfluidics system, where the treatment with the antibiotic (30 μg/mL) was initiated after egg laying. For the NR treatment experiments, *hsp-6p::gfp* worms were grown on regular NGM plates at 20 °C until reaching the L4 stage and then transferred to new plates for treatment (parental generation, F0). NR (1mM) was added just before pouring the plates. The derived NR-treated (F1 generation) population was collected at the stage of YA for introduction in the microfluidics system. For RNAi studies, plates were induced overnight at room temperature with 4 mM isopropyl β-D-1-thiogalactopyranoside (IPTG) and seeded with HT115 bacteria expressing either empty vector RNAi L4440 or the RNAi clones for the indicated genes. F0 adults were removed after 24 h and F1 YA worms were collected for introduction in the microfluidics system. Worms were suspended in S medium solution prior to each microfluidic experiment.

3.7.3   *E. coli* culture

HT115 *E. coli* bacteria were grown in luria broth (LB) with 100 μg/mL ampicillin and 12.5 μg/mL tetracycline overnight in a thermal shaker at 37 °C. The following day, 50 μL of the confluent bacterial cultures were used to inoculate freshly prepared LB medium

containing only ampicillin, so to avoid the presence of tetracycline during the worm experiments, which has been shown to also affect mitochondrial function, similarly to doxycycline [54]. The new cultures were grown until reaching an optical density between 0.6 and 0.8, and 90 μL were used for seeding the experimental plates. To feed worms in the microfluidic device, a solution of bacteria in S medium with optical density of 5 was prepared and used.

3.7.4 Quantification and statistical analysis

Statistical analysis was performed using GraphPad Prism (San Diego, CA, US). Graphs are expressed as mean $\pm$ SD overlaid with a cloud of points describing the actual dataset, unless otherwise as indicated in the figure legends. For each treatment, the datasets were independently obtained from two chips, each featuring 16 worm chambers. The sample number (N) indicates the number of independent viable biological samples for which parameters were extracted in each dataset. Statistical significance was determined with a two-tailed Mann-Whitney test. p-values were graphically reported as * $p \leq 0.05$, ** $p \leq 0.01$. Statistical tests were performed only to compare the recorded values of a given phenotypic parameter, at a specific developmental stage, amongst different treatments/groups of worms.

The on-chip analysis provided a multitude of phenotypic variables which precluded the identification of major phenotypic changes in response to the experimental conditions. As a consequence, we used a HCA and PCA to reduce the dimensionality of the datasets and emphasize the driving force that generated the raw data.

Hierarchical cluster analysis

The input experimental variables were the durations of the embryonal stages of development, the durations of the five stages of larval development, the length at the L1 stage and length increments at the other four stages of larval development, and the fluorescent SBR at L1 stage and the SBR increments at the other four stages of larval development. Increments, rather than absolute measurements, were used here to minimize the risk of unwanted correlations between parameters which are expected to increase as the worm develops (for instance the length), which may hide smaller variations between the treatments. Each dataset was normalized and centered to the average of each parameter for the negative control, and a hierarchical cluster analysis was run using the built-in algorithm in Matlab R 2015b (MathWorks, US). Data points were organized in clusters ordered according to the unweighted average Euclidean distance.

Principal component analysis

As data was spread over a wide range of units and scales, data was normalized to the mean of each parameter (obtained over all the worms for a specific condition, *i.e.* control and treatment) before performing PCA. This allowed for the direct comparison of the different parameters while still preserving the variability of the data, in regard to the average, hence allowing for the extraction of the discriminant markers. Additionally, the algorithm used here centers the dataset by default. A PCA procedure was run using the built-in algorithm in Matlab R 2015b (MathWorks, US). The components were then ranked by decreasing order of explained variance (or eigen-value). The data was then plotted using this new base, and the components revealing the separation of specific subgroups were kept for the analysis. For each retained component the contribution of the initial parameters was computed by normalizing the coordinates of the component to the L^1 norm of the component (*i.e.* the sum of all the absolute values of the coordinate for this component). Only the parameters whose contribution was at least 10% of the component were considered. Finally, by considering the projection of the raw data on the relevant components (*i.e.* by considering the scores) and the parameters contributing to this component, the discriminant parameters for specific subgroups were identified. Using this approach, the contribution of each phenotypic observation could be evaluated, and the input variables with the highest information content isolated.

3.8   Discussion and conclusion

The platform and analysis method were used to identify appropriate biomarkers and investigate the phenotypic variability associated with the nematode UPR^{mt}. In worms treated with doxycycline [54] or fed with bacteria expressing RNAi for *mrps-5* [51] and *cco-1* [44] to induce UPR^{mt}, the classic phenotypic hallmarks of mitochondrial stress were observed, such as delayed development, reduced brood size, reduced fertility and induction of the UPR^{mt} biomarker *hsp-6p::gfp*. On the other hand, NR did prolong the *C. elegans* life-cycle, without compromising either embryonal viability or worm fertility, and the UPR^{mt} was weakly activated. The setup revealed a treatment-dependent intra-population variability that could otherwise not be observed in RNAi experiments run on plates. Interestingly, exposure to small molecules, *i.e.* doxycycline and NR, induced homogenous responses in comparison to *mrps-5* and *cco-1* RNAi, where very distinct outcomes were recorded. A possible contributor to this increased heterogeneity during RNAi treatment is the variability in the transmission of the acquired traits, as the RNAi pretreatment and conditioning started with the L4 parental worm generation.

Quantifying and elucidating the patterns linking markers to heterogeneous responses amongst treated individuals is a paramount prerequisite in precision medicine research. However, this variability in phenome data read-out is often lost owing to the lack of specific strategies to tackle this huge analytical challenge. Consequently, we described here a platform that allows culturing and phenotyping of individual worms from a *C.*

elegans population from egg laying until adulthood. Thanks to hydrodynamic trapping, freshly-laid single embryos were automatically isolated and kept in separate chambers until adulthood. The single-worm resolution of our chip allowed the longitudinal monitoring and tracking of multiple phenotypes over the life-cycle of individual organisms. Moreover, worms showed a physiological development consistent with the one in solid medium at the same temperature, thus setting a new standard in terms of *C. elegans* culture and feeding in liquid environment. Therefore, with respect to previous studies on *C. elegans* culture [47], [66] and its use in drug testing [67], we showed a comprehensive microfluidic platform enabling unprecedented *C. elegans* culture over its full life-cycle at the single-worm level while longitudinally monitoring multiple phenotypic markers upon a variety of treatments. In fact, the platform allowed testing pharmacological and genetic treatments by simply changing the compounds injected into the microfluidic chip, while ensuring perfect control and reproducibility of all the environmental parameters. Conjugating longitudinal assays over the full development span with individualized observations in a precisely controlled chemical environment is a clear advancement of the state of the art and a substantial improvement of the previously proposed analytical microfluidic platforms for *C. elegans*. This phenotyping strategy paves the way for the identification of appropriate disease biomarkers that would shape the worm response to the treatment of interest, which would complement ideally similar studies performed on other species (reviewed in [68]). To compare the high-content phenotypic signature of worm populations under different conditions, we used single-worm based HCA and PCA. Big data strategies facilitate the identification of sub-groups and patterns buried in the phenome data. Our method also evaluated quantitatively the differences between different sub-groups, and provided the phenotypic footprint of each treatment. Envisioning a stratified medicine, the characterization of such intra-population treatment-dependent variability allows both inferring the effectiveness of a treatment in a population subset and identifying personalized follow-up treatments.

After having identified the different sub-groups of a population thanks to our unbiased and individualized analysis, it is possible to uncover significant trends characterizing the treatments, or the specific response biomarkers of a sub-group, by considering the average phenotypes within each sub-group. This analysis allowed for the identification of first-order treatment-specific effects and more global characterization of each experimental condition, as summarized in Figure 3.19. The sub-groups showed two different trends with respect to the negative control, based on the presence or absence of activation of the mitochondrial stress response and the severity of developmental delay. On one side, the third *mrps-5* group and in a more severe fashion the second *cco-1* group showed inappropriate stress-response activation and even impossibility to reach adulthood. On the other side, all the other groups - from NR-treated worms to the second *mrps-5* group - showed a progressive increased ability to respond to stress, as testified by UPR^{mt} activation, slow growth and reduced size during L4 and YA stages of development.
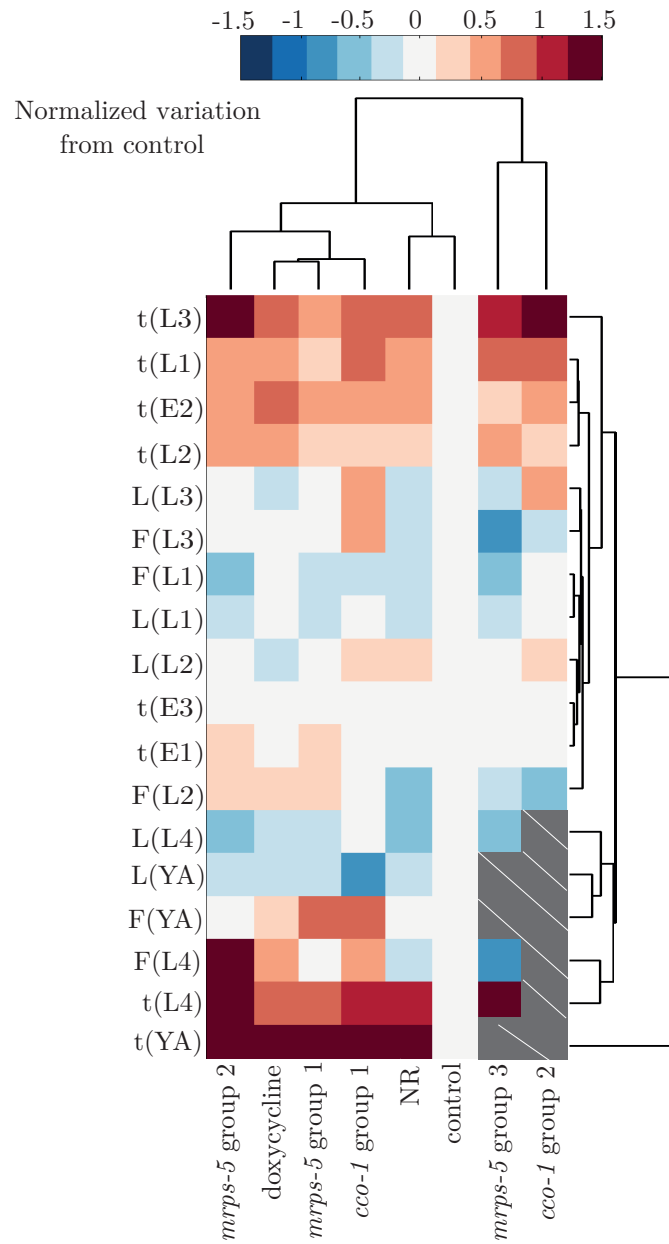
Figure 3.19 – Comprehensive high-content phenotypic picture of pharmacological and genetic treatments effects on *C. elegans* life-cycle. This hierarchical cluster analysis was based on the average phenotypes within the control group and treated group, the latter eventually showing distinct sub-groups. The grey dashed area indicates missing data points, corresponding to the worms that did not complete their development.

3.9   Future outlook

In the future, if worms are cultured and fed for a longer time, a life-long phenotypic analysis - from embryogenesis to death - could be performed. This would require adaptation of the feeding protocol to the adult metabolism of the animals during progeny production and in the last period of their life. A life-long study at single animal resolution would also require the periodic removal of progeny (L1) from the chamber, which we implemented already by providing the single worm chambers with filters through which L1 worms could escape under high fluidic pressure. Such a platform would be instrumental to study the effect of compounds related to worms ageing and degenerative diseases.

The possibility to precisely control the drug delivery in time could be further exploited in the future, by administering the drug at different time points, thereby fine-tuning the animal exposure to the drug of interest. Preliminary experiments were performed by exposing *C. elegans* to doxycycline from the L1 stage. The results confirmed the effect of doxycycline on the extension of the larval development time and on the worms size (Figure 3.20a,b), phenomena that were already observed at a more severe extent upon administration of doxycycline from the egg laying stage (Figure 3.11). More interestingly, 84.6% of worms were fertile (Figure 3.20c) and all the animals developed as hermaphrodite. These results strongly differ from the infertility and the presence of male worms observed upon life-cycle-long administration of doxycycline. Despite the cell lineages that generate the two sexes are clear variant of each other starting from the early cell divisions [69], our finding might hint that sex determination could possibly be modified during embryonic development.
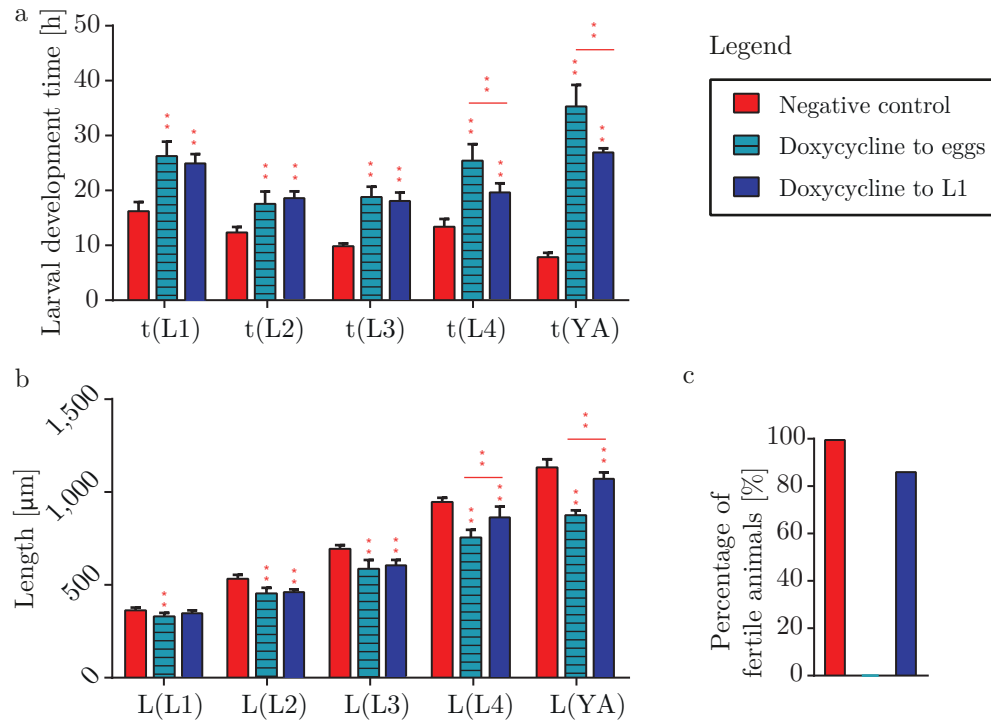
Figure 3.20 – Effect of doxycycline on *C. elegans* larval development. Comparison among control and worms treated with doxycycline for life-cycle and larval development of a) the duration of the larval developmental stages, b) the lengths at each larval stage and c) the percentage of fertile animals. Untreated *hsp-6p::gfp* worms are used as controls (Dataset in Figures 3.6, 3.7). The dataset related to worms treated over the full life-cycle is the same as the one represented in Figure 3.11.

4 Design of experiment approach for multi-parametric drug testing using a *C. elegans* model

Abstract When studying drug effectiveness on a target model, one should distinguish the effects of the drug itself and of all the other factors that could influence the screening outcome. A Design of Experiment (DoE) approach in drug-testing is emerging as a robust and efficient method to reduce the use of resources, while maximizing the knowledge of the process. Here, I used a 3-factor-Doehlert DoE to characterize the concentration-dependent effect of the drug doxycycline on the development duration of the nematode *C. elegans*. 13 experiments were designed and performed, where different doxycycline concentrations were tested, while varying also the temperature and the food amount, which are known to influence too the duration of the *C. elegans* development. A microfluidic platform was designed to isolate and culture *C. elegans* larvae, while testing the doxycycline effect with full control of temperature and feeding over the entire development. This approach allowed predicting the doxycycline effect on the *C. elegans* development in the complete drug concentration/temperature/feeding experimentation space, maximizing the understanding of the effect of this antibiotic on the the *C. elegans* development.

This chapter is an adapted version of the following publications:

- **M. C. Letizia**, M. Cornaglia, G. Tranchida, R. Trouillon, M. A. M. Gijs, "Design of experiment approach for efficient multi-parametric drug testing using a *Caenorhabditis elegans* model", *Integr. Biol.*, Issue 10, p. 48-56, 2018.
- **M. C. Letizia**, M. Cornaglia, M. A. M. Gijs, "Integrated temperature control system for microfluidic culture of nematodes". Proc. of 5th Micro and Nano Flows Conference (MNF2016), Milan, Italy, September 2016.
  Oral presentation

4.1 Introduction

Drug discovery and testing research are mostly based on a one-factor-at-a-time variational approach, in which each experimental parameter is changed at a time, independently of the others [70], [71]. However, this approach inevitably requires an impressively-high number of experiments to cover the entire experimental domain, which makes the drug development costly and time-consuming, limiting the discovery of the number of hits that exhibit interaction with the biological target of choice. Moreover, this technique is less prone to studying the effect of the simultaneous change of several factors on the final outcome. Similarly, the one-factor-at-a-time approach hinders the identification of a causal relationship between the experimental parameters and their influence on the target, or compromises discovery of interactions between the parameters. A robust alternative to this traditional drug discovery method is given by the so-called DoE approach, whose application in the quality-oriented pharmacological sector was recently recommended by the European Medicine Agency (EMA) [72]. In this method, the experimental parameters, called factors, are purposefully varied according to a precise design, in order to understand their effect on the target response, and a mathematical relationship is established between the factors and the response [73]. In a DoE approach, statistical thinking is therefore required before performing experiments rather than doing it *a posteriori*, like in a one-factor-at-a-time-approach [71]. DoE enables minimizing the use of the experimental resources while maximizing the knowledge of the process. In fact, it allows identifying the significance of each factor and its effect on the experimental outcome, as well as determining the interaction between factors. Moreover, a DoE study allows to extrapolate in a rigorous mathematical way its findings into the complete experimental space [73].

We focused on characterizing the effect of the antibiotic doxycycline in a variable temperature and food concentration environment on the development time of *C. elegans* as animal model (see schematic in Figure 4.1).

Doxycycline is mostly employed in animal research to study biological pathways involved
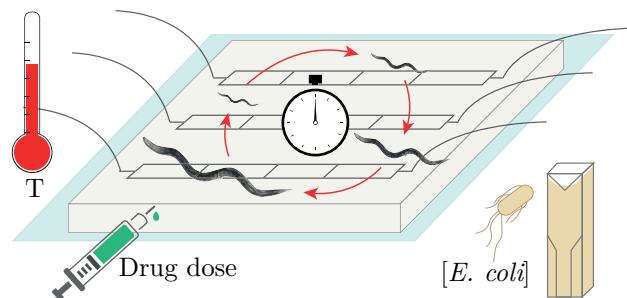
Figure 4.1 – Illustration of the DoE multi-parametric approach to investigate the change of the *C. elegans* development time by simultaneously varying temperature, food concentration and drug dose.

in the extension of longevity, and *C. elegans* represents a powerful model for such aging

and metabolism studies [42], [51], [54], [74], also thanks to its relatively-short life-span of 2-3 weeks [75]. In research, tetracycline antibiotics are generally used to control gene expression in a variety of animal models [54], [76]. However, beside targeting bacterial translation, doxycycline also inhibits mitochondrial translation, which is thought to be a key factor in the lifespan extension [51], [54]. Interestingly, it has been shown that doxycycline extends the lifespan of cells, worms, flies, plants and mice in a dose-dependent fashion [54]. It is known to induce mitochondrial stress, leading to changes in nuclear gene expression and to severely alter mitochondrial function in different animal models, including *C. elegans* and mice, even at low concentration [54]. Gravid worms and progeny were treated with doxycycline at concentrations of 60 μg/mL and 120 μg/mL [77]. In both cases, all the larvae arrested their development at the L3 stage, showed impaired gonad development and a dose-dependent delay in larval growth. Houtkooper et al. treated worms with doxycycline (30 μg/mL and 60 μg/mL) for the entire lifespan and noticed a dose-dependent developmental delay and reduced worm respiration, while no abnormalities were observed at lower doses [51]. Another group gave doxycycline to a worm population throughout its larval development at concentrations of 5 μg/mL, 10 μg/mL and 15 μg/mL [54]. Dose-dependent decrease of the respiration rate, increase of the development time and increase of the percentage of larvae not completing the development were observed. Recently, microfluidic approaches were used as an alternative to the traditional *C. elegans* culture on agar plates. Microfluidic chips for worm culture were fabricated and used to test the effect of doxycycline on worms [78]. In particular, doxycycline at a concentration of 15 μg/mL and 30 μg/mL, given to worms throughout their larval development, dose-dependently delayed the worm growth [78].

However, differences in the experimental and environmental parameters combined with a lack of control of the experimental protocols prevent the exact replication of these experiments and therefore limit the upfront comparison of the literature. Temperature [13] and food amount [79], [80] are in fact the two most relevant factors that modulate *C. elegans* development and longevity. For example, *C. elegans* development time can be 2.1-fold shorter at 25 °C than at 16 °C, and 1.3-fold shorter a 20 °C than at 16 °C [13]. *C. elegans* larvae sense the concentration of *E. coli* bacteria, with severe effect on their development time [49]. Under-fed worms can reach adulthood in twice the time it takes for normally-fed worms at the same temperature conditions [81]. Severe underfeeding conditions may even lead to a non-physiological development of the organism. On the other hand, overfeeding of wild type *C. elegans* may reduce their lifespan by 10-20% [82] and long-term overfeeding may eventually result in bacterial accumulation in the worm's mouth and intestine, leading to a diseased state [81], [83]. Moreover, the combination of temperature and feeding amount has important effects on *C. elegans* development and life-span. Low temperature and dietary restriction activate *C. elegans* pathways that shift physiology towards cell protection and maintenance, leading to a slower development and eventually to a longer life-span [80], [84]. However, interestingly, also exposure to high temperature, e.g. 25 °C, if combined with food deprivation and crowding during the larval development, may arrest the development or reversibly shift it towards a

long-lasting state of diapause called dauer stage [85], [86].

A precise dose-dependent characterization of the effect of doxycycline on *C. elegans*, with full control of the experimental parameters, namely temperature and feeding, is hence essential to provide rigorous culture conditions, but is currently lacking. The possibility to parallelize and automatize the experiments promotes microfluidic platforms as the most efficient tool to enable such a systematic characterization. Most of the experimental repertoire was obtained from traditional *C. elegans* cultures on solid medium, where the food amount is not quantified but is usually abundant [13]. Finding the right feeding protocol in liquid conditions that are corresponding to culture on solid agar plates is not straightforward and requires optimization. However, such characterization is of primary importance for performing reproducible experiments and comparing the results, to disentangle any variation of food concentration and temperature from the tested drug response. Moreover, after performing a DoE analysis using controlled liquid media to culture worms, the correct drug dose that has to be used to achieve the desired outcome can be predicted, therefore avoiding either side effects due to over-dosage or ineffective treatments due to a sub-optimal drug concentration.

In this study, I investigated the role of doxycycline on *C. elegans* development, combined with variations of temperature and concentration of *E. coli* as food source in a microfluidic platform. A 3-factor Doehlert DoE was chosen to characterize the effect of those 3 factors on the worm development. A microfluidic chip enclosed in a custom-made thermal incubator was designed, to culture *C. elegans* larvae with full control of the experimental parameters, especially temperature and injected food amount. The results revealed the relative importance of temperature, food concentration and doxycycline dose on the *C. elegans* development time. In particular, while doxycycline dose and temperature exerted a significant severe effect on the duration of the larval development, no significant development dependence on the *E. coli* concentration in the investigated range was found.

4.2 A 3-factors Doehlert experimental design and mathematical model

The factors under consideration were temperature (X_1), concentration of *E. coli* used as nutrient (X_2) and concentration of doxycycline (X_3). Temperature was considered in the range 15-25 °C, known as characteristic range for *C. elegans* survival [13]. The *E. coli* concentration was considered in the range 2-6 × 10^9 cell/mL, as values in this range were previously used to culture *C. elegans* worms in microfluidic chips [19]. Finally, given the doxycycline concentrations used in the previously reported experiments, the range 5-60 μg/mL was chosen for this third factor. The response (Y) was identified as the duration of the larval development, expressed in hours, from the stage L1 until the onset of adulthood and production of the first progeny. The application of a factorial 3-factor Doehlert design was well-suited to characterize the synergic effect of temperature,

Figure 4.2 – Representation of the factorial combinations in the experimental space, according to a 3-factor Doehlert design. 13 points are uniformly distributed in the experimental domain. X_1, X_2, X_3 represent respectively temperature, concentration of *E. coli* bacteria and concentration of doxycycline. The center point is the center of the interval for the three variables, therefore describing an experiment performed at a temperature of 20 °C, with an *E. coli* concentration of 4×10^9 cell/mL and a doxycycline concentration of 32.5 μg/mL.

concentration of *E. coli* and doxycycline on the larval development, as it offers a uniform distribution of points in the experimental domain. With k being the number of factors, the Doehlert design requires $k^2 + k + 1$ number of experiments, 13 in our 3-factor case. These 13 combinations can be geometrically positioned in the experimental space as the vertices of a cubo-octahedral, as represented in Figure 4.2. The coordinates used in the DoE model, called coded values, as well as the corresponding real experimental values of temperature, *E. coli* concentration and doxycycline concentration, are given in the model matrix in Table 4.1. Typically a coded value 1 corresponds to the highest value of an experimental parameter, -1 to the lowest value and 0 to the linearly-extrapolated center point.

 Experiments corresponding to the central point [0, 0, 0] were performed three times, to test their repeatability. In order to describe the development time Y as a function of the factors, a quadratic polynomial model was constructed, as described by the Equation 4.1:

$$\hat{y} = b_0 + b_1 X_1 + b_2 X_2 + b_3 X_3 + b_{11} X_1^2 + b_{22} X_2^2 + b_{33} X_3^2 + b_{12} X_1 X_2 + b_{13} X_1 X_3 + b_{23} X_2 X_3 \quad (4.1)$$

This model not only considers the linear factors, but also their interactions, $X_1 X_2$, $X_2 X_3$ and $X_1 X_3$ and their quadratic contributions X_1^2, X_2^2 and X_3^2 to the response. The validity of the quadratic model is confirmed *a posteriori* (*vide infra*). The model matrix containing also the interactions and quadratic values of the factors is presented in Table 4.2.

N	Coded values			Experimental parameter values		
	X_1	X_2	X_3	Temperature °C	[*E. coli*] $\times 10^9$ cell/mL	[Doxycycline] μg/mL
1	0	0	0	20	4	32.5
2	1	0	0	25	4	32.5
3	0.5	0.866	0	22.5	5.73	32.5
4	0.5	0.289	0.816	22.5	4.58	54.96
5	-1	0	0	15	4	32.5
6	-0.5	-0.866	0	17.5	2.27	32.5
7	-0.5	-0.289	-0.816	17.5	3.42	10.03
8	0.5	-0.866	0	22.5	2.27	32.5
9	0.5	-0.289	-0.816	22.5	3.42	10.03
10	-0.5	0.866	0	17.5	5.73	32.5
11	0	0.577	-0.816	20	5.15	10.03
12	-0.5	0.289	0.816	17.5	4.58	54.96
13	0	-0.577	0.816	20	2.85	54.96

Table 4.1 – Coded values and corresponding values of the experimental parameters temperature (X_1), *E. coli* concentration (X_2) and doxycycline concentration (X_3).

N	I	X_1	X_2	X_3	X_1X_2	X_1X_3	X_2X_3	X_1^2	X_2^2	X_3^2
1	1	0	0	0	0	0	0	0	0	0
2	1	1	0	0	0	0	0	1	0	0
3	1	0.5	0.866	0	0.433	0	0	0.25	0.749	0
4	1	0.5	0.289	0.816	0.144	0.408	0.235	0.25	0.083	0.665
5	1	-1	0	0	0	0	0	1	0	0
6	1	-0.5	-0.866	0	0.433	0	0	0.25	0.749	0
7	1	-0.5	-0.289	-0.816	0.144	0.408	0.235	0.25	0.083	0.665
8	1	0.5	-0.866	0	-0.433	0	0	0.25	0.749	0
9	1	0.5	-0.289	-0.816	-0.144	-0.408	0.235	0.25	0.083	0.665
10	1	-0.5	0.866	0	-0.433	0	0	0.25	0.749	0
11	1	0	0.577	-0.816	0	0	-0.470	0	0.332	0.665
12	1	-0.5	0.289	0.816	-0.144	-0.408	0.235	0.25	0.083	0.665
13	1	0	-0.577	0.816	0	0	-0.470	0	0.332	0.665

Table 4.2 – Full model matrix of coded values of the experimental parameters temperature (X_1), *E. coli* concentration (X_2) and doxycycline concentration (X_3), their interactions and quadratic values.

4.3 Design and fabrication of the microfluidic chip for controlled _C. elegans_ culture and analysis

In order to test the 13 combinations of the three factors that contribute to the experimental variability and to unravel the influence on the DoE study, a microfluidic chip dedicated to the on-chip culture of _C. elegans_ throughout its larval development was designed and fabricated in PDMS and glass, following the fabrication steps described in Chapter 2. In fact, compared to heaviliy manual and laborious traditional _C. elegans_ culture protocols [13], microfluidics enables automated, more robust and reproducible culture experiments [19], [20], [43]. By matching the channels' dimension with the worm size, _C. elegans_ larvae of the desired stage can be automatically filtered and the population can consequently be synchronized [47]. Moreover, by using dedicated syringe pumps, the feeding protocol can be first optimized and standardized, and then repeatedly executed in an automated way.

The design of our microfluidic device is shown in Figure 4.3a. The chip features 8 independent channels. The heigth of the microfluidic chambers and channels is 80 μm. Each channel is an array of 6 chambers separated by filters, to culture isolated worms and preserve their identity (Figure 4.3b). The 5 μm-feature filters are designed to prevent the uncontrolled passage of L1 larvae to the adjacent chamber, as shown in the optical micrograph in Figure 4.3c. For feeding the worms and for exposing them to drugs, plastic reservoirs are filled with a suspension of _E. coli_ bacteria in S medium, containing the antibiotic doxycycline.

4.3.1 Experimental set up

The microfluidic setup was integrated in a stereo microscope (SteREO Discovery.V8, Zeiss, Germany) equipped with a camera. A thermal incubator system was designed and manufactured, to set and maintain a fixed temperature on the chip and in the reservoirs that contain the bacteria feeding solutions (Figure 4.3d). The incubator box was made in extruded polystyrene. The top and the bottom of the incubator box featured a transparent PMMA window to allow for microscopy observation of the chip inside. The incubator was fixed to a xy motorized stage (Standa, Lithuania). A schematic of the electronic set up placed inside the polystyrene box is given in Figure 4.4. A temperature sensor (AD22100, Analog Devices, US) was placed in contact with the glass side of the chip for monitoring the temperature of the microfluidic device. The temperature signal was exploited to set the power provided to a Peltier thermoelectric module in a closed-loop configuration, for active control and constant monitoring of the temperature experienced by the worms inside the chip. An Arduino microcontroller board (Arduino UNO, Ivrea, Italy) was used to read the signal from the temperature sensor and set the power to the Peltier thermoelectric module, in a proportional integral derivative (PID) closed-loop configuration. Generally, a PID controller reads the sensor signal and
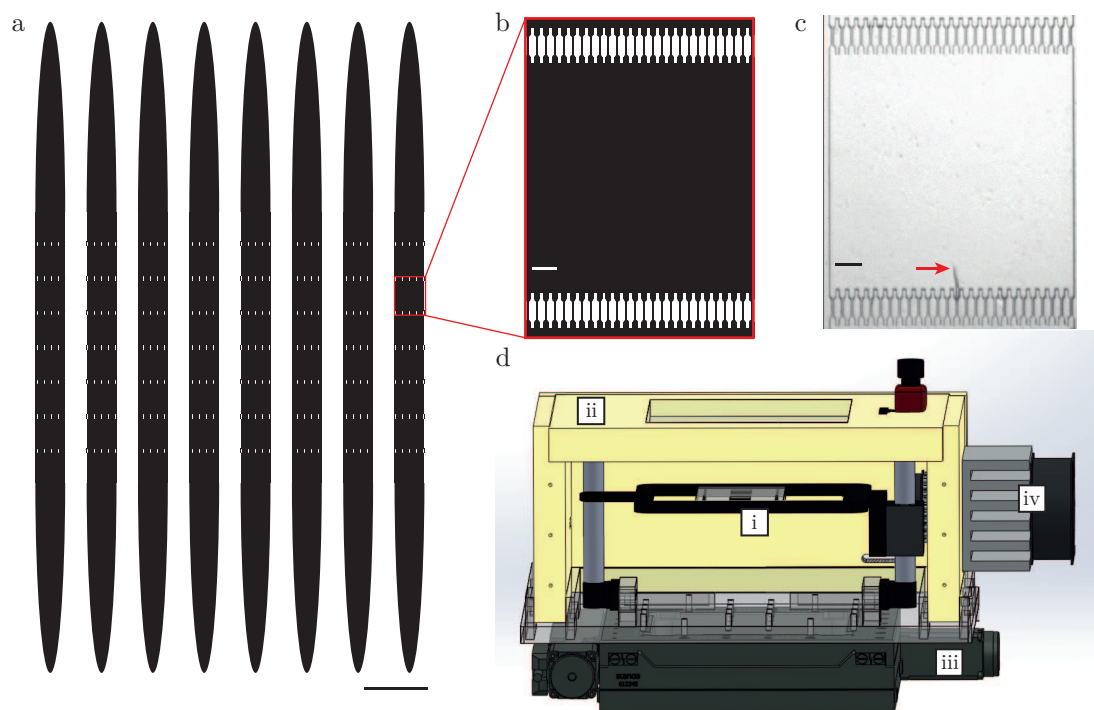
Figure 4.3 – Overview of the microfluidic-based platform for controlled *C. elegans* culture and DoE analysis. a) Schematic of the microfluidic device. The chip consists of 8 channels, each provided with one inlet and one outlet. The channels are independent and up to 8 conditions can therefore be tested at the same temperature in parallel. Each channel is an array of 6 chambers separated by 5 μm-feature filters. Scale bar = 2.5 mm. b) Zoom of a culture chamber, delimited at the entrance and exit by the filters, the size of which is designed in such a way that L1 larvae can pass through only under high flow condition. Scale bar = 200 μm. c) Picture of a single culture chamber containing a L1, whose maximum diameter is larger than the filter size. Scale bar = 200 μm. d) Representative schematic of the inside of the thermal incubator. The microfluidic chip (i) is placed inside the insulating box (ii). The reservoirs, the tubings connecting the chip with the reservoirs and with the microfluidic pumps outside the box are not represented here. The box features a top and bottom polymethylmethacrylate (PMMA) window, and is placed on a motorized xy stage (iii). A thermoelectric module is fixed on the side of the box (iv) and is used to set the temperature that the worms experience inside the microfluidic chip.
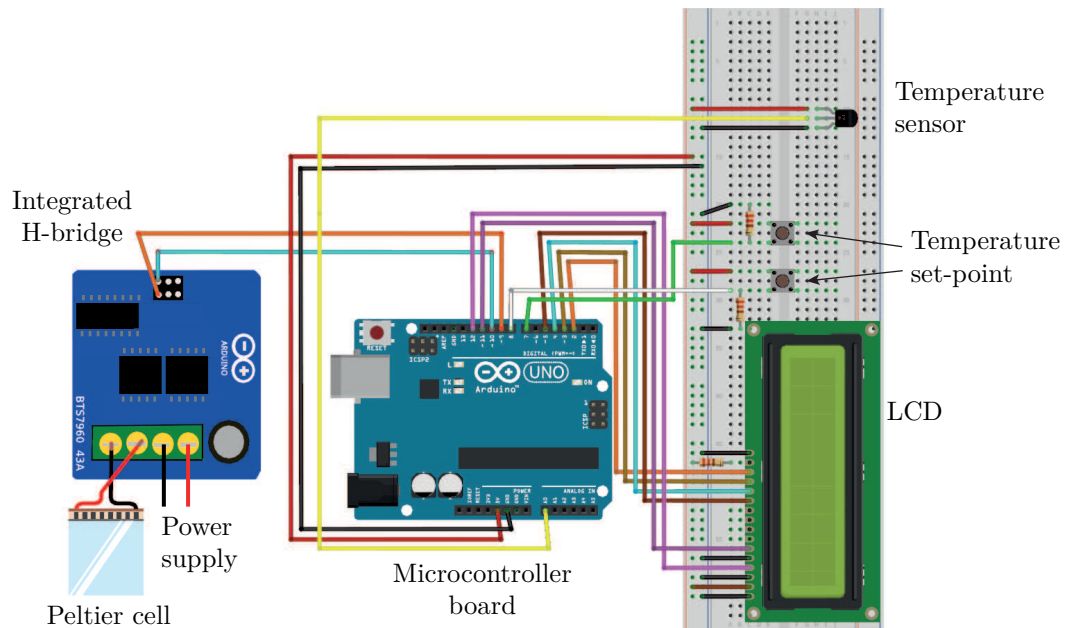
Figure 4.4 – Schematic of the electric circuit designed to control the temperature into the thermal incubator. According to the signal measured by a temperature sensor, a microcontroller sets the power given to an H-bridge connected to a Peltier cell, in a closed-loop proportional integral derivative (PID) configuration. The temperature set-point can be adjusted by the user through two dedicated buttons, and is displayed on a LCD with the actual measured temperature.

computes the desired output by calculating and summing the proportional, integral and derivative responses. The output control signal $u(t)$ can be therefore defined by Equation 4.2:

$$u(t) = K_p e(t) + K_i \int_{t_0}^{t} e(t) \, dt + K_d \frac{de(t)}{dt} \tag{4.2}$$

K_p, K_i and K_d are respectively the gains of the proportional, integral and derivative components. $e(t)$ is the the difference between the set-point value and the output signal. The proportional, integral and derivative gains were tuned using the open-loop step response method by Ziegler and Nichols [87] and were then experimentally optimized. After calculating the three gains, the PID control operations were committed to a dedicated Arduino library. The electric circuit was provided with an integrated H-bridge (BTS 7960B, Infineon technologies, Germany), to change the direction of the current depending on the heating or cooling mode of the Peltier element. The default value of the set-point, 20 °C, could be increased or decreased by 0.5 °C by the user, pressing two dedicated buttons. The temperature set-point and the actual temperature were displayed on a LCD.

The microfluidic operations were controlled using a Kloehn pump (Norgren Kloehn, US) and Micromanager microscopy software. The acquisition system was programmed so that brightfield pictures were taken every 20 min of each chamber.

4.4 Effect of temperature, food amount and drug dose within the chosen experimental range

The larval development was monitored for each *C. elegans* worm in the chamber array, following the experimental protocol described in Section 4.5.1. In all the 13 conditions that I tested, the worms completed their development. All the larval stages (L1, L2, L3 and L4) were observed, as well as the YA stage and adult (A), with the production of progeny in the microfluidic chamber (Figure 4.5). The image stacks generated by combining all images of a given chamber over time were processed in order to measure the duration of the larval development. Completion of the latter was identified by observation of the first progeny production, *i.e.* eggs being laid in the chamber. For each experimental condition, the readout was obtained by averaging the development time of all the investigated animals. The experimental development times can be considered as the components of a vector and are shown in the left column of Table 4.3). From these results, I calculated the coefficients of the quadratic polynomial model in Equation 4.1 (Table 4.4). Afterwards, the components of the theoretical development time were calculated based on the best fit as well, as shown in the right column of Table 4.3.

The interpolated data obtained from the model showed excellent fitting with the experimentally measured values, as shown in Figure 4.6. This confirms that choosing a quadratic model was a correct assumption, as this model accounts for the recorded data.
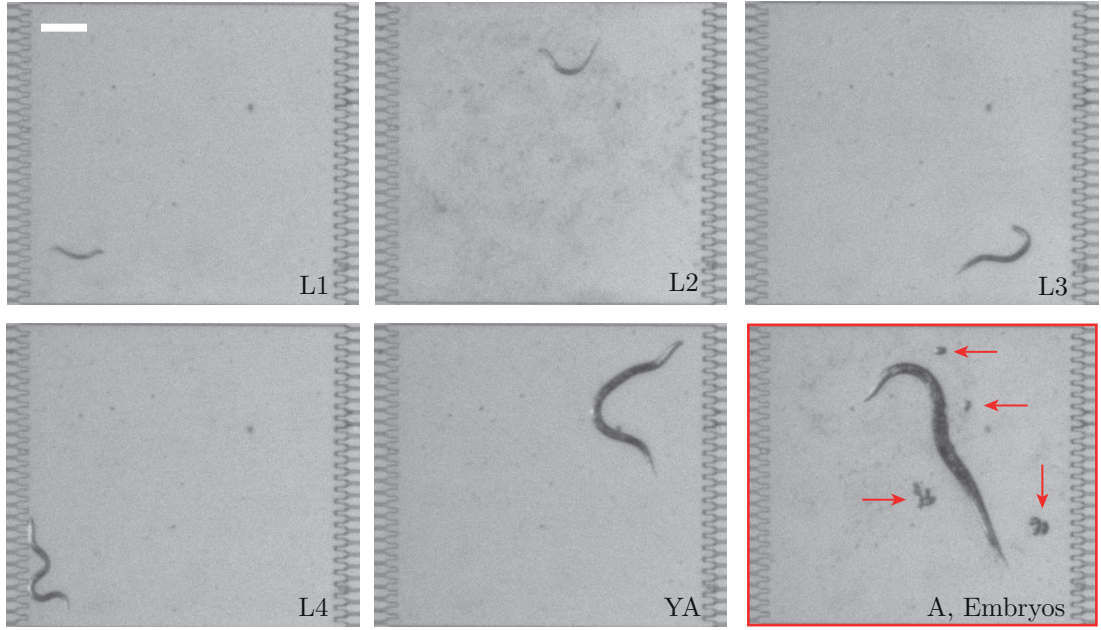
Figure 4.5 – Illustration of the time-lapse brightfield imaging, here shown only for one worm, enabled for each chamber of each chip array during the larval development. The worms completed their development, from the larval stage L1 until adulthood and first progeny production. Scale bar = 300 μm.

	Experimental development time Y [h] average $\pm$ SD (N)	Interpolated values of development time as given by Equation 4.1 [h] $\hat{y}$
1	95.8 $\pm$ 2.8 (11+13+12)	95.8
2	80.9 $\pm$ 2.6 (12)	80
3	89.8 $\pm$ 3.7 (13)	89.2
4	103.3 $\pm$ 2.4 (12)	104.7
5	115 $\pm$ 3.5(14)	115.8
6	109 $\pm$ 2.7 (12)	109.6
7	80.5 $\pm$ 2.2 (14)	79.1
8	92.4 $\pm$ 1.6 (12)	90.9
9	63.5 $\pm$ 3.3 (13)	65.7
10	104.9 $\pm$ 3.4 (14)	106.3
11	66.3 $\pm$ 4.1 (12)	65.4
12	129.3 $\pm$ 4 (13)	127.1
13	110.6 $\pm$ 2.3 (14)	111.4

Table 4.3 – Averaged experimental results (average $\pm$ SD, with the number of animals tested N in brackets) and interpolated values obtained for the different conditions determined by the Doehlert design.

b_0	b_1	b_2	b_3	b_{12}	b_{13}	b_{23}	b_{11}	b_{22}	b_{33}
95.861	-17.8661	-1.451	27.163	0.914	-5.893	8.588	2.097	3.577	-6.789

Table 4.4 – Coefficients of the quadratic polynomial model in Equation 4.1.
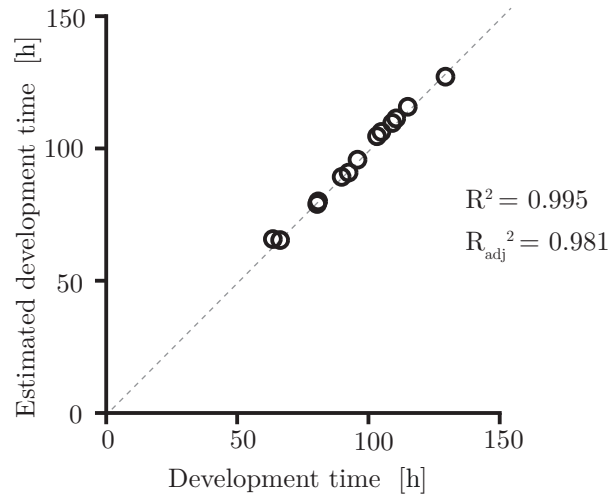
Figure 4.6 – Scatterplot of the experimental data and the results obtained from the quadratc model. The development time obtained from the polynomial model agrees with the experimental results, as also quantified by a correlation coefficient R^2 of 0.995 and a coefficient of determination of R^2_{adj} of 0.981.

4.4. Effect of temperature, food amount and drug dose within the chosen experimental range

	Sum of Square	DoF	Mean Square	F	p-value
X_1	1276.79	1	1276.79	178.56	0.000905
X_2	8.43	1	8.43	1.17	0.356937
X_3	2947.96	1	2947.96	412.27	0.000261
$X_1 X_2$	0.62	1	0.62	0.08	0.786475
$X_1 X_3$	20.81	1	20.81	2.91	0.186533
$X_2 X_3$	44.23	1	44.23	6.18	0.088702
X_1^2	2.93	1	2.93	0.41	0.567483
X_2^2	8.53	1	8.53	1.19	0.354517
X_3^2	32.46	1	32.46	4.53	0.122926
error	21.45	3	7.15	1	0.5

Table 4.5 – Analysis of variance for the experimental development time (DoF: degree of freedom, F: Fisher ratio).

In order to determine the validity of the quadratic polynomial model in relation to the experimental data, the Analysis of Variance (ANOVA) was performed, too. The results are presented in Table 4.5. The analysis of the Sum of Squares (SS) and the Mean Square (MS) values, both giving information about the total variance of the observation, revealed that X_1 and X_3, respectively temperature and doxycycline concentration, had an effect on the larval development time, as their SS and MS are more than 100 times larger than the SS and MS of the error. A more detailed description of the ANOVA terms is given in Subsection 4.5.4.

 These considerations are also supported by the analysis of the p-values. In fact, high significance was observed for X_1 and X_3. Interestingly, the second order interactions between the factors did not have a significant effect on the larval development time. The overall p-value of the model, computed as 0.00258, confirmed the high accuracy of the quadratic polynomial model, as confirmed by the coefficient of determination R_{adj}^2.

The results obtained for the 13 tested conditions were then compared by grouping them according to the doxycycline dose used and in an increasing temperature-wise order (Figure 4.7). Moreover, in order to appreciate the effect of the 3 factors on the worm development in a more comprehensive fashion, the response was color-coded and represented in the experimental space by interpolating the different experimental conditions from Equation 4.1 (Figure 4.7d). This representation enables to determine the interpolated development time that would be obtained if different values for the 3 factors would have been taken, beside the chosen 13 in Table 4.1, therefore allowing predicting the process behavior within the full investigated experimental domain.

The shortest development time was obtained when worms were treated with the lowest dose of doxycycline and at high temperature (Figure 4.7a and dark blue area in Figure 4.7d). By comparing the development time in Figure 4.7a, b and c, a progressively dramatic increase in the development time can be observed in correspondence of increasing amount of doxycycline. In particular, the longest development time was obtained upon treatment with the highest doxycycline dose and at the lowest temperature (Figure 4.7c

and yellow area in Figure 4.7d). In contrast to the roles of temperature and doxycycline, the developmental delay is not feeding-dependent for the used concentrations of bacteria. Similarly, in the color-coded representation of development time in Figure 4.7d, points corresponding to the same development time are described by different coordinates along the [*E. coli*] axis, confirming that food amount does not alter the duration of the development. Moreover, for a few experimental runs, development times showing no significant difference (p-value > 0.05, see Table 4.6) were obtained. This occurred when in pairs of independent experiments (run 6-run 10, run 8-run 3) worms were exposed to the same amount of doxycycline, the same temperature and double *E. coli* concentrations, confirming that feeding - in the considered range of bacterial contentrations – does not play a significant role. Moreover, development times not statistically different were obtained also when worms were treated either with a low doxycycline dose at a low temperature level or with higher doxycycline dose at a higher temperature (run 7-run 2, run 6-run 13, run 10-run 4). This finding suggests that the effect of the high temperature can counterbalance the impact of a strong antibiotic concentration.

These findings were supported by the isosurface-response representation shown in Figure 4.8, where experimental points corresponding to the same larval development time lay on the same surface. Interestingly, this representation allows finding all the possible combinations of temperature, *E. coli* concentration and doxycycline concentration that must be used to achieve a desired effect on the larval development time.

4.5   Materials and methods

4.5.1   Microfluidic experimental protocol

Initially, after sterilization by injection of ethanol 70%, the microfluidic chip was filled with S medium. L1 worms were harvested from the culture plate and suspended in S medium. Afterwards, they were injected into each channel from the corresponding inlet and distributed along the array by applying 1 s flow pulses of 2 μL inflow, to let the PDMS filters expand and the L1 pass through, as described in [78]. A uniform distribution of the larvae over the array was consistently obtained, confining worms in separate chambers along each microfluidic line. Doing so, overcrowding was prevented and a proper worm growth was ensured. Typically, 1 to 3 worms get confined in each chamber, with about 15% of empty chambers and about 65% of the chambers containing 1 isolated worm. Each channel was then perfused with a flow of *E. coli* bacteria suspended in S medium, containing also the antibiotic doxycycline. The feeding protocol consisted of injecting 8 μL of bacterial solution at a flow rate of 100 nL/s, every 30 min. Depending on the temperature condition, different concentrations of *E. coli* and doxycycline were used, according to the combinations listed in Table 4.1. For example, the runs 3, 4, 8 and 9 were performed simultaneously, at a set temperature of 22.5 °C.
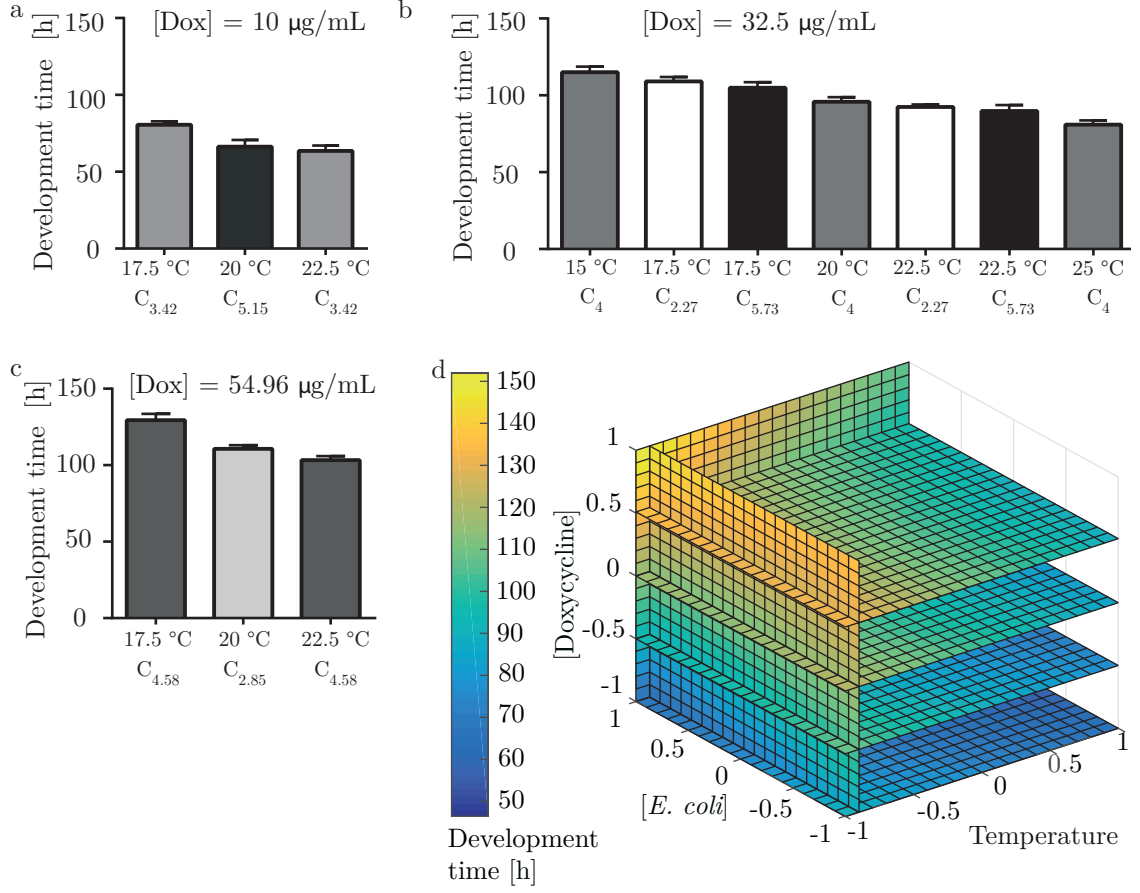
Figure 4.7 – Effect of temperature, *E. coli* concentration and doxycycline dose on the development time, in the range considered by our DoE experiments. Effect of temperature on the development time with doxycycline concentration of a) 10 µg/mL, b) 32.5 µg/mL and c) 54.96 µg/mL. C_n indicates the bacterial concentration (n $\times$ 10^9 cell/mL). Bars are expressed as average $\pm$ SD. d) Color-coded representation of the interpolated development time values Y. The vertical plane corresponding to X_1=-0.9 was arbitrarily chosen for approppriate visualization of the response at low-temperature conditions.
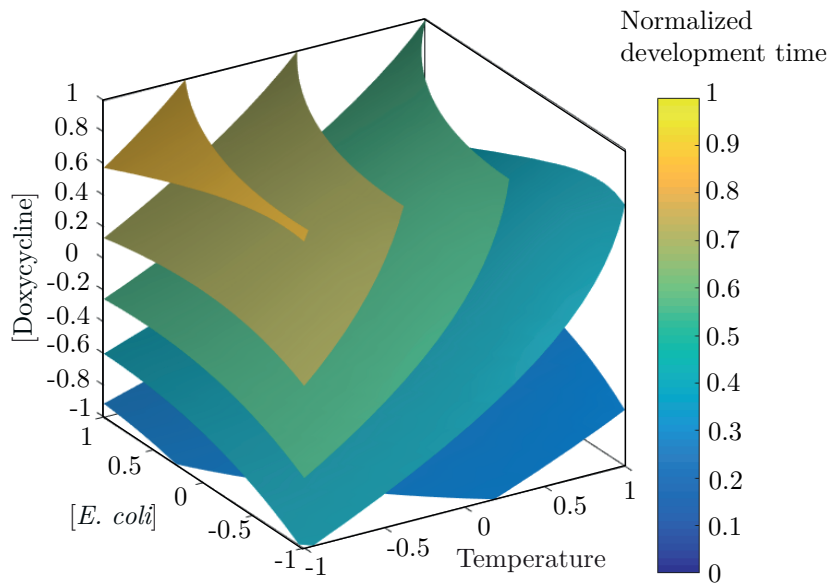
Figure 4.8 – Iso-surfaces representation of the normalized interpolated larval development time as a function of temperature, *E. coli* concentration and doxycycline concentration. The response is re-scaled between 0 and 1, so that these values represent the minimum and maximum development duration respectively. The factors are considered in their coded values (see Table 4.1).

4.5.2 *C. elegans* experimental model and subject detail

C. elegans strain was cultured at 20 °C on NGM 90 mm Petri dishes seeded with *E. coli* strain OP50. The strain used in this study was the N2, provided by the Caenorhabditis Genetics Center (University of Minnesota). Before starting the experiments, the plates were washed with S medium and L1 were harvested.

4.5.3 *E. coli* culture

HT115 *E. coli* bacteria were grown in LB with 100 μg/mL ampicillin and 12.5 μg/mL tetracycline overnight in a thermal shaker at 37 °C. The following day, 50 μL of the confluent bacterial cultures were used to inoculate freshly prepared LB medium containing only ampicillin. The new cultures were grown until reaching an optical density between 0.6 and 0.8, and 90 μL were used for seeding the experimental plates. After the overnight culture, 50 mL of the bacterial cultures were centrifuged to remove LB; in this way, bacteria samples with the desired optical density were obtained by adding S medium accordingly. The concentration of each bacterial solution was measured using a commercial spectrophotometer (WPA CO8000, Biochrom, UK).
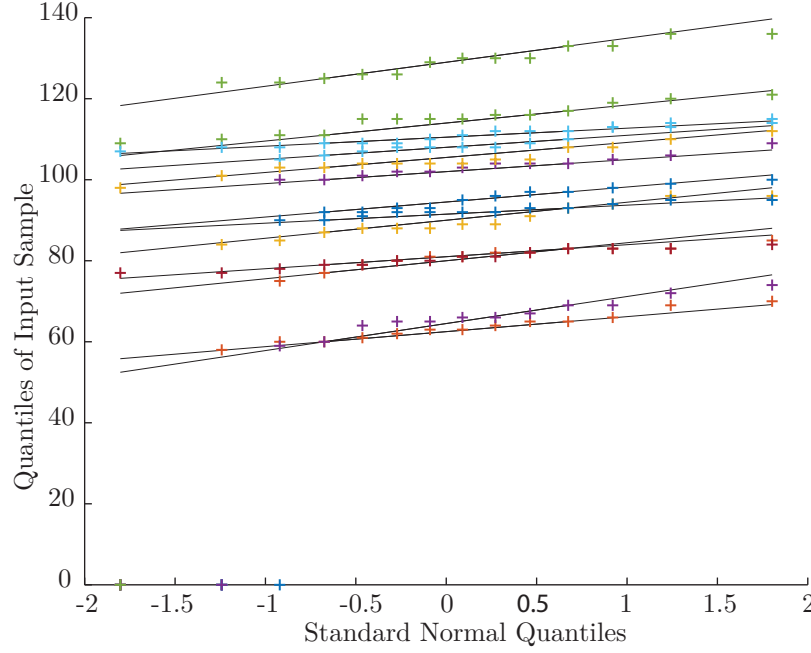
Figure 4.9 – Quantile-quantile plot of the quantiles of the sample data (*i.e.* DoE 13 experimental runs) versus normal distribution of the sample. The theoretical quantiles values from a normal distribution. The approximately straight lines indicate that the distribution of our sample is normal.

4.5.4 Quantification and statistical analysis

The validity of the quadratic polynomial model in relation to the experimental data was assessed upon the ANOVA, performed using a built-in Matlab function. The average value of each of the 13 conditions was used. The normality of the data distribution in each dataset was assessed by using the Matlab built-in function to display the quantiles of the sample and the theoretical quantiles from a normal distribution in a quantile-quantile plot (see Figure 4.9). For each experimental run, the dataset was obtained from worms uniformly distributed along 2 channels of the same chip. The sample number N indicates the number of independent biological samples for each experimental run. Statistical significance was determined with a 2-way ANOVA with Tukey correction for multiple comparisons using GraphPad Prism.

ANOVA is used to determine the validity of the model in relation to experimental data. The coefficients of the model are related to the factors targeted by the set of experiments and are then varied during the experiments. The residue is due to unidentified factors that are not controlled and thus have changed during the experiments.

For each factor, the total variance of the observations is given by the total *SS*, which is the sum of squares of the deviations of all the observation y_i from their mean y_m. *SS*

	1	2	3	4	5	6	7	8	9	10	11	12	13
1	-	**	**	**	**	**	**	0.4644	**	**	**	**	**
2		-	**	**	**	**	0.999	**	**	**	**	**	**
3			-	**	**	**	**	0.7438	**	**	**	**	**
4				-	**	**	**	**	**	0.9893	**	**	**
5					-	**	**	**	**	**	**	**	*
6						-	**	**	**	0.0682	**	**	0.9912
7							-	**	**	**	**	**	**
8								-	**	**	**	**	**
9									-	**	0.6262	**	**
10										-	**	**	**
11											-	**	**
12												-	**
13													-

Table 4.6 – Adjusted *p*-values from 2-way ANOVA test with Tukey correction for multiple comparisons. *p*-values were graphically reported as * $p \leq 0.05$, ** $p \leq 0.01$.

can therefore be quantified as in Equation 4.3

$$SS = \sum_{i=1}^{n}(y_i - y_m)^2. \tag{4.3}$$

The Degree of Freedom (*DoF*) represents for each factor the number of values (or levels) that are free to vary in one experiment. Having chosen here a Doehlert design of experiment, each factor assumes a precise value in each experiment. Therefore, the number of DoF for each factor is 1.

MS, gives information about the total variance of the observations taking into account the DoF. It is therefore defined as $MS = SS/DoF$.

For each factor, the Fisher ratio (*F*) is the ratio between the *MS* and the *MS* of the error, or residue. The *p*-value is the probability to obtain a given *F* by chance. The smaller the *p*-value, the higher is the significance of the considered factor. The standard criteria for accepting a factor as significant is typically $p < 0.05$.

The *p*-values, adjusted according to Tukey correction, are displayed in Table 4.6.

4.6   Discussion and conclusion

In this study, I used a DoE approach to characterize the effect of temperature, concentration of *E. coli* and dose of doxycycline antibiotic on the duration of the larval development of the nematode *C. elegans*. In particular, a Doehlert design was chosen to characterize the effect of those 3 factors on the worm development. A microfluidic chip enclosed in a custom-made thermal incubator, was designed to culture *C. elegans* larvae with full control of the experimental parameters.

Our results confirmed the severe dose-dependent effect of doxycycline on the duration of the larval development, making the concentration of doxycycline the major player (p-value = 0.000261). Indeed, worms treated with the highest doxycycline dose (54.96 μg/mL) took about 65% more time to develop, compared to worms treated with the lowest dose (10 μg/mL) at the same temperature. A milder but highly-significant effect (p-value = 0.000905) on the larval development was induced by temperature. In fact, worms cultured at 15 °C took 42% more time to develop than the ones cultured at 25 °C and treated with the same doxycycline dose.

On the other hand, the food concentration did not affect the larval development time. This finding allows us to conclude that *E. coli* concentrations in the range 2-6 $\times$ 10^9 cell/mL can be alternatively safely used in microfluidic culture protocols, without significantly affecting the development time. This range could be considered as appropriate feeding range for microfluidic cultures, as it prevented either underfeeding or bacterial gut invasion.

The DoE approach has established a mathematical relationship between the larval development time and culture temperature, food concentration and drug dose, requiring only 13 well-designed experiments to characterize the effectiveness of the drug, as well as the influence of all the considered experimental factors on the treatment outcome. When performing the experiments, 3, 5 or 7 different levels (values) were varied of each factor over the 13 experiments (see Table 4.1). On the other hand, according to the standard one-factor-at-a-time approach, where only one factor is changed and the outcome is not interpolated over the full breadth of the experimental space, to explore the full combinations of three factors, each assuming 3, 5 and 7 levels (Table 4.1), 105 (3×5×7) experiments would have been necessary. At the same "experimental" cost (13 experiments), the standard approach would have allowed only about 2 levels for each factor, providing therefore very limited information on the control of the development time. Practically, as the fitted polynomial then allows for the interpolation of any point in the considered experimental range with a very limited error, this allows for the continuous exploration of the experimental setting, and the identification of a possible ideal operation point.

The analysis showed that there are only limited interactions between the different factors. It is worth to notice, however, that the ANOVA showed a p-value of 0.088 for the interaction between food amount and doxycycline dose. This p-value is too high to indicate a relevant impact, but is the third lowest recorded in the analysis. This may hint that there may be some interactions beyond the boundaries of the experimental space that I considered here. Indeed, a higher dose of doxycycline, which is an antibiotic, might damage or kill the bacteria and make them less nutritious for the worms, possibly affecting their life-cycle. This fine contribution would have been impossible to observe with a standard experimental approach, thus highlighting the relevance of the DoE and the quadratic fitting.

Moreover, such a DoE approach allowed predicting the process behavior in the experimental space, by revealing the drug effect even upon additional combinations of experimental

factors, not limiting the study to the 13 tested conditions. The use of a DoE approach would therefore tremendously increase the efficiency of a drug screening process, by minimizing the use of the resources – and therefore costs – while maximizing the knowledge of the process.

In this endeavor, the use of microfluidic platforms represents a crucial step towards the standardization and the optimization of the drug testing protocols based on the use of small model organisms such as *C. elegans*. Thanks to our microfluidic platform, I automatized the *C. elegans* culture and delivered the drug doxycycline in a precise spatio-temporal way. Moreover, our microfluidic device enabled reducing the overall drug testing time, by parallelizing the experiments. In fact, not only multiple animals were simultaneously exposed to the same compound, but also multiple conditions were tested in parallel within independent channels of the same device.

4.7   Future outlook

Continuous longitudinal monitoring throughout the entire larval development was performed and other phenotypes of interest could be extracted in future via image processing. Such a systematic drug dose test, following the principles of a DoE approach, would have high added value to predict the optimal conditions to eventually use in follow-up targeted drug experiments. A factorization approach will be instrumental in ensuring the drug effectiveness and disentangle its effect from any undesired effects of other possible contributors.

In order to deepen the understanding of the drug effect on *C. elegans*, other phenotypic read-outs could be considered besides the development time. In fact, by using the same microscopy set up and the same microfluidic device, one could also measure the effect of doxycycline on the worms size or on the fluorescent expression of a gene of interest, similarly to what I described in Chapter 3.

5 Monitoring bacterial concentrations in micro-chambers by optical absorbance measurements

Abstract Envisioning a microfluidic platform where *C. elegans* feeding is fully controlled and food consumption is quantified as additional phenotype, in this Chapter I describe a method to measure the absorbance of solutions of planktonic *E. coli* bacteria in a microfluidic chip. The latter consists of two independent micro-chambers, one used to measure the concentration of the bacterial solution, the other used for a reference measurement. Each chamber is placed in between a light emitting diode and a photodiode, to simultaneously measure the light transmittance across each chamber, from which the absorbance of the bacterial solution is calculated by applying Lambert-Beer's law. I calibrated the device and obtained a linear relation between the absorbance and the concentration of the injected solutions. Afterwards, to assess the turbidity of the solution on the long-term, the on-chip absorbance was monitored over 10 h in absence of flow: the absorbance dropped after 1 h, revealing that the solution became more optically-transparent than expected, and this in a concentration-dependent fashion. These results can be understood by the phenomena of bacterial settling and aggregation, which were further investigated by video microscopy. I hypothesized a simple mathematical model for the over-time change of absorbance, according to which, bacterial settling and aggregation were shown to affect absorbance measurements of the solutions.

This chapter is an adapted version of the following publications:

- **M. C. Letizia**, P. G. Testa and M. A. M. Gijs, "Monitoring bacterial concentrations in micro-chambers by optical absorbance measurements", Manuscript in preparation.
- **M. C. Letizia**, P. G. Testa and M. A. M. Gijs, "Bacterial feeding control system for on-chip culture of the nematode *Caenorhabditis elegans*". Proc. of 21th International Conference on Miniaturized Systems for Chemistry and Life Sciences (microTAS 2017), Savannah, Georgia, US, 2017.
  Poster presentation.

- **M. C. Letizia** and M. A. M. Gijs, "Accurate quantification of bacteria concentration as a nutrient for *C. elegans* worm culture on chip", 19th Edition of Nano Bio Tech, Montreux, Switzerland, 2015.
  Oral and **poster** presentation

5.1 Introduction

Bacteria are of great interest in the fields of medicine, microbiology, and ecology. A major reason for their success in nature is that they multiply at extraordinary rates when food is available, and can switch easily from a mobile planktonic state to a colonial biofilm state for optimum species survival. Bacteria were not only used as a model organism to investigate phenomena involved in surface colonization and biofilm formation [88], [89], but also several behaviours related to their planktonic state were investigated [90]–[93]. In this frame, diverse aspects of microbial insight received interest, such as the effect of bacterial motion on mixing or transport of particles [94], the effect of flow on nutrient uptake and encounter rate of bacteria [95], [96], or their interaction with boundaries and surfaces [97]–[99]. The ways bacterial cells interact with each other via chemical signalling pathways, such as quorum sensing or virus-host interaction, were investigated too [100]. The bacterial resistance to antimicrobial compounds is being of great interest as well, as it increasingly affects both human and wildlife populations [101], [102]. Indeed, in applications such as waste-water treatment, medicine, seawater desalinization or production of biofuels, the quantification of the amount of planktonic microbes in the region of interest is of crucial importance [103]. In fact, the majority of the experimental outcomes depends crucially on the bacterial amount/concentration, which is therefore a very important parameter that should always be determined.

Microfluidics facilitated research about bacterial cultures [103]. Microfluidic chips usually are optically transparent, therefore enabling direct and quantitative observation of the bacteria behaviour via microscopy. Environmental cues can be mimicked in microfluidic chips, where chemo- and thermo-gradients can be generated in an accurate and flexible way [104]. Controlled flows and shear rates can be advantageously applied to bacteria to assess the effect of flow on their behaviour [105], [106]. Microfluidics was also used to study surface interactions, by dedicated chip areal micro-patterning and by tuning of the hydrodynamic parameters [107]–[109]. Interestingly, many papers reported attempts to monitor the growth of bacterial colonies and quantify their concentration [103]. In particular, bacteria and yeast cells were cultured in precise chemostatic and thermostatic conditions; the growth of the colony was monitored over time, by taking fluorescent pictures, from which the bacterial number was assessed as ratio between total fluorescent area and the background [110]. Others fabricated a microfluidic bioreactor for long-term culture of *E. coli* bacteria and monitored the colony growth by processing brightfield images and counting the number of isolated bacteria in the micro-chamber [111]. Similarly, the bacterial growth was monitored in a microfluidic chip by real-time counting the number of bacteria in a known volume at regular time intervals by brightfield microscopy [112]. Considered this state of the art about microfluidic bioreactors, the quantification of planktonic bacterial concentration and growth in a microfluidic chip is currently mostly based on bacterial counting – manual or automated – starting from fluorescence or brightfield pictures. This is indeed accurate, but presents many drawbacks: first, especially when performed manually, bacteria counting is time-consuming and error-

prone, and cannot be executed in a continuous and real-time fashion; second, such a quantification requires complex equipment dedicated to optical and fluorescent microscopy. For applications focused on cell detection rather than bacterial culture, more sophisticated and automated approaches for cell counting have been developed [113]–[116]. These studies rely on the Coulter principle and exploit the non-conductivity of bacterial cells: a bacterium passing through an aperture, concurrent with an electric current, produces an impedance change proportional to its size. Dedicated microfluidic chips were therefore designed, all featuring a small sensing channel or a constriction allowing the passage of a single cell. This technology allowed detecting single bacteria in an automated way, even when high flow rates were applied. However, these microfluidic devices do not represent the best solution for long-term experiments, as the continuous flow of bacteria through an aperture of a few μm might lead to the formation of biofilms and eventually chip clogging [117].

A significant improvement in the state of the art was shown by Jakiela *et al.* [118]. They exploited droplet microfluidics principles to compartmentalize bacterial cells and nutrient in microdroplets, creating in this way many parallel chemostats. The growth of the colony was monitored by periodically measuring its absorbance in a 5 mm-thick on-chip optical path, using an external commercial spectrophotometer coupled with a waveguide. However, this approach required a relatively-complex fluidic design and the use of multiple valves. Moreover, such droplet-based measurements are not representative of the dynamic behavior of bacteria in a three-dimensional and gas-permeable micro-chamber. Jung *et al.* [119] monitored the growth of bacteria microcolonies spotted on a container eventually sealed with a CMOS chip for direct real-time observation. Such a system, however, is limited by the recommended cellular density in the 10-100 cell/cm^2 range and, similarly to the previous example, prevents gas and media exchange. Interestingly, Meyer *et al.* developed a bench microfluidic reactor to probe the role of quorum sensing in the formation of biofilms by measuring their optical absorbance [120]. To this purpose, a simple straight microfluidic channel was fabricated and inoculated with *E. coli* bacteria. An array of light emitting diode (LED) illuminated the channel and the absorbance was measured in two different points of the channel, each provided with a photodiode (PD). Similarly, Kim et al. monitored biofilms using LEDs and a charge-coupled device camera, upon treatment with antibiotic and electric current [121]. This approach resembled the measurement of the optical density (OD) performed by commercial spectrophotometers. However, unlike spectrophotometers, the absorbance signal that was measured was not compared to a reference signal provided by a transparent solution, which is a prerequisite for accurate and noise-free absorbance and optical density measurements.

In this Chapter, I present a method to measure the optical absorbance of solutions of planktonic *E. coli* bacteria. I designed an opto-electronic device that was integrated and optically aligned to a microfluidic chip, as sketched in Figure 5.1. The latter consists of two identical independent micro-chambers, one used to measure the concentration of the bacterial solution, the other used for a reference measurement. Each chamber has a volume of 7.2 μL and functionally replaces a 1 mL cuvette, as traditionally used in most

Figure 5.1 – Schematic of the quantification of bacterial concentration in a microfluidic chamber.

of the commercial spectrophotometers, thereby considerably reducing the required sample volume. Each chamber was placed in between a LED and a PD, conveniently designed to simultaneously measure the light transmittance across each chamber, from which the absorbance of a bacterial solution was calculated according to the Lambert-Beer's law. The device was tested and calibrated with different bacterial solutions of known concentration, obtaining a linear relation between the absorbance and the concentration of the injected solutions. Afterwards, I measured the on-chip absorbance over 10 h in absence of flow, to assess the turbidity of the solution on the long-term. I found that the measured absorbance consistently dropped after 1 h of measure, revealing that the bacterial solution became more optically-transparent than expected, in a concentration-dependent fashion. In order to explain this finding, the phenomena of bacterial settling and aggregation were investigated with further experiments. Based on our observations, I hypothesized a simple mathematical model for the change of absorbance over time, according to which, bacterial settling and aggregation phenomena were shown to affect absorbance measurements of planktonic solutions over time.

5.2 Double-beam absorbance measurement setup

The on-chip absorbance A of a planktonic bacteria solution was obtained applying the Lambert-Beer's absorption principles, according to which

$$A = log_{10}\frac{I_0}{I} = k_\lambda CL. \tag{5.1}$$

I_0 is the intensity of a light beam that illuminates a liquid sample, I is the intensity of the light transmitted through the sample. k_λ $[M^{-1}cm^{-1}]$ is the molar extinction coefficient of the sample, which depends on the wavelength of the incident light and the sum of the extinction coefficient due to scattering, k_λ^{scatt}, and the extinction coefficient due to absorbance by the sample, k_λ^{abs}. Both scattering and absorption result in a diminished

I. C [M] or [cell/mL] is the concentration of the bacterial solution, while L [cm] is the length of the optical path of the sample, *i.e.* the thickness of the microfluidic chamber containing bacteria.

A microfluidic chip featuring two identical and independent micro-chambers (Figure 5.2a) was designed in PDMS and glass, following the fabrication steps described in Section 5.5.1. The measurement chamber is filled with a bacterial solution whose concentration has to be measured, while the other chamber is filled with S medium ($C = 0$ cell/mL, optically transparent) for reference. The microfluidic chip was fabricated from a 1 mm-thick PDMS layer, and a microscope glass slide. Each device has a 60 μm-thick inlet and outlet channel, and a round chamber (4 mm in diameter) with 575 μm thickness (see magnification in Figure 5.2a). The sample volume that fills each chamber is scaled down to 7.2 μL, enough to ensure the necessary sensitivity for optical detection. The light absorbance in both chambers was measured by identical pairs of LEDs and PDs (Figure 5.2b). Each PD was inserted in an opaque cylindrical cavity to reduce cross-talks between each LED-PD pair. One extremity of the cylindrical cavity was glued to a magnetic ring and another magnetic ring was fixed to each LED. LED and PD were then magnetically fixed to each other, with the micro-chamber in between. A schematic of the electronic circuit is given in Figure 5.2c. Red LEDs ($\lambda = 630$ nm) (UR502DC, Chengguangxing, China) were chosen as excitation source, motivated by their use in commercially-available spectrophotometers, which measure the OD at 600 nm (OD600), and because high absorption was expected at this wavelength [122]. In order to detect the transmitted light, PDs with an excellent spectral sensitivity of 0.45 A/W at 630 nm were chosen (S10784, Hamamatsu, Japan). Moreover, their sensitive area had a diameter of 3 mm, matching the microfluidic chamber size, and the compact packaging favored the integration of the PD in the microfluidic set up. The two LEDs were powered by a microcontroller (Arduino, Ivrea, Italy) digital output port (5V) and were connected in series with a low-pass RC filter, to reduce any difference in their electrical behaviour and to stabilize the LED emission. A potentiometer was used to finely adjust the intensity of the LEDs' emission, not to damage the downstream PDs. The photocurrent generated by each PD – in the nA order – was amplified and converted to a voltage by a trans-impedance amplifier board (Multiboard, SGlux, Germany). The voltage signals from the measurement and reference channels were processed by an external 16-bit analog-to-digital converter (ADC) (ADS115, Adafruit, US), which provided a resolution of 0.125 mV and supported the I2C serial interface protocol to communicate with the microcontroller. A sampling frequency of 1 Hz was chosen for the microcontroller, as it allowed detecting subtle changes in the concentration of the investigated bacterial solution. A digital 2nd-order Butterworth low pass filter (LPF) with cut-off frequency of 0.05 Hz was first designed in Matlab (Mathworks, US) and then implemented on the microcontroller, to remove signal spikes that were present at higher frequencies.
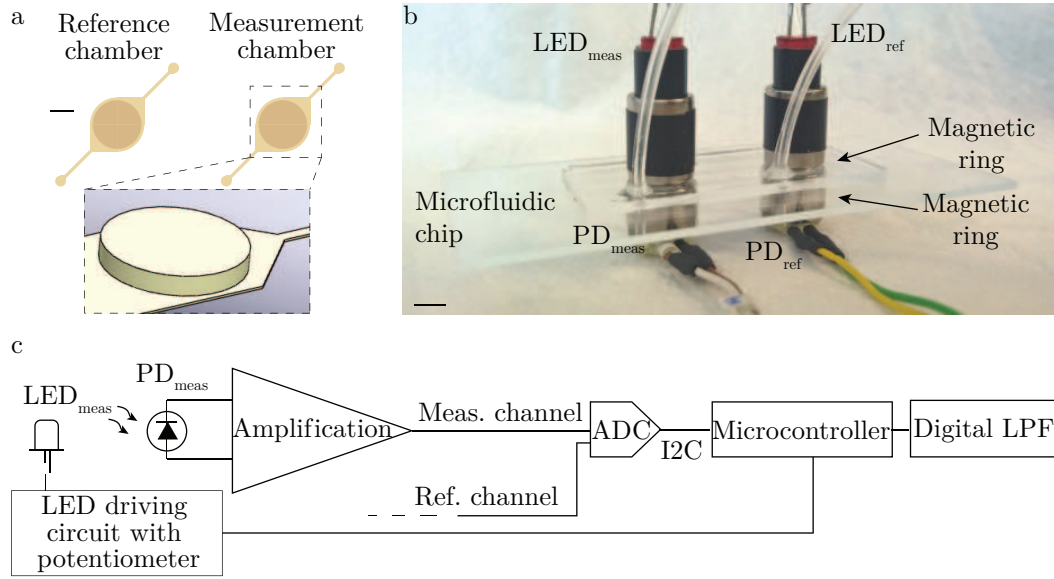
Figure 5.2 – Overview of the miniaturized optoelectronic device. a) Design of the microfluidic PDMS-glass chip featuring two independent micro-chambers. The measurement chamber is filled with the bacterial solution with unknown concentration, while the other chamber is filled with an optically transparent liquid, S medium, and it is used for reference. Scale bar = 2 mm. b) Assembly of microfluidic chip and sensing elements. Two LED-PD pairs, one to measure the absorbance, the other for reference, are aligned and fixed to each other by magnetic rings, holding the micro-chamber in between. Scale bar = 5 mm. c) Schematic of the optoelectronic setup. Two red LEDs illuminate the reference and the measurement chambers, and the transmitted light is detected by the corresponding PD. The read-out signal, inversely proportional to the concentration, is amplified, digitally converted, sampled and filtered by a microcontroller.

5.3 Validation and testing of the setup

The absorbance calculation (Equation 5.1) was readapted as

$$A = log_{10} \frac{V_{ref} - V_{ref}^0}{V_{meas} - V_{meas}^0}, \tag{5.2}$$

where V_{ref} and V_{meas} indicate the ADC read-out values from the reference and measurement channels, respectively; V_{ref}^0 and V_{meas}^0 indicate the corresponding voltage values in absence of light. The subtraction of V_{ref}^0 and V_{meas}^0 was necessary to refer the two detectors read-out to the same baseline in dark condition and to cancel any read-out difference due to the photodiode dark current or to the environment light. Afterwards, the two chambers were filled with S medium and the respective ADC read-out were compared, to check and correct for discrepancies due to possible misalignment of PDs, LEDs and the detection chambers. Then, five bacterial solutions of known concentration (1, 2, 3, 4, 5×10^9 cell/mL, later referred as C_1, C_2, C_3, C_4 and C_5, respectively) were prepared and consecutively injected into the measurement micro-chamber starting from C_1. The reference chamber was filled with S medium for all the duration of the experiment. The ADC read-out related to the measurement and the reference chambers are shown in Figure 5.3a. Due to the compliance and deformability of the PDMS chamber upon injection, the overpressure increased the chamber height and the following relaxation decreased it, resulting in a like-wise change of the optical path with consequent peak artefacts in the signal. To disentangle such artefact from the measurement, the flow was stopped for 1 min after the chamber was filled with the bacterial solution. The absorbance values were computed in 40 s time windows (yellow bars in Figure 5.3a) in which the signal was stable, and the averaged values are reported in Figure 5.3b. A calibration curve was also obtained upon repeated measurements (Figure 5.3c). Our optoelectronic device shows very good linearity (linear correlation coefficient $R = 0.9976$) and the calibration curve has the equation $A=0.0170C$, where A is the absorbance and C the *E. coli* concentration.

5.4 Time dependence of absorption

I typically measure the absorbance of a bacterial solution over a time interval of 10 h. Solutions with concentration C_2, C_3 and C_4 were used in three different experiments. Upon injection, the flow was stopped and inlet and outlet were clamped. Results are given in Figure 5.4. The initial value measured at t = 0 h agrees with the absorbance values previously obtained (Figure 5.3b,c). However, the measured absorbance decreased during a period of 1-2 h after the injection. The amplitude of such a drop seemed to be concentration-dependent, the strongest decrease being observed for the C_4 solution, whose absorbance value became 0.05 - correspondent to a C_3 solution – after 2 h. After this time-window, the measured absorbance underwent a slight linear increase, the amplitude
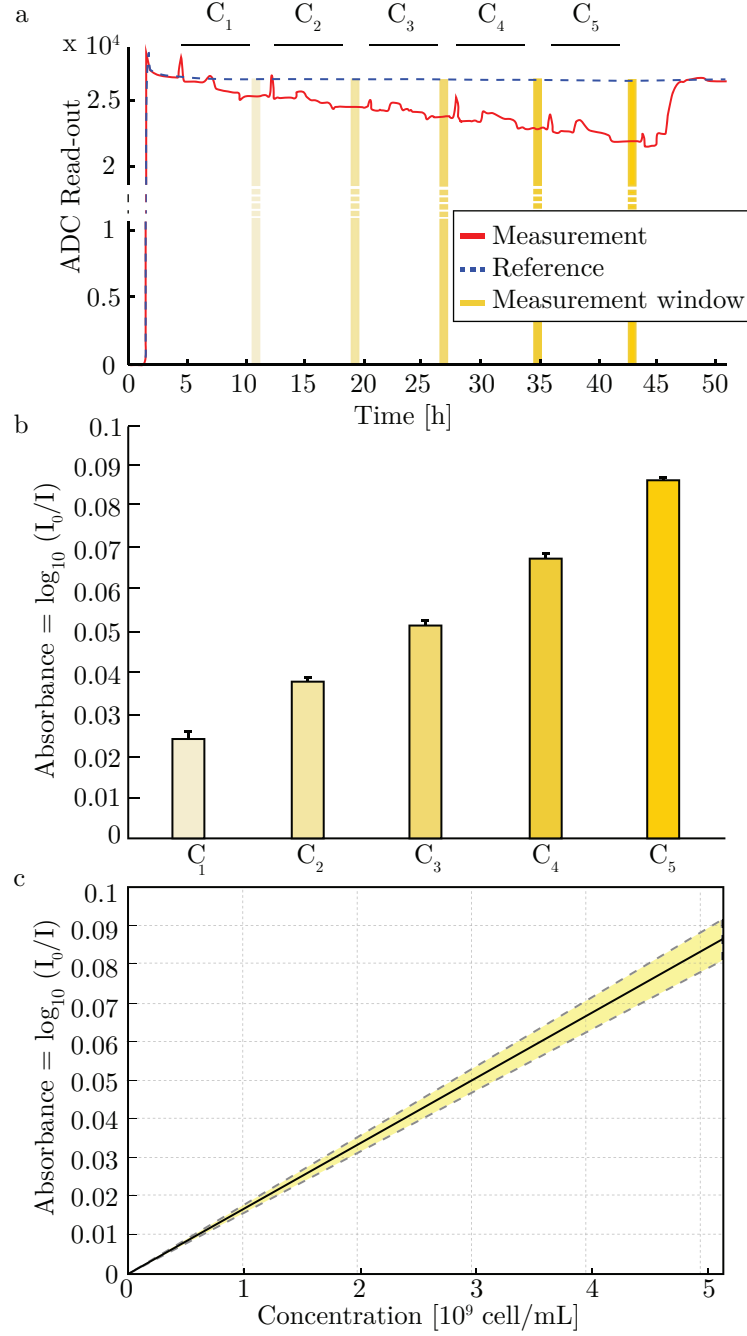
Figure 5.3 – Testing of the absorbance-measurement setup and calibration curve. a) Real-time change of the measured optical signal related to the reference channel filled with S medium (dashed blue line) and the measurement channel (red line) when S medium and then 5 bacterial solutions with increasing concentration – C_1, C_2, C_3, C_4 and C_5 – are consecutively injected. Yellow bars indicate the measuring 40 s-windows for each injected solution. b) Absorbance values for the bacterial solutions measured by our opto-electronic platform. Bars are expressed as average $\pm$ SD. c) Calibration curve of our absorbance-measurement setup, showing a linear relation between the absorbance and the concentration of the injected solutions. The curve is expressed as mean (solid line) $\pm$ SD (dashed line) and is obtained from 4 experiments performed in different microfluidic chips using freshly-prepared bacterial solutions.
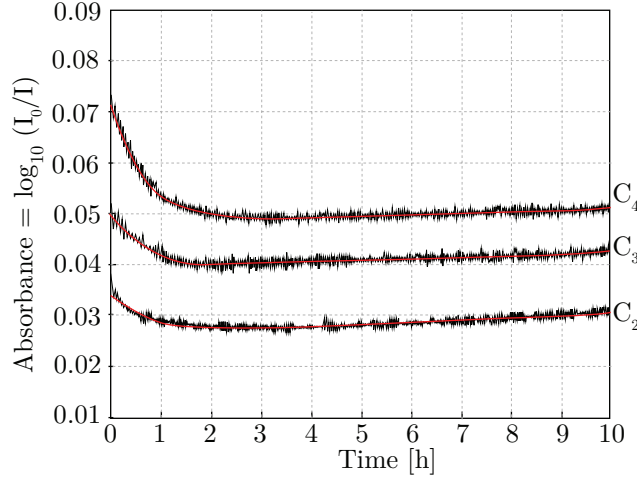
Figure 5.4 – Change of the absorbance over 10 hours of bacterial solutions having concentration C_2, C_3 and C_4, as calculated from our absorbance data. The graph shows raw data (black line) and a double-exponential fitting curve (red line).

of which is inversely proportional to the initial concentration of the solution.

In order to explain the initial absorbance drop measured by the absorbance-measurement setup, the phenomena of bacterial settling and aggregation were investigated in our micro-chamber. These two phenomena are in fact known to occur in bacteria colonies [123], [124]. A solution with concentration C_4 was studied, as the most severe absorbance decrease was observed for this concentration.

Image processing was performed with ImageJ software and Matlab R 2015b software (MathWorks, US), on each stack of images.

5.4.1 Monitoring and quantification of bacterial settling and aggregation in the micro-chamber

The bacterial settling phenomenon was investigated in a 575 μm-thick chip, with same geometry as the one in Figure 5.2a. The micro-chamber was filled with a bacterial solution of concentration C_4 and inlet and outlet were closed. In order to capture the bacterial settling and their migration in the vertical direction, brightfield pictures at different focal planes were taken with a 20$\times$ objective (scheme described in Figure 5.5a). Given the depth-of-field of the objective of $\pm$ 5.7 μm ($n_{air} = 1.0002772$, $\lambda = 550$ nm, numerical aperture NA $= 0.22$), a spacing of 30 μm between consecutive focal planes ensured that the bacteria behaviour in different vertical positions of the chamber was captured. The vertical 30 μm-shift of the focal plane was committed to a piezo transducer mounted on the motorized stage holding the microfluidic chip. Starting from the bottom of the micro-chamber (0 μm), focal planes at 30 μm, 60 μm, 90 μm, 120 μm and 150 μm were chosen, the range of investigated focal planes being limited to the 150 μm vertical span of the piezo transducer. According to Stokes' law, a bacterium should take about 90

min to sink from the top to the bottom of the chamber of height $L = 575$ μm. After this time window, all the bacteria that sank to the bottom of the micro-chamber should form a layer of thickness z_{max}. z_{max} can be estimated by dividing the volume occupied by all bacteria, $V_{E.coli,tot}$, by the surface of the micro-chamber, having radius R, according to Equation 5.3

$$z_{max} = \frac{V_{E.coli,tot}}{\pi R^2}.$$ (5.3)

$V_{E.coli,tot}$ can be estimated by multiplying the volume occupied by a single bacterial cell, V_{cell}, if considered as a sphere of radius $r=1$ μm, and the total number of bacterial cells, N, calculated by multiplying the bacterial concentration C with the volume of the bacterial solution (*i.e.* the volume of the micro-chamber having radius R), as in Equation 5.4:

$$V_{E.coli,tot} = V_{cell} \times N = \frac{4}{3}\pi r^3 \times C \times \pi R^2 L.$$ (5.4)

By replacing Equation 5.4 in Equation 5.3, Equation 5.4 can be re-written as

$$z_{max} = \frac{V_{E.coli,tot}}{\pi R^2} = \frac{\frac{4}{3}\pi r^3 \times C \times \pi R^2 L}{\pi R^2} = \frac{4}{3}\pi r^3 C L.$$ (5.5)

Therefore, according to Equation 5.5, bacteria from a solution of concentration $C = C_4$ will precipitate forming a layer of thickness $z_{max} = 10$ μm.

To capture the full dynamics of the settling process, pictures of a given focal plane in the micro-chamber were taken every 20 s for 120 min. Initially, pictures taken at different focal planes after the injection of bacteria in the micro-chamber (Figure 5.5b, T = 0 min) appeared similar, as bacteria were in a planktonic regime. However, after 2 h the bottom of the micro-chamber appeared richer in contrast (Figure 5.5b, 0 μm) as bacteria sedimented. Pictures taken at superior focal planes appeared more clear because of bacterial depletion from the planktonic state due to settling (Figure 5.5b, 150 μm), confirming the absorbance decrease as shown in Figure 5.4. Images belonging to all focal planes showed an average gray scale value that increased over time (on our scale, white corresponds to 1 and black to 0) (Figure 5.5c). The layer of settled bacteria of thickness z_{max} was clearly captured by images taken at the 0 μm focal plane (Figure 5.5b, T = 120 min), which also revealed that bacteria settled to the bottom of the micro-chamber as aggregates, and no longer as dispersed bacteria. Aggregation was confirmed also by the increase of the image SD calculated for the 0 μm plane (Figure 5.5d), which clearly deviated from the one calculated for the other planes (30 μm, 60 μm, 90 μm, 120 μm and 150 μm), for which the layer of settled bacteria appeared blurred (Figure 5.5b, 150 μm plane, T = 120 min). The diverging "fan-shape" of the curves, happening

after about 40 min and considering the superior focal planes (from 30 μm to 150 μm), is probably due to diffusive light scattering, which increases with the increase of the distance between the objective focus and the scattering layer of already present settled bacteria. The small initial rise in all curves of Figure 5.5d eventually could be explained by minor aggregation phenomena happening from the beginning in each focal plane. Considering these results, we think that settling and aggregation are together responsible for the initial decrease in the absorbance measured by our device (Figure 5.4). In fact, upon settling, bacteria leave behind an increasingly-thick layer of transparent medium, approximatively saturating towards a value of $L - z_{max}$ after 1-2 h. A medium with higher transparency would evidently result in a lower absorbance. The role of settling in the initial decrease of the measured absorbance is also supported by the observation that settling and the absorbance drop occurred in the same time window of 1-2 h after injection of the bacterial solution in the microfluidic chip.

To deepen our understanding about bacterial aggregation separately from the bacterial settling, a dedicated microfluidic chamber with the same layout as in Figure 5.2a, but with 60 μm-thick chambers, was used. The bacterial solution was injected in the microfluidic chamber and inlet and outlet were closed. Brightfield pictures were taken every 30 s using a 5× objective, to monitor the bacterial aggregation in the micro-chamber over 10 h. The resulting 1200 frames-stack was then processed to quantify the dynamics of the aggregation, using the image-processing algorithm illustrated in Figure 5.6a. After applying a moving-average filter with a 5 min-window, the inverted background was subtracted to the image stack, removing in this way artefacts due to dust or particles along the optical path of the microscope or on the PDMS chip. Then, the contrast was enhanced and a threshold was applied to binarize the image, segmenting therefore black bacteria or aggregates over a white background. Figure 5.6b shows exemplifying images from the stack before applying the image-processing algorithm (Figure 5.6bi and 5.6bii) and after (Figure 5.6biii and 5.6biv). Finally, the size of the aggregates was measured for each frame (Figure 5.6c). The segmentation algorithm was able to detect planktonic bacteria at the beginning of the experiment (Figure 5.6biii) and the formation of bacterial aggregates (Figure 5.6biv), which started immediately after the injection and led to the formation of aggregates with about twice the size of planktonic bacteria after 1-2 h. This time-window matches our observations related to settling (Figure 5.5b, 0 μm focal plane). After this pronounced aggregate formation during the initial 2 h, the aggregation rate decreased and a plateau was reached after about 7 h.

Upon bacterial aggregation, the medium appeared more clear and transparent, as visible by comparing Figure 5.6biii and 5.6biv, leading to a higher transmittance when the absorbance is measured. Therefore, we think that, beside depletion of the planktonic bacterial concentration due to settling, aggregation is a key-player in the initial decrease of the absorbance (Figure 5.4). This is also supported by the observation that bacterial aggregation and absorbance drop occurred in the same time window of 1-2 h after injection of the bacterial solution in the microfluidic chip.

After the first 1-2 h window, a slight increase in the absorbance was measured, indicating
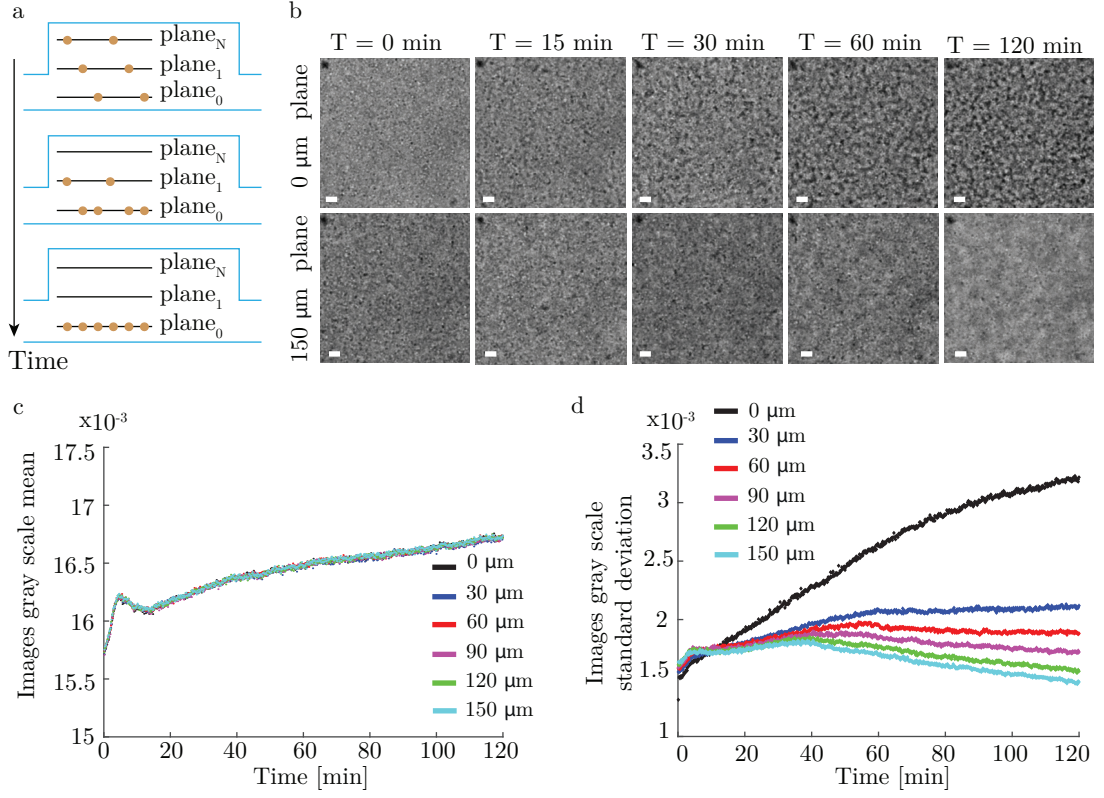
Figure 5.5 – Monitoring of bacterial settling in the micro-chamber via brightfield microscopy. a) Illustration of the settling movement of bacteria over time towards lower planes of the micro-chamber. Eventually bacteria are only present on the micro-chamber bottom ($plane_0$). b) Representative brightfield pictures over time of a micro-chamber filled with a bacterial solution at the 0 μm focal plane (bottom) and at the 150 μm focal plane (top). Scale bar = 10 μm. c, d) Quantification of the settling dynamics as variation of (c) the mean gray intensity and (d) the standard deviation of the gray scale values of each image of the 6 stacks taken at 0 μm, 30 μm, 60 μm, 90 μm, 120 μm and 150 μm, respectively.
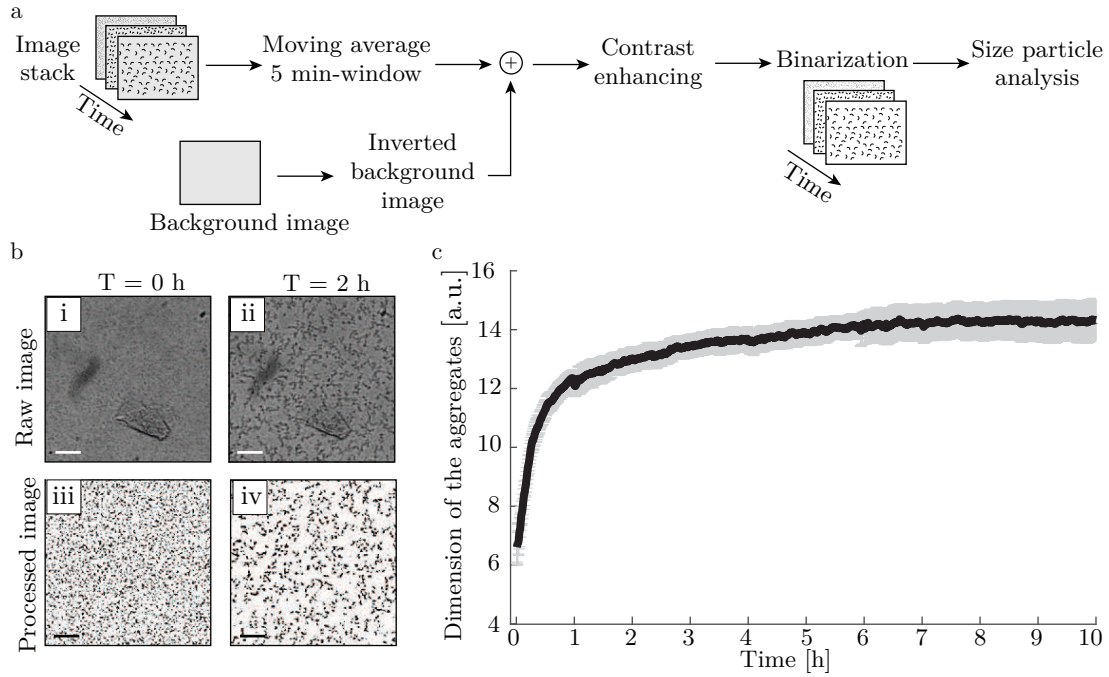
Figure 5.6 – Monitoring of bacterial aggregation in a 60 μm-thick micro-chamber via brightfield microscopy. a) Schematic of the image-processing algorithm applied to the 10 h stack of images, which was used to segment planktonic bacteria and the aggregates. After cleaning the images from undesired dust or particles with a moving average and background subtraction, the contrast was enhanced and a threshold was used to binarize the image. Finally, the size of the bacterial aggregate particles was measured. b) Two representative brightfield pictures of the micro-chamber, taken with a 5× objective after it was filled with the bacteria solution, (i) before applying the segmentation algorithm at the beginning of the sequence, (ii) after 2 h, and after applying the algorithm (iii) at the beginning of the sequence and (iv) after 2 h. Scale bar = 50 μm . C) Time-dependent change of the average aggregate dimension. The curve is expressed as average $\pm$ SD.

an increase in the turbidity of the solution (Figure 5.4), which can be attributed to bacterial settling on the glass surface coupled with more frequent and stronger intercellular interactions triggered by close proximity and confinement of bacteria at the micro-chamber bottom. The fact that aggregation continued even after 1-2 h and reached a plateau after about 7 h (Figure 5.6c), could be an indicator of the reorganization among the cells [88], [89]. In fact, literature data already showed that optical absorbance of a solution of cells varied with respect to the level of interaction between cells, which continue to reorganize themselves over time [120]. However, deviations from the linear relation between concentration and absorbance described by the Lambert-Beer law were reported in case of highly concentrated and non-dispersed media [125], [126]. For this reason, once bacteria aggregated and sedimented at the micro-chamber bottom forming a very dense colony, its concentration might not be safely derived from the absorbance.

5.4.2 Mathematical model for the absorbance dynamics of bacterial solution in micro-chambers

In order to unravel the influence of contributions from planktonic vs. settled and aggregated bacteria to the absorbance, a mathematical model of the change in the absorbance was designed to fit the experimental results. The volume of the micro-chamber can be subdivided into three parts V_x, V_y, V_z of height x, y and z respectively (Figure 5.7a). V_x is the "depleted" volume, ideally transparent because bacteria disappeared from the solution when settling down. V_y and V_z are respectively the volume in which bacteria are in their planktonic state and the volume occupied by settled bacteria. According to the Lambert-Beer law for multiple absorbers, Equation 5.1 can be generalized in Equation 5.6

$$A = log_{10}\frac{I_0}{I} = k_\lambda(C_x x + C_y y + C_z z),$$ (5.6)

where C_x, C_y and C_z are respectively the concentrations of the solution in the volumes V_x, V_y and V_z. In particular, C_y corresponds to the initial concentration of the solution C. Neglecting the contribution from V_x, which ideally is optically transparent, the absorbance can be calculated according to Equation 5.7

$$A = k_\lambda(C_y y + C_z z) = \frac{y}{y_0} + \frac{z}{z_0},$$ (5.7)

where $y_0 = 1/k_\lambda C_y$ and $z_0 = 1/k_\lambda C_z$. According to our hypothesis, bacteria start aggregating upon injection at time t_0, in clusters having a radius of about 1.5 μm, and settle with velocity v. I assumed as negligible the initial contribution of V_z, given that the solution in V_y has about the initial concentration C and that $y \gg z$. After about 1.5 h (at time t_1), settling is saturated and all the bacteria occupy a volume of height z_{max}, $y = 0$ and ideally only V_z contributes to the absorbance. The change of absorbance over time $A(t)$ can be expressed according to Equation 5.8 and the time-change of $A(t)$ is
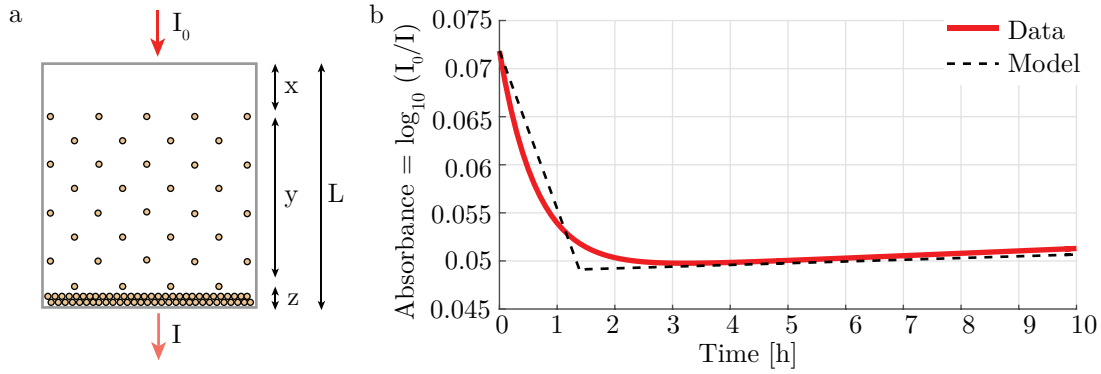
Figure 5.7 – Model of the absorbance change over time. a) Schematic of the lateral view of the measurement chamber of height L. Three parts are identified, having respectively a height of x, y and z. x represents the depleted zone, optically transparent because bacteria disappeared there when settling, and therefore does not contribute to the overall absorbance. y represents the region where bacteria are in a planktonic state. Finally, sedimented bacteria occupy a region of height z. Dimensions not in scale. b) The change of absorbance measured for a solution of concentration C_4 by our absorbance measurement setup, as reported in Figure 5.4 (solid red line) and change of absorbance from the model that was designed to fit the measured data and the experimental results (dashed black line).

plotted in Figure 5.7b.

$$
A(t) = \begin{cases}
\dfrac{L - vt}{y_0}, t < t_1 \\[3mm]
\dfrac{z_{max}}{z_0}(\beta + \alpha t), t \geq t_1
\end{cases}
\tag{5.8}
$$

α is a fitting constant of the model equal to $\dfrac{z_0}{z_{max}A(t = t_1)}$.

5.5 Materials and methods

5.5.1 Fabrication of the microfluidic chip

All the chips were fabricated starting from a 60 μm-thick SU-8 silicon mold by traditional photolithography as described in Chapter 2. Starting from these wafers, to fabricate the chips used to measure the absorbance and to study settling, tape disks were laminated on top of the measurement and reference chambers, increasing the thickness in a single step process. Such 515 μm-thick self-adhesive round-shaped tape (diameter of 3 μm) were previously cut by a laser cutter (Plotter Cutter RoboPro CE5000-40-CRP, Graphtec America, US). On the other hand, for the chip used to study bacterial aggregation, no additional layer was patterned on top of the initial 60 μm-thick SU-8 pattern. For all the wafers, the mold was used for PDMS casting, following the steps described in Session 2.3.

5.5.2 Bacterial preparation

HT115 *E. coli* bacteria were grown in LB with 100 μg/mL ampicillin and 12.5 μg/mL tetracycline overnight in a thermal shaker at 37 °C. The following day, 50 μL of the confluent bacterial cultures were used to inoculate freshly prepared LB medium containing only ampicillin and were grown overnight. After the overnight culture, 50 mL of the bacterial cultures were centrifuged to remove LB; in this way, bacteria samples with the desired optical density were obtained by adding S medium accordingly. The concentration of each bacterial solution was measured using a commercial spectrophotometer (WPA CO8000, Biochrom, UK). Fresh bacterial solutions were prepared before each experiment.

5.5.3 Image acquisition and platform control

Image aquisition and platform control were performed by using the setup described in Section 2.4. The acquisition system was programmed so that pictures were automatically captured. For the settling experiments, pictures were recorded every 20 s for 2 h using a Zeiss 20x NA 0.22 objective. For the aggregation experiments, pictures were recorded every 30 s for 10 h using a Zeiss 5x NA 0.13 objective. The microfluidic chambers were filled either with S medium (reference chamber) or with the bacterial solution under investigation, using a flow rate of 1000 nL/s. After chip filling, the chamber inlet and outlet were clamped and kept in this condition over the full experiment. The experiments were performed at 25 °C.

5.6 Discussion and conclusion

I presented in this Chapter a miniaturized optoelectronic platform integrated in a microfluidic device, which was able to measure the on-chip absorbance of planktonic bacteria in the 1-5 $\times$ 10^9 cell/mL concentration range. Relying on the Lambert-Beer's absorption principles, I designed two independent fluidic chambers, the reference and measurement chambers, each configured with a LED-PD pair to measure the corresponding transmittance. By connecting in series the two LEDs, relating the signal from the measurement chamber to the one from the reference channel and filtering opportunely, a nearly noise- and fluctuation-free absorption measurement was obtained. Compared to previous solutions, this platform permitted the quantification of bacterial concentrations in an automated way, and is therefore less error-prone and time-consuming. Furthermore, the quantification of a bacterial concentration, which is currently microscopy-based and often involves manual counting, was here assured using a system of small commercial opto-electronical components that made the measurement affordable and the device portable. The system was able to measure the concentration of a bacterial sample with a volume of about 7 μL, which is three orders of magnitude smaller than the volume

required by most of the commercial spectrophotometers. Moreover, this general-purpose device can be possibly put in fluidic connection with a separate microfluidic chip inoculated with bacteria of unknown concentration, in a modular fashion, with a negligible dead volume. Upon testing the device with bacterial solutions of different and known concentration, a linear calibration curve was obtained. The on-chip absorbance was measured over 10 h in absence of flow for solutions with concentration C_2, C_3 and C_4. For the three cases, I found that the measured absorbance consistently dropped after 1 h, revealing that the bacterial solution became more optically transparent, and this in a concentration-dependent fashion. I hypothesized that the driving forces of such a change in the turbidity of the solution could be found in the phenomena of bacterial settling and aggregation. Tailored experiments were performed to investigate bacterial settling and aggregation using the concentration C_4, for which the most dramatic changes were observed. I found that bacterial settling and aggregation promptly started upon the injection of the solution in the micro-chamber and lasted for 1-2 h. This time window matched the dynamics of the absorbance change measured by our optoelectronic device. The two phenomena were not independent and the initial absorbance drop was likely to be due to a combined process, during which settling increases the chances of intercellular interactions and bacterial clusters of increasing size settle down easier, reaching eventually the chamber bottom in about 1-2 h. The absorbance measured for a solution with concentration C_4 showed the highest drop, while a milder decrease was observed for more diluted solutions. This inverse-dependence of the absorbance decrease on the concentration of the solution can be explained with the fact that aggregation and settling of a massive number of bacteria significantly altered the transparency of the solution. On the other hand, the fewer intercellular interactions and settling events occurring in a diluted solution did not result in an as dramatic absorbance change as the one observed for more concentrated solutions. Based on our observations, a simple mathematical model for the change of absorbance over time was hypothesized, according to which, bacterial settling and aggregation were the major players. Moreover, the absorbance change over 10 h can be fitted with a double-exponential trend (decreasing first and increasing afterwards), while the model here features an initial linear decrease due to settling and aggregation and a following slower linear increase.

5.7   Future outlook

From a future perspective, this platform could be used as a complementary stand-alone device that, on demand, can be put in fluidic connection with a separate microfluidic chip inoculated with bacteria of unknown concentration, and this in a modular fashion. More specifically, I could aim at measuring the concentration of the bacterial solutions that are used to culture *C. elegans* worms in microfluidic environments, to properly control their feeding. As *C. elegans* worms preferentially eat dispersed bacteria [19], [20], this study

revealed that injected bacterial solutions remain in the planktonic state only for about 1 h, after which they sediment. Therefore, after this short time window, the feeding solution in the worm culture chamber should be refreshed or stirred to re-suspend the bacteria. Envisioning a microfluidic platform where *C. elegans* worms are cultured on chip and their feeding is fully controlled, our miniaturized device can be connected to the feeding line of the *C. elegans* culture chip, either upstream or downstream. In this way, the same solution used to feed the worms could fill the measurement chamber of the device, to allow a real-time measure of its concentration. The exact control of the *C. elegans* feeding would allow performing reproducible culture experiments or precisely tuning the bacterial concentration to perform underfeeding or overfeeding experiments, paving the way for future worm metabolism studies.

6 Motility assay to evaluate the behavioral response to glucose on a *C. elegans* population

Abstract *C. elegans* being a relatively simple animal model, its motility gives direct information on its neuromuscular system and an indirect assay of the health of this nematode. Therefore, a quantitative evaluation of *C. elegans* motility can be used to assess the action of a drug at the whole-animal level. In this Chapter, I propose a simple yet powerful approach to assess the effect of small molecules, namely glucose and dynasore, at the behavioral level on YA worms by quantifying and comparing their motility before and after the compounds administration. I designed and fabricated a dedicated microfluidic device to deliver drugs to a YA population of worms in a precise spatio-temporal way, which made the experimental protocol robust and reproducible. A motility assay protocol was designed, where flow profile and video recording were synchronized. The designed image-processing routine was able to segment and quantify the motility for 10-12 animals in the micro-chamber. The results point at a critical role for dynamin in the cellular ability to uptake glucose, which was observed first at the behavioral level by quantifying worms motility and then confirmed at the whole organism level with the quantitation of glucose in *C. elegans*.

This chapter is an adapted version of the following publications:

- R. Trouillon, **M. C. Letizia**, K. J. Menzies, L. Mouchiroud, J. Auwerx, K. Schoonjans and M. A. Gijs, "A multiscale study of the role of dynamin in the regulation of glucose uptake", en, *Integr. Biol.*, Issue 9, p. 810-819, 2017.
- R. Trouillon, **M. C. Letizia**, M. A. M. Gijs, "Assessing electrochemically the chemical activity of cells in a cells-on-paper system". Proc. of 20th International Conference on Miniaturized Systems for Chemistry and Life Sciences (microTAS 2016), Dublin, Ireland, October 2016.
  Poster presentation
- R. Trouillon, **M. C. Letizia**, M. A. M. Gijs, "Quantitative analysis of chemical

release and uptake in cells-on-paper microsystems". Proc. of 39th International Conference of the IEEE Engineering in Medicine and Biology Society (EMBC2017), Jeju Island, Korea, July 2017.
Oral presentation and **poster** presentation

6.1 Introduction

C. elegans motility is a direct readout of the neuromuscular system and an indirect assay of the health of the animal [127]. Therefore, motility can be used to quantify the action of a drug at the whole-animal level. In this perspective, both the detection of the drug's action on worms and worms handling should be automated. In fact, precise specification of different locomotion phenotypes, such as velocity, amplitude of the movement, angles of body bends etc., cannot be provided through mere visual observation, and machine vision approaches for automated behavioral analysis are required. Many machine vision methods have been described to quantify behavioral phenotypes [128]. The majority of these algorithms share the same image-processing-based features: extract individual frames from a movie, segment the area occupied by worms by applying a threshold, compute the skeleton of each worm and finally extract motility parameters, such as center of mass and body curvature.

Although many sophisticated methods have been proposed [128]–[133], they are optimized for worm culture in solid medium, and are not ideal to quantify the swimming behavior characteristic in microfluidic devices [128]. In fact, *C. elegans* in liquid media shows substantially different moving patterns compared to worms in agar plates: when placed in a liquid, worms thrash, *i.e.* swim with a rhythmic and oscillating body motion [127]. Swimming offers a useful measurement, well-suited for the readily-scorable, phenotypic readout required for a screening, as it can be quantified as simple scalar numbers, such as the amplitude of its movement or the number of body bends per minute. Approaches based on worm segmentation and skeletonization were developed [134]. Other groups proposed methods based on measuring the differences between consecutive frames to quantify motility [135], [136]. However, microfluidic devices were not used in all these motility assays, and to perform the experiments, worms were on purpose transferred to microwells. Therefore, the worms handling was not automated, and the drug delivery protocol could not be carefully synchronized with the video recording. Moreover, these methods required that only one animal was present in the field of view. Interestingly, another group recently used an adapted version of a previous tracker [131], modifying the parameters to track the motility of multiple worms in a microfluidic chamber by using a segmentation/skeletonization approach [137].

In this Chapter, I propose a simple method to evaluate the effect of chemicals on a population of *C. elegans* worms in a microfluidic chamber. The method allowed precise synchronization of drug delivey and video recording. Moreover, in order to evaluate the drug effect, a motility score was obtained in a differential approach, by comparing motility values calculated before and after drug exposure.

The method was validated by investigating the links between glucose uptake, via insulin-regulated glucose transporter (GLUT4) exocytosis, and dynamin in a population of synchronized *C. elegans* worms. Dynamin is a molecular motor normally involved in endocytosis but also found to contribute to exocytosis through the dilation of the fusion pore, as exposure to the selective inhibitor dynasore was found to block exocytosis

a

b
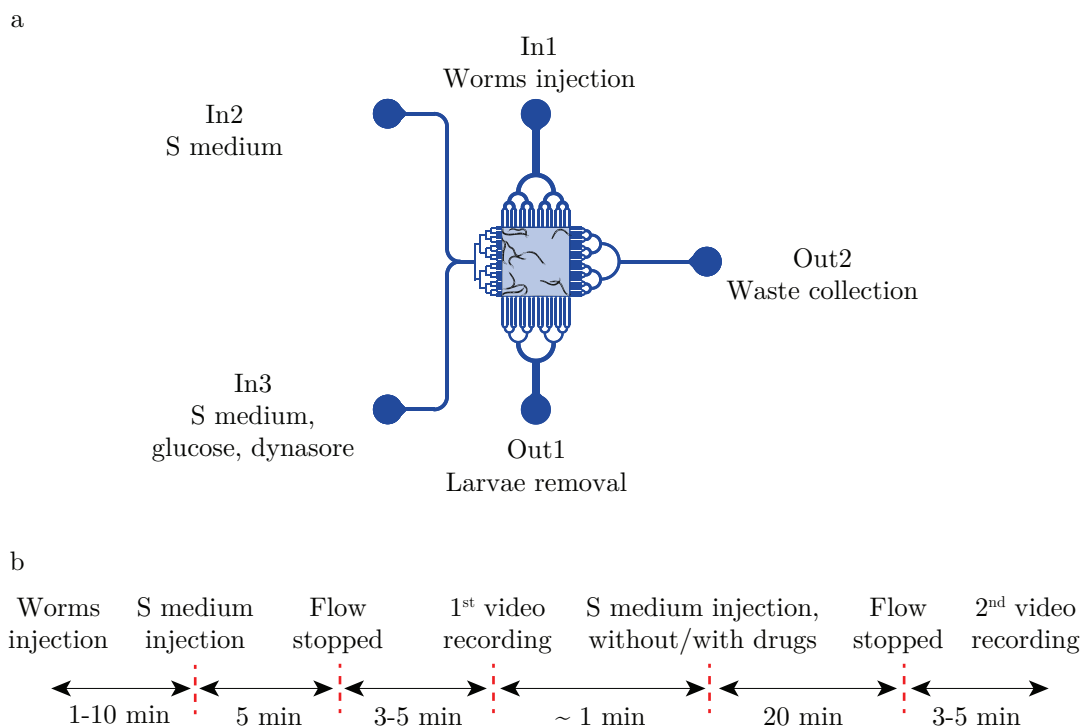
Figure 6.1 – Microfluidic-based approach for worm motility assay. a) Design of the microfluidic chip, featuring three inlets - one for worm loading and two for the injection of S medium and drugs - and two outlets. b) Time line of the worm motility assay protocol.

[138]. A custom microfluidic setup allowed for a controlled and reproducible drug testing assay, perfectly synchronized with the video recording. Our quantitative analysis of the nematodes behavior suggested that dynasore alters worms response to high glucose exposure.

6.2 A microfluidic-based approach for worm motility phenotyping assay

Microfluidic chips were designed to quantify worm motility before and after animals are exposed to the compound under investigation. Chips were prepared by standard soft lithography using a 2-layer SU-8 master as described in Chapter 2. The chip design is shown in Figure 6.1a. The main feature of the chip is a 2×2 mm^2 microfluidic chamber, dedicated to adult nematode maintenance and treatment, connected to three inlets – In1, In2 and In3 – dedicated respectively to worms loading, S medium refreshing and treatment injection, and two outlets – Out1 and Out2 – fitted respectively with 60 μm and 30 μm filters. These filters allow for size selection of the nematodes, so that only adult hermaphrodite worms are retained in the chamber. Microchannels are 40 μm-high, while the height of the chamber is 130 μm. The microfluidic chip was integrated into the

Figure 6.2 – Schematic of the image processing routine to quantify the worm motility score. a) Image cropping by manual selection of the region of interest, corresponding to the worm square chamber. b) Image binarization by thresholding. c) Differentiation of the binary video to quantify the number of non-null pixels, characteristic of the worms motility. Scale bar = 500 μm

microfluidic setup described in Section 2.4. A 5×/0.12 A-Plan Zeiss objective was used. Videos were recorded with a Pixelink B681 CMOS Camera (Pixelink, US).

The worm loading and synchronization procedures resemble the ones described in Chapter 3. A mixed population of worms was suspended in 200 μL of S medium and aspirated into a tubing connected to the device. With a flow ranging from 200 to 800 nLs^{-1}, the unsynchronized worms were injected in the microfluidic chamber from inlet In1. Worm synchronization was automatically performed hydrodynamically through Out1. This outlet filter was tailored with 60 μm-wide and 800 μm-long channels, in such a way that only adult worms were retained in the chamber, while younger worms were washed away by the flow. The number of worms retained in the chamber was controlled by adjusting the volume of the injected solution, from 5 μL up to 20 μL. After worm synchronization, Out1 was closed and Out2 opened. The worms were then exposed to a constant flow of 30 nLs^{-1} of S medium, from In2 for 5 min, to remove the residues of OP50 bacteria and any metabolic waste from the chamber, and also to expose the worms to a basal level of hydrodynamic conditions. The tailored filters cast on the Out2 side, *i.e.* 30 μm-wide channels, prevented the adult worms from escaping. Then, the flow was stopped, and the first video was recorded (5 sec, 20 fps). After the first recording, the second solution (S medium without/with the investigated drug) was injected for 20 min, at a flow of 30 nLs^{-1}, from In3. Finally, the second video was recorded. In order to avoid any effect of the flow on worm motility, the flow was stopped for 3-5 min before starting both recordings. The time sequence of the worm motility assay is shown in Figure 6.1b.

Each video was converted to grayscale and processed using a custom routine written in IgorPro (WaveMetrics, US) to extract a motility score. The data processing routine is summarized in Figure 6.2. First, the area of interest, corresponding to the central chamber, was selected and extracted from each frame (Figure 6.2a). Each of these reduced frames was then converted to a binary image using a user-defined threshold

(Figure 6.2b). This threshold was adjusted so that the shape of the worms appeared clearly, but all the other features, such as debris or the edges of the PDMS channels, were cancelled. The same threshold was used for each frame of the video. The number of white pixels, corresponding to a "1" value, were counted for each frame and averaged over the duration of the video, thus providing a measure of the fraction of the image occupied by the worms. In a second step, the binary video was differentiated using the forward difference method (Figure 6.2c). Briefly, the number of non-null pixels, indicative of worm motion, was counted for each frame, and these values were averaged over the whole video. This value, describing the rate of change of the frames and therefore the worm activity, was normalized to the average worm area computed above, thus providing the motility score for this video. Finally, motility was quantified as the variation of this motility score, before and after the drug treatment, which was defined as the ratio of the score after the treatment to the score before the treatment. To prevent from overloading the memory of the computer, the algorithm was typically run over 3 s of the video. The rest of the file was used to ensure that the behavior of the worm was consistent over the duration of the video. To guarantee the relevance of the computed motility value, I ensured that the worms were not overlaid or crowded, which would have impaired the computation of the worm area, for instance. Also, stopping the flow allowed the worms to swim freely and therefore to spread evenly in the chamber. Finally, the videos were captured at a point where the worms were found to be isolated from each other.

6.3 Effect of glucose uptake and inhibited glucose uptake on *C. elegans* motility

A motility assay was performed to quantify the effect of glucose and dynasore exposure on *C. elegans* adult worms. Briefly, glucose uptake by muscle cells upon insulin signaling is a fundamental mechanism for metabolism [139]. Insulin binds to its membrane receptor on a muscle cell, thus triggering an intracellular kinase cascade leading to the mobilization of GLUT4 storage vesicles. These vescicles are translocated to the rim of the cell, where they can tether and fuse with the cell membrane following an exocytosis process. This allows for the integration of the GLUT4 into the membrane, where they can take up glucose. Diseased states, such as diabetes, in which cells are not able to respond to an insulin stimulus, are characterized by the inability to mobilize the specific GLUT4 [140]. Dynamin is a molecular motor normally involved in endocytosis [141] but also found to contribute to exocytosis [142] through the dilation of the fusion pore [138], as exposure to the selective inhibitor dynasore was found to block exocytosis [143].

Cell experiments indicated the role of dynamin in glucose uptake [74]. However, cell models are too simple to account to the complexity of life. The aim of the present study is to understand if dynasore interacts or inhibits glucose uptake at the whole-animal level, and if behavioral responses to glucose are triggered in a *C. elegans* population. High glucose concentrations are known to have deleterious effects on nematodes development

[144] or to provoke oxidative stress [145], and to reduce the motility of hermaphrodite worms [146]. First, a motility assay was performed to characterize the concentration-dependent effect of glucose (Figure 6.3a). It was found that the worm motility is progressively reduced by increasing concentrations of glucose, and that a motility drop by 50% is reached when a glucose concentration of 200 mM is used. Therefore, a concentration of 200 mM glucose was chosen to maximize the effect of the treatments in the following experiments. The concentration-dependent effect of dynasore was then tested on untreated worms and on worms exposed to 200 mM of glucose (Figure 6.3b). In the absence of glucose, the motility decreased with increased dynasore concentrations as this drug impairs membrane trafficking. This agrees well with a toxic effect *in vivo* of dynasore at high concentrations. Interestingly, in the presence of 200 mM glucose, the dose response to dynasore changed dramatically and became "U-shaped". Low concentrations (up to 100 nM) seemed to increase the observed glucose toxicity, the lowest motility being recorded for 100 nM. However, for dynasore levels higher than the 100 nM-limit, the motility increased too, up to the levels of motility observed in the absence of glucose with 10 μM dynasore. This finding suggests that high dynasore concentrations cancel the effect of glucose, possibly by blocking GLUT4 exocytosis and glucose uptake.

L-glucose, an enantiomer of glucose that cannot enter glycolysis was used to investigate the specificity of D-glucose (otherwise referred to as glucose in the text) in the observed variations in motility. In particular this molecule was used to disentangle the physical (osmolarity, viscosity) and the enzymatic, metabolic or biological effects of the previous treatments. L-glucose has a low affinity with GLUT4 [147], [148] and was previously found to show none of the typical harmful effects of glucose on *C. elegans*: the lifespan [144] and egg laying rate [149] were unaffected, and it displayed no toxicity in glucose-sensitive mutants [150]. Exposure to 200 mM L-glucose decreased the worm motility in a smaller magnitude than glucose (p-value= 0.004, motility ratio 0.75 for L-glucose vs. 0.52 for glucose) (Figure 6.3c). This drop can be attributed to the physical effect of the molecule, principally the increase in osmolarity, on the nematodes. From this result, it can be estimated that the $\sim$48% drop in motility due to glucose exposure is the sum of a $\sim$25% decrease due to the different physical conditions and another $\sim$23% drop in motility that can be attributed the biological impact of high glucose, probably leading higher oxidative stress. The L-glucose tests were also repeated for different concentrations of dynasore. Interestingly, the U-shaped response previously observed in the presence of glucose is abolished, and the trend of the response was comparable to the one recorded when no glucose is added. This further supports that the specific response seen for the co-exposure to glucose and dynasore arises specifically from the biological activity of glucose in *C. elegans*, and that dynamin takes part to this phenomenon.

Finally, to confirm the specific role of dynamin and its inhibition, worms were treated with a feeding RNAi targeted at *dyn-1*, the gene coding the dynamin isoform present in *C. elegans* (Figure 6.3d) [151]. The decrease in motility due to 200 mM glucose was less than for the untreated worms (motility ratio 0.67 for the RNAi vs. 0.52 for the untreated).

Additionally, the decrease in motility was similar for both glucose enantiomers, thus showing that the bioactivity of glucose does not alter the behavior of these RNAi-fed worms. As with dynasore, inhibiting the activity of dynamin via RNAi feeding blocks the biological response to glucose.

In order to support the hypothesis that dynasore blocked glucose uptake, the worm glucose content was measured under different conditions. To do so, unsynchronized populations of about ∼2700 worms were exposed to high glucose concentration (200 mM), either without or with 1 μM dynasore. Those populations were then lysed and the total glucose content of the lysate was quantified electrochemically, with the help of a collaborator (Figure 6.4). Our results showed that dynasore blocked the accumulation of glucose in the worms.

Overall, this set of experiments further established the role of dynamin in glucose uptake, as its activity modulates the magnitude of the nematode response to glucose. Additionally, it also hints at complex whole organism effects, e.g. behavioral alterations, mediated by the altered biochemical status of the animal.

6.4   Materials and methods

6.4.1   Worm maintenance and preparation

C. elegans were cultured at 20 °C, in 90 mm Petri dishes, on NGM seeded with *E. coli* strain OP50 bacteria. The strain used in this study was the wild-type N2 strain, as obtained from the Caenorhabditis Genetics Center (University of Minnesota). RNAi clones *dyn-1* (C02C6.1) were purchased from GeneService and sequenced.

For the RNAi studies, HT115 *E. coli* bacteria for the control and RNAi experiments were grown LB with 100 μg/mL ampicillin and 12.5 μg/mL tetracycline overnight in a thermal shaker at 37 °C. The following day, 50 μL of the confluent bacterial cultures were used to inoculate freshly prepared LB medium containing only ampicillin (100 μg/mL). The new cultures were grown until reaching an optical density between 0.6-0.8. Plates were induced overnight at room temperature with 2 mM isopropyl β-D-1-thiogalactopyranoside (IPTG) and seeded with 90 μL of the culture of HT115 bacteria expressing the RNAi clones for the *dyn-1* gene. L4 worms were transferred on the RNAi plates and removed after 24 h of treatment. YA worms were then collected for introduction in the microfluidics system. In all the experiments, YA worms were harvested from the plates and suspended in solution prior to each introduction in the microfluidic system by rinsing the plates with fresh S medium.

6.4.2   Statistical analysis

Where applicable, the data are reported as average ± SD, and the number of individual measurements is described using the notation n. A Shapiro-Wilk test was run on
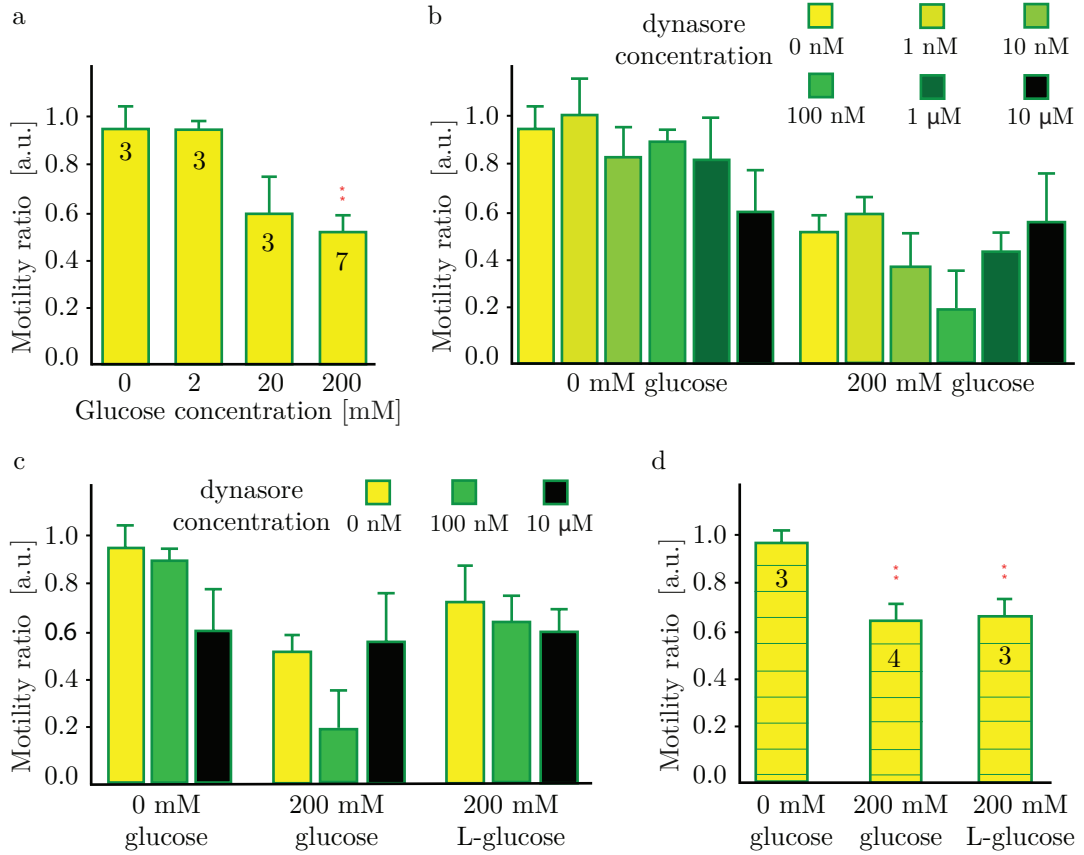
Figure 6.3 – Effect of glucose and dynasore on *C. elegans* motility. a) Effect of different glucose concentrations (2 mM, 20 mM and 200 mM) on worms motility. The number in each bar corresponds to the number of microfluidic chip used for each condition. A maximal drop in motility of 50% reached for 200 mM (p-value= $1.6\ 10^{-5}$ versus 0 mM glucose). b) Variations in motility score for different levels of dynasore, for 0 and 200 mM of glucose (p-value= $1.9\ 10^{-9}$ overall). c) Variations in motility score upon glucose and L-glucose exposure and different concentrations of dynasore. (p-value= 0.004, motility ratio 0.75 for L-glucose vs. 0.52 for glucose). d) Variations in motility score for upon glucose and L-glucose exposure nematodes treated with RNAi on *dyn-1* gene. *: p-value < 0.05. **: p-value < 0.01.
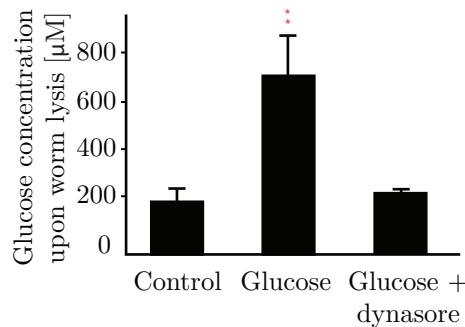
Figure 6.4 – Total glucose content measured electrochemically in worm lysates after exposure to 200 mM glucose, without or with 1 μM dynasore and control without dynasore or glucose (n = 3 for each case, each repeat corresponds to the lysate of $\sim$2,700 worms).

the different control datasets obtained in the study to test the normality of the data. Comparisons between two different datasets were performed with a two-tailed Student's t-test, or with a 1-way ANOVA in the case of more than 2 datasets, followed by a post-hoc two-tailed Student's t-test if further comparisons are required.

6.5 Discussion and conclusion

In this Chapter, I propose a simple yet powerful approach to quantify the *C. elegans* motility as a phenotype. This method enabled assessing the drug effect at the behavioral level and was exploited upon exposure of *C. elegans* YA worms to glucose and dynasore. The results presented in this Chapter point at a critical role for dynamin in the ability of cells to uptake glucose upon insulin stimulation. Importantly, evidence for this was found *in vivo*, by taking advantage of microfluidics and the ease of culture of *C. elegans*. The role of dynamin in glucose uptake was observed first at the behavioral level by quantifying worms motility and then confirmed at the whole organism level with the quantitation of glucose in *C. elegans*, thus providing an extensive mapping of the role of dynamin. The experimental findings, in agreement with the literature, underline the fundamental role of dynamin in exocytosis. Dynasore blocked glucose uptake in *C. elegans*, but also altered the behavioral response of the nematodes to high glucose levels. The use of *C. elegans* is here relevant, as the insulin pathway is well conserved from this nematode to mammals. Altogether, these findings suggest that dynamin is involved in the response to insulin by mediating the membrane expression of GLUT4, probably by facilitating exocytosis, as previously reported in other systems [138], [142].

The use of a dedicated microfluidic device allowed chemical delivery in a precise spatio-temporal way, with full control of injection times and doses, which made the experimental protocol robust and reproducible. Moreover, I designed a motility assay protocol, where fluidic flow profile and video recording were coupled in a synergistic fashion. Compared to methods previously presented in literature, this approach can handle multiple worms in the same video frame, being able to segment and distinguish up to 10-12 animals.

Quantitation of worm motility upon exposure to drugs proved to be a powerful indicator of the molecule effect at the whole-organism level.

6.6 Future outlook

In the future, depending on the biological question, this method could be used to measure the long-term worms response to a drug, by taking small videos also at later time points and comparing the change in motility over time. Moreover, other more subtle phenotypes could be measured, such as angles of body bends, thrashing frequency, amplitude of the sinusoidal movement, velocity of head, tail and body center, etc.
Furthermore, fabricating a micro-chamber with filters of a different size would allow sorting and confining of worms of another developmental stage. Comparing the glucose effect among populations of different age could reveal a possible stage-dependent effect of glucose.

7 Design of 3D-printed micro-channel for NMR spectroscopy of a *C. elegans* subsection

Abstract Nuclear magnetic resonance (NMR) is successfully applied in a great variety of fields, from diagnostic imaging to *in vivo* spectroscopy of large living animals. Potentially, NMR could also allow for metabolic phenotyping on small organisms as *C. elegans*, but methods enabling the translation of this technique to the study of smaller volumes were not developed yet. In fact, experiments on subnanoliter (sub-nL) volumes are hindered by the limited sensitivity of the detector and by difficulties in positioning and holding such small samples in proximity of the detector. While the detectors sensitivity is optimized by miniaturizing its dimensions to match the size of the specimen, the sample handling becomes more difficult as the size of the detector is scaled down. In this Chapter, I report NMR experiments on *C. elegans*, immersed in liquids having volumes down to 100 pL. To do so, a microfluidic device was designed to allow positioning and holding of *C. elegans* over the sensitive region of the detector. The device was fabricated using a high spatial resolution 3D printing approach, which allowed placing the sample and the coil in close proximity, crucial to exploit the volume of maximum sensitivity of the detector. The system was first tested and calibrated in water, and then used to collect NMR peaks from a *C. elegans* subsection. The obtained results indicate a promising route for NMR studies at the single-organism level of important biological entities having sub-nL volumes, such as living microscopic organisms and eggs of several mammalians, including humans.

This chapter is an adapted version of the following publications:

- E. Montinaro, M. Grisi, **M. C. Letizia**, L. Pethö, M. A. M. Gijs, R. Guidetti, J. Michler, J. Brugger and G. Boero "3D-printed microchannel for sub-nL NMR spectroscopy", en, *PLOS ONE*, manuscript accepted.
- E. Montinaro, M. Grisi, **M. C. Letizia**, M. A. M. Gijs, J. Brugger, G. Boero, "Nuclear magnetic resonance spectroscopy of subnanoliter samples by single chip

detector and microfluidic channels". Symposium LATSIS, 2016, Lausanne
Poster presentation

7.1 Introduction

Methods based on the NMR phenomenon are widely used in physics, chemistry, medicine and biology [152]–[154]. In traditional NMR experiments, the sample is placed in a static magnetic field and excited with electromagnetic fields at frequencies and strengths that are not harmful to biological entities. Due to this property and to its resolving power, NMR is successfully applied in a great variety of fields, such as diagnostic imaging [155], [156] and *in vivo* spectroscopy [157], [158] of large living animals. The use of NMR methodologies for the study of sub-μL volumes is hindered by sensitivity limitations. The search for methods enabling the translation of this powerful technique to the study of smaller volumes is therefore an active research domain. These efforts include both the miniaturization of inductive methods [159]–[164] and the use of more sensitive but less versatile non-inductive approaches [165]–[167]. Various techniques allowed optimizing NMR inductive detectors for volumes ranging from 1 μL down to a few nL. Some of these were used to perform pioneering studies of small collections of microorganisms [168]–[170], perfused tumor spheroids [171], and large single cells and embryos [172]–[175]. However, NMR-based studies of intact single biological entities were, until recently, demonstrated down to volumes of 5 nL [173], [176], whereas typical volumes of most cells and microorganisms are below the nL scale [177]. Recently, the use of ultra-compact single-chip NMR probes as convenient tools to deliver state-of-art spin sensitivity for sub-nL volumes was reported [163], [178]. Such probes consist of a multilayer microcoil and a co-integrated low-noise electronic transceiver. Thanks to the achieved sensitivity, researchers were able to perform the first NMR spectroscopy studies of single untouched sub-nL ova of microorganisms having active volumes down to 0.1 nL [178]. These experiments, however, were conducted by manually placing the sample on top of the microcoil using a polystyrene cup filled with agarose gel [178]. This study demonstrated the detection of highly concentrated endogenous compounds, but improvements concerning sample manipulation are required to enable long-lasting experiments in more biocompatible environments. A microfluidic-based approach would improve many aspects of NMR experiments. First, the study of biological samples in liquids would provide a more biocompatible environment, where oxygen and nutrients are continuously provided to the sample. Second, the use of a microfluidic device would facilitate a non-invasive sample handling and would provide a controllable environment during the experiments. Moreover, a microfluidic-based approach would possibly allow performing NMR experiments upon delivery of drugs, to compare the metabolic content before and after the drug administration. To perform NMR spectroscopy studies on small biological entities in a liquid environment, relatively complex microfabrication techniques are required, in particular for the placing and holding of the samples in the sensitive region of the miniaturized detector. Several approaches to combine microfluidic structures with microsolenoids [159], [168], [179]–[181], and planar microcoils [182], [183] have been reported. Various techniques were developed to reduce the size of solenoids and pattern them on capillaries [184]–[186] or around hollow pillars via wire bonding

[179], [187]. At the sub-nL volume scales, an efficient combination of microsolenoids with microfluidic structures would require significantly more complex microfabrication processes than the one for planar microcoils with planar microfluidic structures.

In this Chapter, I report the design and fabrication of a microfluidic device capable to deliver and hold a *C. elegans* nematode in a sub-nL sensitive volume of a planar microcoil, used for NMR signal excitation/detection, integrated on a silicon chip. The single chip detector offers a robust planar working surface, but its very small detection volume of about 0.2 nL requires the nematode to stay in close proximity to the microcoil without introducing significant static magnetic field inhomogeneities. To overcome these challenges, a microfluidic device was fabricated using a 3D printer and able to provide resolution better than 1 μm^3. This approach enabled the fabrication of micro-channels capable to confine the samples under investigation at a distance of about 10 μm from the microcoil surface. Upon calibration of the system using pure water, experiments on *C. elegans* were performed. Despite the *C. elegans* volume of about 100 pL and the broad intrinsic linewidth (about 30 Hz at 300 MHz) of these samples, the achieved sensitivity (2.5 $\times$ 10^{13} spins/Hz$^{1/2}$) was sufficient to detect highly concentrated endogenous compounds. The microfluidic channels were connected to a robust fluidic interface that tolerates the application of flows as strong as 7 μL/s and guarantees an efficient sealing for several days. The results of the reported experiments indicate that our approach allows for the non-invasive and efficient handling and trapping of *C. elegans* for NMR investigations at the sub-nL volume scale, in conditions of high sensitivity and sample limited spectral resolution.

7.2   Single-chip CMOS detector

The setup described in this Section was developed by collaborators at Laboratory of Microsystems 1, under the supervision of Professor G. Boero.

The single chip NMR detector, described in details in a previous publication [163], has an integrated excitation/detection multilayer microcoil with a diameter of 150 μm (Figure 7.1a). The integrated planar microcoil has a high sensitivity in a distorted spherical volume having a diameter of about 100 μm. The planar microcoil lies in the yz plane, with the static magnetic field B_0 along the z axis. Using the principle of reciprocity [188], the signal contribution per elementary volume $dS(r)$ (*i.e.* the local sensitivity) is proportional to $B_{xy}(r)sin(\vartheta)$, where $B_{xy}(r) = \sqrt{B_x(r)^2 + B_y(r)^2}$ is the field component in the xy plane (*i.e.*, perpendicular to B_0) produced by the microcoil carrying a unitary current, $\vartheta = \gamma B_{xy}(r)I\tau$ is the flip angle, γ is the nuclear gyromagnetic ratio, τ is the pulse length, and I is the current carried by the coil during the excitation pulse [152]. The maps of sensitivity of the integrated microcoil shown in Figure 7.1b were obtained computing $B_{xy}(r)sin(\vartheta)$, starting from the computation of $B_{xy}(r)$ via a Biot-Savart code implemented in Matlab. The sensitivity of the microcoil decreases rapidly with the distance along the x axis. As a result, the microfluidic system used to hold the sample on
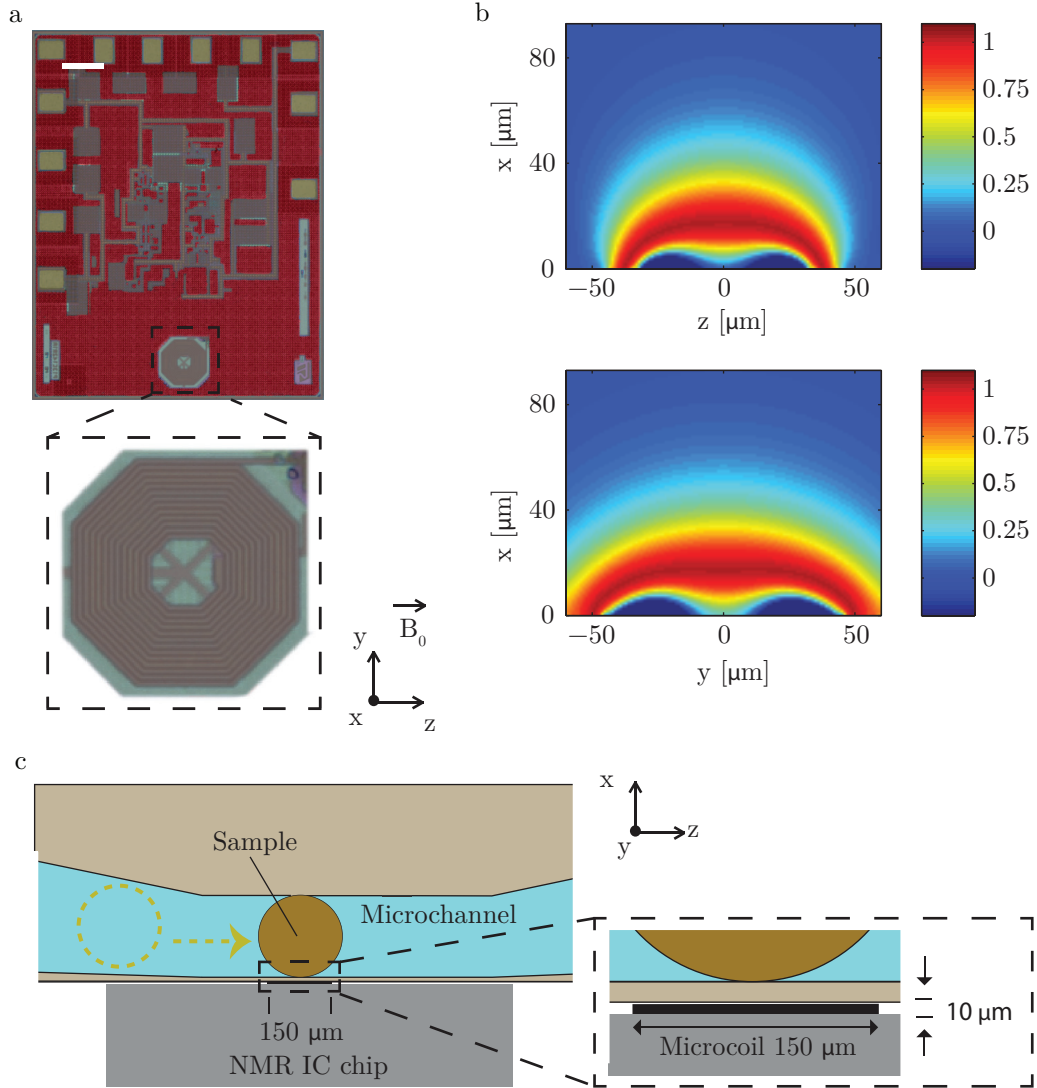
Figure 7.1 – Integrated electronic setup for NMR spectroscopy. a) Microphotograph of the NMR single-chip detector, fabricated using a 130 nm CMOS technology from STMicroelectronics. The integrated planar microcoil is realized using four copper metal layers. The total number of turns is 22 and the outer diameter is 150 μm. The details of the microcoil and of the co-integrated electronics are reported in Reference [163]. Scale bar = 150 μm. b) Normalized-sensitivity maps of the microcoil. The sensitivity is defined as $B_{xy}(r)sin(\vartheta)$. The microcoil lies in the yz plane and the static magnetic field B_0 lies along the z axis. The sensitivity in the xz (top) and xy (bottom) planes are computed for a pulse length $\tau = 3.7$ μs and an excitation current $I = 9$ mA. Dark red color identifies the region of maximum sensitivity. c) Illustration of the approach used to place the sample subsection, here represented as a sphere, onto the most sensitive area of the excitation/detection microcoil. The flow drives the sample in proximity of the integrated microcoil. The dashed arrow indicates the direction of insertion of the sample. A 10 μm-thick crosslinked photoresist layer defines the spacing between the sample and the chip surface.

top of the microcoil needs a thin separation layer. Variation of the pulse length τ implies a variation of the local flip angle ϑ, thus a variation of the spatial distribution of the sensitivity. The integrated NMR signal S is proportional to the integral of $dS(r)$ over the total volume of the micro-channel. Figure 7.1b shows the sensitivity maps for $\tau = 3.7$ μs, which is the pulse length that maximizes the integrated signal, assuming a separation $d = 10$ μm between the microcoil and the sample. Upon normalization of the integrated NMR signal to $S_{d=0\mu m}=1$ for the case of the channel volume placed in direct contact with the chip, the signals $S_{d=10\mu m}$ and $S_{d=20\mu m}$, evaluated in conditions of optimal τ, are respectively of about 0.7 and 0.5. Hence, a separation layer of 10 μm (Figure 7.1c) is an acceptable compromise between the loss of sensitivity and the robustness of the structure.

The single chip integrated NMR detector consisted of a radio-frequency (RF) power amplifier, a RF low-noise pre-amplifier, a frequency mixer, an audio-frequency (AF) amplifier, transmit/receive switches, and an excitation/detection microcoil. All NMR experiments described in this Chapter consisted of a RF pulsed excitation (about 300 MHz, pulse duration τ of a few μs) immediately followed by a detection time T_D (50 ms to 10 s). This simple excitation/detection sequence is repeated n times (1 to 10^6) with a repetition time T_R (50 ms to 10 s).

7.3 Design of a micro-channel to trap and immobilize a single *C. elegans* adult for NMR spectroscopy

A microfluidic device was designed to gently deliver, position and hold the sample in proximity of the detector microcoil, while providing a stable sealing over the duration of the experiments (Figure 7.2a). To easily align the sample with the microcoil under a microscope, the structural material of the micro-channel has to be optically transparent. The geometry of the channel is designed to minimize static magnetic field inhomogeneities and maximize the detected NMR signal amplitude. The microfluidic chip was configured with one inlet and one outlet, featuring a main entrance that splits into three channels that re-join at the outlet. The central micro-channel was designed to match tightly the size of an adult hermaphrodite worm, which is about 60 μm-wide, 50 μm-high and 1.3 mm-long. An array of 50 μm-high pillars with a 12 μm spacing was placed at the end of this channel in a V-shaped configuration, and used to block either the tail or the head of *C. elegans* (Figure 7.2b-d). The other two 55 μm-wide lateral channels were designed to fill the rest of the chip with nutrients, for animal survival during the measurement. To prevent the undesired trapping of other worms in the lateral feeding channels, one pillar was placed at their entrance (Figure 7.2a). A cross-section of the central part of the microfluidic structure is shown in Figure 7.2e,f. The gradual narrowing of the channels along their length was designed to facilitate the hydrodynamic trapping of the samples. The size and shape of the inlet and outlet parts were designed to match the capillaries used for the fluidic connection with the external pumps, limiting the presence
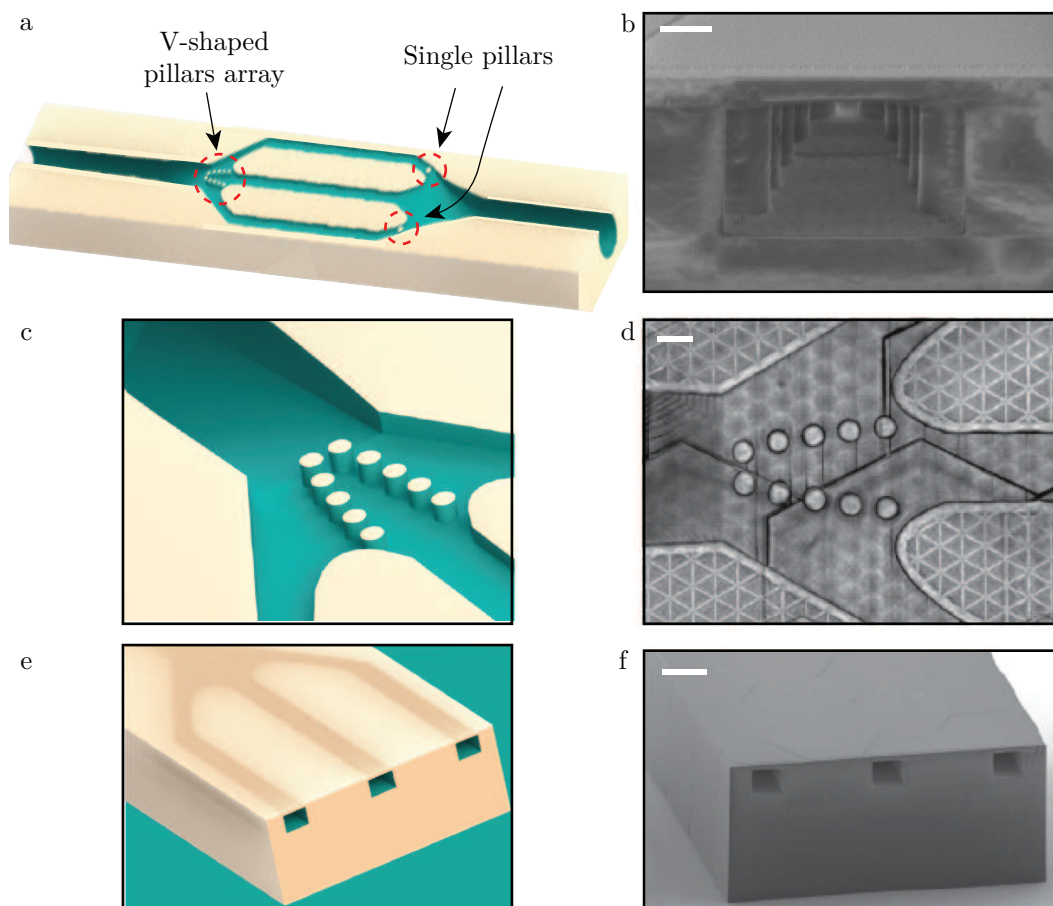
Figure 7.2 – Microfluidic chip to delivery and immobilize single *C. elegans* worm for NMR spectroscopy. a) Sketch of a cross-section of the microfluidic chip. b) Scanning electron microscope (SEM) picture of a 3D printed channel section showing the trapping pillars. Scale bar = 20 μm. c) Sketch and d) top view optical microscope picture of the pillars array used to trap the head or tail of *C. elegans*. Scale bar = 20 μm. e) Sketch and f) SEM picture of a 3D printed channel section showing the central trapping micro-channel and two lateral feeding micro-channels, closed from the top by a 10 μm-membrane. Scale bar = 60 μm.
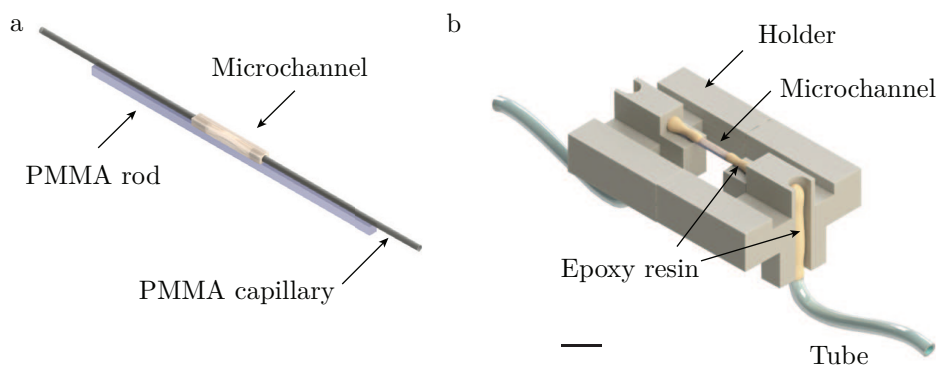
Figure 7.3 – Fluidic interface and holder of the microfluidic chip for NMR spectroscopy. a) The microfluidic channel was attached to a PMMA rod and connected to PMMA capillaries to create a fluidic assembly. b) The micro-to-macro interface was completed by connecting tubes to the PMMA capillaries and performing the casting of epoxy resin to create the sealing and give robustness to the fluidic system. Scale bar = 5 mm.

of dead volumes. Similarly, the thickness of the separation layer gradually changes over the micro-channel length, with a thickness of only 10 μm in correspondence of the most sensitive region of the detector (*i.e.* above the excitation/detection microcoil). With this design, the requirements of proximity for the maximization of the NMR signal amplitude and robustness of the structure were both respected.

In order to precisely position and tightly hold the microfluidic chip in contact with the single-chip integrated CMOS detector and to connect its micro-channels to the external pump, an interfacing structure was fabricated. The 3D printed microfluidic chips were first glued on a 200 μm × 2 cm PMMA rod for support using a cyanoacrylate adhesive (ECS500, 3M, US) (Figure 7.3a). Afterwards, PMMA capillaries (Paradigm Optics, US) were fitted in the inlet and the outlet of the 3D printed micro-channels. Finally, the realized assembly shown in Figure 7.3a was introduced into a 3D printed plastic holder (Figure 7.3b) fabricated by a conventional stereolithographic 3D printer (Form+1, Formlabs, US). The holder was patterned out of a photosensitive resin (Clear FLGPCL02, Formlabs, US) and was constituted of two complementary parts to allow for the insertion of the fluidic assembly. A system of tubes was connected to the fluidic assembly through the PMMA capillaries and a casting of epoxy resin was performed to seal the fluidic system and to give robustness to the structure. The assembled fluidic interface (Figure 7.3b) was manually brought into contact and aligned to the integrated excitation/detection microcoil under an optical microscope. Wax was used to hold the interface in position. A central squared aperture in the holder provided visibility for the alignment. With this system, we repeatedly achieved a good sealing, easy handling of the liquids, and a positioning of the sample within 10 μm precision.
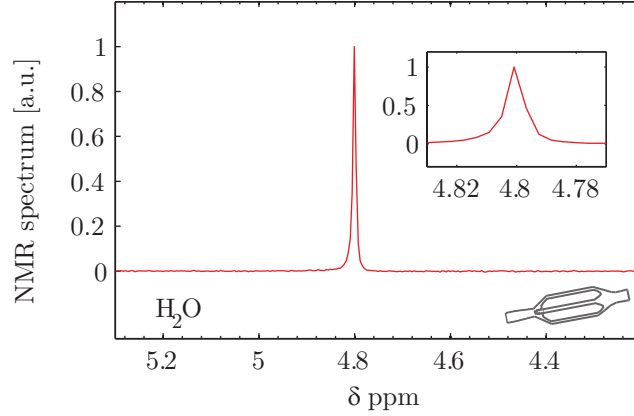
Figure 7.4 – ^{1}H NMR measurements on pure water in water performed at 7.05 T (300 MHz). V = 100 pL, number of averages = 1000, T_R = 4 s, τ = 3.5 μs, matching filter decay time constant $T_M = \infty$.

7.4 NMR spectroscopy of liquid samples

NMR measurements and data analysis were performed by collaborators at the Laboratory of Microsystems 1.

^{1}H spectra obtained from liquid samples (water and lactic acid in water) at 7.05 T (300 MHz) in the micro-channel were collected to characterize the spectral resolution limits of the setup and to measure the spin sensitivity of the detector. This NMR spectrum was also used to calibrate the sensitivity of the detector in combination with the microfluidic channel. All chemical shifts are expressed in ppm deviation from the resonance frequency of tetramethylsilane (TMS). Since this standard reference compound was not present in *C. elegans*, a chemical shift of 4.8 ppm was assigned to the peak of water, which is contained in the worm. The excitation pulse length used in the reported experiments (τ = 3.5 μs) corresponds to the experimental condition of maximum sensitivity, in good agreement with the value of 3.7 μs computed with simulations via sensitivity maps (Figure 7.1b). Figure 7.4 shows the ^{1}H NMR spectrum of pure water (Sigma-Aldrich, US) after averaging 1000 scans. The lorentzian fit of the data indicates a linewidth of 2 Hz full-width-at-half-maximum (FWHM). The baseline width, defined as the peak width at 0.55% height of the peak of water, is 24 Hz. These spectral resolutions were systematically achieved in six separated experiments employing six different micro-channels with the same nominal design. The obtained effective spin sensitivity is 2.5×10^{13} spin/Hz$^{1/2}$. Better spectral resolutions (down to 0.6 Hz) have been reported in literature [184], [189]–[191] but with probes having a worse spin sensitivity.
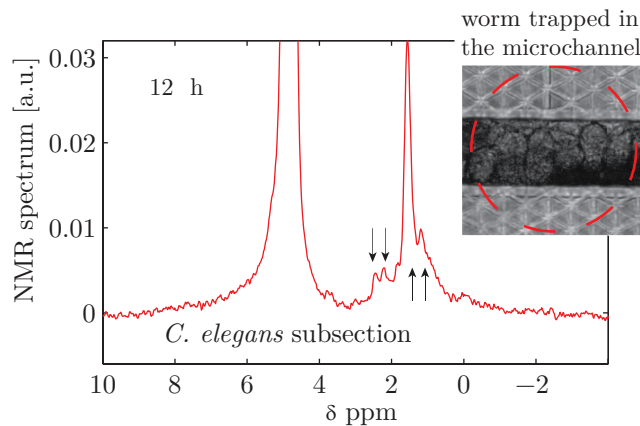
Figure 7.5 – ^{1}H NMR measurement on a *C. elegans* subsection at 7.05 T (300 MHz). The dashed circle indicates the 150 μm outer diameter of the integrated microcoil. V = 100 pL, number of averages = 113664 (12 hour), T_R = 200 ms, τ = 3.5 μs, matching filter decay time constant (T_M) = 30 ms. Arrows point at the peaks possibly associated to yolk lipids.

7.5   NMR spectroscopy of *C. elegans* subsections

NMR measurements on *C. elegans* were performed in collaboration with the Laboratory of Microsystems 1. Data analysis was performed by collaborators at the Laboratory of Microsystems 1.

In the experiments, the sensed portion of the *C. elegans* worm was given by the intersection of the sensitive region of the coil with the volume of the sample. Defining the active volume as the fraction of the sample that contributes to the 70% of the total signal and considering the geometries in play and their position with respect to the microcoil, an active volume of about 100 pL was estimated. The chemical shifts scale was obtained assigning a chemical shift of 4.8 ppm to the peak of water contained in the sample. Figure 7.5 shows the NMR spectrum obtained from a single *C. elegans* subsection, after averaging over 12 hours. During the experiment, *C. elegans* went through a delicate squeezing process when entering the micro-channel, whose size tightly matches the worm. Consequently, the channel section was entirely occupied by the worm. For this experiment, a subsection of the worm containing ova with was aligned the microcoil. As shown in Figure 7.5 (inset), a great part of the sensitive region was indeed occupied by about eight eggs contained in *C. elegans* abdomen. The peaks assignment was challenging due to the reduced size of the sample combined with the relatively poor spectral resolution. The peaks observed at about 0.9, 1.5, 2.1, 2.6 ppm may be mainly associated to yolk lipids. Some qualitative information can be obtained from previous ^{1}H high resolution magic angle spinning NMR studies on a collection of *C. elegans* [169] and on a single worm [176].

A prominent signal arises at a chemical shift of about 3.9 ppm. As shown in the Figure 7.6, the same resonance appears in the spectrum of *E. coli* in S medium, which is used as a base to feed the worm during the experiment. Therefore, such a resonance may
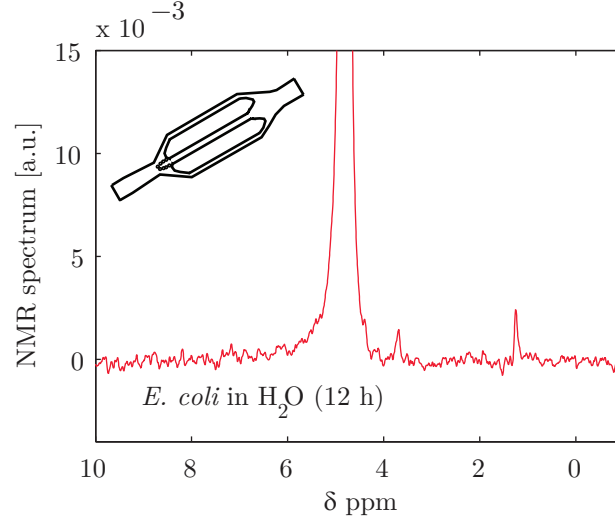
Figure 7.6 – ^{1}H spectrum of *E. coli* in S medium. NMR measurement performed at 7 T in the micro-channel. V = 100 pL; number of averages = 19800; T_R = 2 s, τ = 3.5 μs, matching filter decay time constant T_M = 60 ms.

result from the ingestion of nutrients operated by the microorganism. The linewidths are broader than the ones measured with water (Figure 7.4).

Although the performances of the system promote NMR spectroscopy as a promising technique to quantify the concentration of metabolites in *C. elegans*, the sample number is low and further experiments are indeed required to confirm the *in vivo* results.

7.6 Materials and methods

7.6.1 Fabrication of the micro-channel

The fabrication of the micro-channel was carried out by collaborators at EMPA, Switzerland.

The micro-channels were fabricated via a two-photon polymerization technique using a high resolution 3D printer (Photonic Professional GT, Nanoscribe GmbH, Germany). This additive manufacturing technique provides a resolution better than 1 μm^3 in a more versatile manner compared to traditional microfabrication methods. The structures were patterned into IP-S photoresist, a negative tone cross-linking polymer proprietary to Nanoscribe GmbH, which is optically transparent and gives an extraordinary geometrical freedom in the design of the micro-channels. An indium tin oxide (ITO) coated glass slide served as a substrate. The refractive index difference between the two materials guaranteed a facilitated detection of the interface. For the release of the micro-channels,

a 500 nm-thick dextran layer (Sigma-Aldrich, US) was spin-coated onto the substrate. This sacrificial layer was subsequently dissolved in water, enabling the release of the structures at the end of the fabrication process. A 25× objective (LCI Plan-Neofluar 25/0.8 Imm Korr DIC M27, Zeiss, Germany) was used in direct immersion mode into the photoresist. The refractive indices of the objective and the photoresist were matched to enable high spatial resolution. The voxel diameter was determined by a preceding test exposure, and the results were fed into the modelling software which imports Solidworks STL files to generate machine specific data. Using the 25× objective and 50 m/s writing speed, the voxel size was about $0.3 \times 0.3 \times 2 \ \mu m^3$ (with a 63× objective the voxel size was about $0.15 \times 0.15 \times 0.45 \ \mu m^3$). A droplet of IP-S resist was placed onto the substrate, in which the objective was immersed. The objective was fixed in space, while the positioning of the substrate was given by the combination of galvanometric MEMS mirrors and a piezoelectric unit. In the xy plane, the galvanometric mirrors traveled within a 200 μm radius at each fixed piezo position. A slicing distance of 1 μm was defined to split the structure into equal distance horizontal planes which were set by the piezoelectric stage. This parameter was set to ensure proper overlapping and adhesion in between the horizontal planes. To decrease writing time, a scaffolding technique was implemented within the bulk volumes. A triangular support structure was used, with a 20 μm spacing between planes and a scaffolding wall thickness of 3 μm. The writing time for a single microfluidic structure was approximately 5 hours. To provide control over the resist-air interface, and to maintain mechanical resistance over an extended period of development, an 18 μm-thick outer shell was defined, which was patterned as a bulk area. The accessible area of the galvanometric mirror was limited by the beam deflection and it was confined in a 200 μm-radius circle. The block consisted of a volume that could be written at a single xy piezoelectric stage position, only by moving the galvanometric mirrors and the piezoelectric stage in the z direction. The block shape had hexagonal shape to optimize the volume accessible from the galvanometric mirror and to facilitate stitching by having large neighbouring block surfaces. The blocks were written in a consecutive manner: a piezoelectric stage xy position was chosen, which was exposed thanks to the synergy of the galvanometric mirrors and the piezoelectric z stage. Once the block writing was finished, the piezoelectric stage moved to the next, neighbouring position and restarted exposure as before. A block shear angle of 13° was used in the z direction to avoid a shadowing effect, which occurs at overlapping block edges due to increased exposure. A block overlap of 2.5 μm enhanced the stitching by reinforcing the adhesion between blocks. The block size was chosen to be $x = 220 \ \mu m$, $y = 190 \ \mu m$, $z = 250 \ \mu m$. Applying the shear angle and overlap, the total block dimension became $x = 259.5 \ \mu m$, $y = 259 \ \mu m$, $z = 250 \ \mu m$.

The laser power was 65 mW at the point of entering the objective. For writing the shell of the structure, the laser power was reduced to 42%. For the internal scaffolding, the laser power was increased to 50%, which increased the robustness at the cost of the spatial resolution. Following exposure, the objective was removed from the photoresist, and the substrate was placed into PGMEA (Sigma-Aldrich, US) for development. The

substrate was positioned in a way that the channels could stand vertically. A continuous stirring in the beaker enhanced the removal of developed photoresist residues from inside the channel. The development duration was typically 6 hours. Once development was finished, the substrate was immersed into isopropanol in an identical configuration for one hour. A second rinsing step, with ultra-high purity isopropanol (99.99 %) was performed over 30 minutes to further clean the inside of the channels. Finally, the substrate was left to naturally dry in vertical position.

7.6.2 *C. elegans* preparation and microfluidic operations

C. elegans wild type worms were cultured at 20 °C on NGM 90 mm Petri dishes seeded with *E. coli* strain OP50. Worms were provided by the Caenorhabditis Genetics Center (University of Minnesota). HT115 *E. coli* bacteria were grown in LB with 100 μg/mL ampicillin and 12.5 μg/mL tetracycline overnight in a thermal shaker at 37 °C. The following day, 50 μL of the confluent bacterial cultures were used to inoculate freshly prepared LB medium containing only ampicillin. The new cultures were grown until reaching an optical density between 0.6 and 0.8, and 90 μL were used for seeding the experimental plates.

The microfluidic chip and tubes were first filled with S medium using the fluidic setup described in Section 2.4. A worm of desired size was transferred, using a worm picker, from the agarose plate to an S medium reservoir, from which it was sucked up in a tube connected to the device. Afterwards, with a flow of 500 nL/s, the worm was injected in the microfluidic chip from the inlet. In order to insert the animal in the trapping channel, a flow of 1 μL/s was applied. Once trapped, a gentle flow of 50 nL/s of *E. coli* bacteria was used to replace the S medium in the chip and therefore provide nutrients to the worm through the lateral channels. Afterwards, the flow was stopped and the tubes clamped. The whole operation, and the following NMR experiments, were performed at 20 °C. Once the sample was trapped and the microfluidic chip was clamped, the device was moved and transferred under the setup described in Section 7.2.

7.7 Discussion and conclusion

In this Chapter, I described the implementation of a microsystem to perform NMR spectroscopy on *C. elegans* subsections. A microcoil integrated in a silicon chip previously described by [163] was used for NMR signal excitation/detection. The 0.2 nL-detection volume of the single chip detector required the sample to be immobilized and in close proximity to the microcoil. To answer to this requirement, a microfluidic device was designed, to load and hold a single adult *C. elegans* on the microcoil. The device featured a main channel, whose dimensions matched the size of an adult animal, and two lateral parallel micro-channels for the delivery of nutrients, necessary for the sample survival. The device was then fabricated by collaborators at EMPA, using a two-photon

119

polymerization technique by mean of a high resolution 3D printer, which provided a resolution better than 1 μm^3. Using this channel, the sample could be kept at a distance of about 10 μm from the microcoil surface. A robust fluidic interface was then fabricated by collaborators at the Laboratory of Microsystems 1, in order to connect the micro-channel with the microfluidic setup, guaranteeing a stable sealing over the entire NMR measurement. After the system was calibrated by measuring the NMR from pure water, we performed experiments on a *C. elegans* worm. The active area of the detector was covered by a subsection occupied by about eight eggs inside the adult. NMR peaks presumably corresponding to yolk lipids were found after 12 hours of measurements.

The results of the reported experiments indicate that the approach proposed here allows for the non-invasive and efficient handling and trapping of *C. elegans* for NMR investigations at the sub-nL volume scale, in conditions of high sensitivity and sample limited spectral resolution.

7.8   Future outlook

The obtained spin sensitivity of 2.5×10^{13} spin/Hz$^{1/2}$ allowed detecting highly concentrated endogenous compounds in the *C. elegans* subsection, at the cost of a relatively long experimental times. In order to perform measurements and capture possible age-related changes in the metabolic content of the animal, the spin sensitivity should be improved, to allow for shorter experimental times. To do so, one could either scale down the detector size to improve the filling factor, which, however, would make the sample positioning more challenging, or use a higher magnetic field. Typical age-related changes occur every 8-12 hours [75]: this timing requires a maximum measurement time of 3-4 hours. Moreover, if the *C. elegans* subsection contains embryos, a measurement time as short as 1 h should be achieved, as the average *in utero* embryonic development time lasts about 2.5 hours [50].

In order to increase the throughput of the NMR recordings, a new silicon chip including parallel independent microcoils, opportunely spaced to avoid any crosstalk, could be fabricated. Such array of coils would allow investigating the metabolic content in different subsections of the same individual or in the same subsection of different individuals.

8 Conclusions and outlook

Despite being an invertebrate that lacks many vital organs and a circulatory system, *C. elegans* is a powerful tool for drug testing and for the understanding of the molecular and genetic mechanisms underlying several human diseases. Its ability to mimic human disease and disease pathways offers higher chances of identifying drugs that will ultimately be more efficacious in humans, and cannot be reproduced in *in-vitro* or cellular-based models. Moreover, the availability of genetic tools such as a RNAi feeding library can be exploited, to simplify the identification of drug targets.

Despite its low complexity, *C. elegans* offers a vast portfolio of measurable phenotypes: several physiological traits and behaviors can be measured, such as size, growth rate, feeding, locomotion, fertility, respiration rate, motility. In a drug screening scenario, *C. elegans* would make an excellent candidate for whole animal-based screening and would nicely feed the drug discovery pipeline, between cell-based assays and tests on rodents. The use of microfluidics would make such drug tests more efficient, standardized and cost-effective.

In Chapter 3, I showed a comprehensive microfluidic platform enabling the unprecedented *C. elegans* culture over its full life-cycle at the single-worm level while longitudinally monitoring multiple phenotypic markers upon a variety of treatments. In fact, the platform allowed testing pharmacological and genetic treatments by simply changing the compounds injected into the microfluidic chip, while ensuring reproducibility and perfect control of all the environmental parameters. This phenotyping strategy paves the way for the identification of appropriate disease biomarkers that would shape the worm response to the treatment of interest. The method was used to identify the phenotypic footprint and investigate the phenotypic variability associated with the nematode UPR^{mt}. In worms treated with doxycycline or treated with RNAi for *mrps-5* and *cco-1* to induce UPR^{mt}, I observed the typical phenotypic hallmarks of mitochondrial stress, such as delayed development, reduced size, reduced fertility and induction of the UPR^{mt} biomarker *hsp-6p::gfp*. On the other hand, NR did prolong the *C. elegans* life-cycle, without compromising either embryonal viability or worm fertility, and weakly activat-

ing the UPR^{mt}. Moreover, this phenotyping strategy revealed a treatment-dependent intrapopulation variability that could otherwise not be observed in RNAi experiments run on plates. In a personalized medicine perspective, the characterization of such intrapopulation treatment-dependent variability allows both characterizing the effectiveness of a treatment in a population subsets and identifying personalized follow-up treatments. In Chapter 4, I described a Doehlert design of experiments to characterize the effect of temperature, food amount and drug concentration on the worm development. A microfluidic chip enclosed in a custom-made thermal incubator was designed to culture *C. elegans* larvae with full control of the experimental parameters. Such a device allowed testing multiple conditions in parallel, reducing therefore the overall drug testing time. Only a limited number of well-designed experiments (13, in this case) was required to characterize the effectiveness of the drug, as well as the influence of all the considered experimental factors on the treatment outcome. According to the standard one-factor-at-a-time approach, to explore the full combinations of three factors, 105 experiments - instead of 13 - would have been necessary. Moreover, such a DoE approach revealed the drug effect even upon additional combinations of experimental factors, not limiting the study to the 13 tested conditions, maximizing in this way the knowledge of the process. Furthermore, this approach could provide information about second or higher order interactions among the factors, even if no significant interactions were shown in the experimental space chosen in this work. Finally, this testing strategy allowed identifying appropriate drug concentration and environmental conditions to obtain the desired experimental outcome.

In Chapter 5, I described a miniaturized opto-electronic platform integrated in a microfluidic device, which was able to measure the on-chip absorbance of planktonic bacteria in the 1-5 $\times$ 10^9 cell/mL concentration range, applying the Lambert-Beer's absorption principles. Compared to previous solutions, this platform made the quantification of bacterial concentration in an automated way, therefore less error-prone and time-consuming, as well as nearly noise- and fluctuation-free. Furthermore, the quantification of a bacterial concentration was here assured using a system of small commercial opto-electronical components that made the measurement affordable and the device portable. The system was able to measure the concentration of a bacterial sample, requiring a dead volume which is three orders of magnitude smaller than the volume required by most of the commercial spectrophotometers. Afterwards, envisioning long-term experiments, I used the customized platform to monitor the change of bacterial absorbance over 10 h. A concentration-dependent absorbance drop was observed after 1-2 hours. In order to explain this measurement, tailored experiments were performed, investigating the phenomena of bacterial settling and aggregation. Based on our observations, I hypothesized a simple mathematical model for the change of absorbance over time, according to which, bacterial settling and aggregation were the major players. Finally, our general-purpose device can be possibly put in fluidic connection with a separate microfluidic chip inoculated with bacteria of unknown concentration, in a modular fashion, with a negligible dead volume. Specifically, such a platform could be used to measure the concentration of the

bacterial solutions that are used to culture *C. elegans* worms in microfluidic environments, to properly control their feeding.

In Chapter 6, I described a simple yet powerful motility assay, to assess the drug effect at the behavioral level upon exposure of *C. elegans* YA worms to glucose and dynasore. A dedicated microfluidic device allowed delivering chemicals in a precise spatio-temporal way, which made the experimental protocol robust and reproducible. Moreover, fluidic flow profile and video recording were coupled in a synergistic fashion and the video-processing routine could segment and distinguish up to 10-12 animals swimming in the same microfluidic chamber. I validated this method by investigating *in vivo* the role of dynamin in glucose uptake in *C. elegans*, given that the insuline pathway is well-conserved from these nematodes to mammals. The role of dynamin in glucose uptake was observed first at the behavioral level by quantifying worms motility and than confirmed at the whole organism level with the quantitation of glucose in *C. elegans*, thus providing an extensive mapping of the role of dynamin. Quantification of worm motility upon exposure to drugs proved to be a powerful indicator of the molecule effect at the whole-organism level. This quantification could be extended to other time points beside YA stage and to more subtle phenotypes, e.g. body bends and swimming frequency.

Finally, in Chapter 7, I described the design of a micro-channel to accurately position and immobilize a single *C. elegans* to perform NMR measurements. The device was fabricated at EMPA, using a two-photon polymerization technique by mean of a high resolution 3D printer, which provided a resolution better than 1 μm^3. Using this channel, the sample could be kept at a distance of about 10 μm from the microcoil surface, inside the detection volume of the single chip detector. A robust fluidic interface was then fabricated to connect the micro-channel with the microfluidic setup, guaranteeing a stable sealing over the entire NMR measurement. After the system was calibrated by measuring the NMR from pure water, experiments were performed on a *C. elegans* worm, and NMR peaks presumably corresponding to yolk lipids were found after 12 hours of measurements.

Throughout this Thesis, I described different microfluidic-based phenotyping assays dedicated to the quantification of worms growth, length, fertility, survival, fluorescent expression of a gene of interest and motility. Ideally, these analyses could be easily integrated in a unique phenotyping platform, taking advantage of the modularity and versatility of each assay. In such a comprehensive phenotypic scenario, an exception is given by the metabolic phenotyping enabled by NMR, as it requires a dedicated chip and setup. However, NMR spectroscopy can be performed in a separate step. For example it could be useful to compare the metabolic content of *C. elegans* before and after the administration of a drug, to obtain complementary information about the drug effect.

In the drug discovery pipeline, testing several compounds on *C. elegans* using microfluidic-based phenotypic screenings, would allow approaching the follow-up tests on mammals with a more clear vision and higher probability of success.

To start, a DoE approach, where different doses of a compound are varied, would first

allow excluding those ineffective drugs that, regardless the dose, do not trigger any response in the nematode. At the same time, a working dose could be identified for the other compounds. The microfluidic platform that I described in Chapter 4 could be perfectly used for this purpose. If needed, a microfluidic chip featuring a higher number of channels and chambers could be used, to increase the throughput of the screening. Depending on the compound, the read-out of the assay could be the development time as well as size or motility, quantified either at the population level or at single-animal resolution or both.

In a second step, once the effective dose of a compound is identified, a high content phenotypic screening could be performed. The phenotyping strategy that I described in Chapter 3 would allow monitoring the response to the drug at a population level but also at single-animal resolution, if required by the assay. A single-worm-based readout, if coupled with appropriate clustering algorithms, would allow identifying a possible heterogeneous response to the drug, as demonstrated in Chapter 3. Clustering analyses as PCA would also allow isolating the most significant phenotypes, that could be worth investigating in follow-up experiments on rodents. Anyway, both in a single-animal- and in a population-based response, a sample number higher than 16 is recommended to increase the throughput of the assay, and can be achieved by fabricating a design with higher number of micro-chambers, capitalizing the modularity of the chip design.

Testing a significant number of compounds on *C. elegans* and extrapolating the most important phenotypic markers before investing in experiments on more complex animals, would allow narrowing the portfolio of molecules to test. Moreover, tests on *C. elegans* would provide a more precise idea of the molecule's mechanism of action and would ideally suggest which type of phenotypic readout should the follow-up preclinical experiment on rodent be addresses to. From an economical and business perspective, this translates in a reduced amount of *ad hoc* tests on animals, and eventually in a faster and less-costly animal testing phase. Finally, even if tests on animals are nowadays still impossible to replace with an equivalently-powerful and alternative model, *C. elegans* research, whenever able to reduce the use of higher-order animal, would be advantageous also from an ethical point of view.

Bibliography

[1]   S. Brenner, "The Genetics of Caenorhabditis Elegans", en, *Genetics*, vol. 77, no. 1, pp. 71–94, 1974.

[2]   L. Timmons and A. Fire, "Specific interference by ingested dsRNA", En, *Nature*, vol. 395, no. 6705, p. 854, 1998.

[3]   T. C. e. S. Consortium*, "Genome Sequence of the Nematode C. elegans: A Platform for Investigating Biology", en, *Science*, vol. 282, no. 5396, pp. 2012–2018, 1998.

[4]   X. Chen, J. W. Barclay, R. D. Burgoyne, and A. Morgan, "Using C. elegans to discover therapeutic compounds for ageing-associated neurodegenerative diseases", *Chem Cent J*, vol. 9, 2015.

[5]   J.-A. Lepesant, "The promises of neurodegenerative disease modeling", *Comptes Rendus Biologies*, Biologie et devenir technologique de l'homme / Biology and the technological future of man - Bruxelles, 9 et 10 octobre 2014 / Brussels, 9 and 10 October 2014, vol. 338, no. 8, pp. 584–592, 2015.

[6]   J. E. Sulston, E. Schierenberg, J. G. White, and J. N. Thomson, "The embryonic cell lineage of the nematode Caenorhabditis elegans", *Developmental Biology*, vol. 100, no. 1, pp. 64–119, 1983.

[7]   O. Hobert, "Neurogenesis in the nematode Caenorhabditis elegans", *WormBook*, 2010.

[8]   G. D. Coxon, C. B. Cooper, S. H. Gillespie, and T. D. McHugh, "Strategies and challenges involved in the discovery of new chemical entities during early-stage tuberculosis drug discovery", eng, *J. Infect. Dis.*, vol. 205 Suppl 2, S258–264, 2012.

[9]   M. Cornaglia, T. Lehnert, and M. A. M. Gijs, "Microfluidic systems for high-throughput and high-content screening using the nematode Caenorhabditis elegans", en, *Lab Chip*, vol. 17, no. 22, pp. 3736–3759, 2017.

[10] T. Denayer, T. Stöhr, and M. Van Roy, "Animal models in translational medicine: Validation and prediction", *New Horizons in Translational Medicine*, vol. 2, no. 1, pp. 5–11, 2014.

Bibliography

[11] L. P. O'Reilly, C. J. Luke, D. H. Perlmutter, G. A. Silverman, and S. C. Pak, "C. elegans in high-throughput drug discovery", *Advanced Drug Delivery Reviews*, Innovative tissue models for drug discovery and development, vol. 69-70, no. Supplement C, pp. 247–253, 2014.

[12] K. Strange, "Drug Discovery in Fish, Flies, and Worms", *ILAR J*, vol. 57, no. 2, pp. 133–143, 2016.

[13] T. Stiernagle, "Maintenance of C. elegans", *WormBook*, 2006.

[14] T. C. Y. Kwok, N. Ricker, R. Fraser, A. W. Chan, A. Burns, E. F. Stanley, P. McCourt, S. R. Cutler, and P. J. Roy, "A small-molecule screen in *C. elegans* yields a new calcium channel antagonist", En, *Nature*, vol. 441, no. 7089, p. 91, 2006.

[15] B. Lehner, J. Tischler, and A. G. Fraser, "RNAi screens in *Caenorhabditis elegans* in a 96-well liquid format and their application to the systematic identification of genetic interactions", En, *Nature Protocols*, vol. 1, no. 3, p. 1617, 2006.

[16] S. Gosai, *Automated High-Content Live Animal Drug Screening Using C. elegans Expressing the Aggregation Prone Serpin 1-antitrypsin Z*, 2010.

[17] A. G. Fernandez, E. K. Mis, B. O. Bargmann, K. D. Birnbaum, and F. Piano, "Automated sorting of live C. elegans using laFACS", *Nat Methods*, vol. 7, no. 6, pp. 417–418, 2010.

[18] C. K. Leung, Y. Wang, S. Malany, A. Deonarine, K. Nguyen, S. Vasile, and K. P. Choe, "An Ultra High-Throughput, Whole-Animal Screen for Small Molecule Modulators of a Specific Genetic Pathway in Caenorhabditis elegans", *PLOS ONE*, vol. 8, no. 4, e62166, 2013.

[19] B. P. Gupta and P. Rezai, "Microfluidic Approaches for Manipulating, Imaging, and Screening C. elegans", en, *Micromachines*, vol. 7, no. 7, p. 123, 2016.

[20] V. Sivagnanam and M. A. M. Gijs, "Exploring Living Multicellular Organisms, Organs, and Tissues Using Microfluidic Systems", *Chem. Rev.*, vol. 113, no. 5, pp. 3214–3247, 2013.

[21] A. Ben-Yakar, N. Chronis, and H. Lu, "Microfluidics for the analysis of behavior, nerve regeneration, and neural cell biology in C. elegans", *Curr Opin Neurobiol*, vol. 19, no. 5, pp. 561–567, 2009.

[22] X. Ai, W. Zhuo, Q. Liang, P. T. McGrath, and H. Lu, "A high-throughput device for size based separation of C. elegans developmental stages", en, *Lab Chip*, vol. 14, no. 10, pp. 1746–1752, 2014.

[23] K. Chung, *Automated on-chip rapid microscopy, phenotyping and sorting of C. elegans | Nature Methods*, 2008.

[24] N. A. Bakhtina and J. G. Korvink, "Microfluidic laboratories for C. elegans enhance fundamental studies in biology", en, *RSC Adv.*, vol. 4, no. 9, pp. 4691–4709, 2013.

[25] K. Chung, M. Zhan, J. Srinivasan, P. W. Sternberg, E. Gong, F. C. Schroeder, and H. Lu, "Microfluidic chamber arrays for whole-organism behavior-based chemical screening", en, vol. 11, no. 21, pp. 3689–3697, 2011.

[26] A. San-Miguel and H. Lu, "Microfluidics as a tool for C. elegans research", *WormBook*, pp. 1–19, 2013.

[27] Henrik Bruus, *Theoretical Microfluidics*, ser. Oxford Master Series in Physics 18. 2007.

[28] E. K. Sackmann, A. L. Fulton, and D. J. Beebe, "The present and future role of microfluidics in biomedical research", En, *Nature*, vol. 507, no. 7491, p. 181, 2014.

[29] T. Watanabe, F. Sassa, Y. Yoshizumi, and H. Suzuki, "Review of Microfluidic Devices for On-Chip Chemical Sensing", en, *Electron Comm Jpn*, vol. 100, no. 4, pp. 25–32, 2017.

[30] E. Samiei, M. Tabrizian, and M. Hoorfar, "A review of digital microfluidics as portable platforms for lab-on a-chip applications", en, *Lab Chip*, vol. 16, no. 13, pp. 2376–2396, 2016.

[31] H. Yang and M. A. M. Gijs, "Micro-optics for microfluidic analytical applications", en, *Chem. Soc. Rev.*, 2018.

[32] S. Gavrilakis, "Numerical simulation of low-Reynolds-number turbulent flow through a straight square duct", en, *Journal of Fluid Mechanics*, vol. 244, pp. 101–129, 1992.

[33] B. Eckhardt, T. M. Schneider, B. Hof, and J. Westerweel, "Turbulence Transition in Pipe Flow", *Annual Review of Fluid Mechanics*, vol. 39, no. 1, pp. 447–468, 2007.

[34] D. J. Beebe, G. A. Mensing, and a. G. M. Walker, "Physics and Applications of Microfluidics in Biology", *Annual Review of Biomedical Engineering*, vol. 4, no. 1, pp. 261–286, 2002.

[35] N. A. Polson and M. A. Hayes, "Microfluidics: controlling fluids in small places", eng, *Anal. Chem.*, vol. 73, no. 11, 312A–319A, 2001.

[36] C. Zhang, D. Xing, and Y. Li, "Micropumps, microvalves, and micromixers within PCR microfluidic chips: Advances and trends", *Biotechnology Advances*, vol. 25, no. 5, pp. 483–514, 2007.

[37] R. F. Ismagilov, A. D. Stroock, P. J. A. Kenis, G. Whitesides, and H. A. Stone, "Experimental and theoretical scaling laws for transverse diffusive broadening in two-phase laminar flows in microchannels", *Appl. Phys. Lett.*, vol. 76, no. 17, pp. 2376–2378, 2000.

[38] C.-P. Jen, C.-Y. Wu, Y.-C. Lin, and C.-Y. Wu, "Design and simulation of the micromixer with chaotic advection in twisted microchannels", en, *Lab Chip*, vol. 3, no. 2, pp. 77–81, 2003.

[39] Y. Xia and G. M. Whitesides, "Soft Lithography", en, *Angewandte Chemie International Edition*, vol. 37, no. 5, pp. 550–575, 1998.

[40] N. J. Schork, "Personalized medicine: Time for one-person trials", *Nature News*, vol. 520, no. 7549, p. 609, 2015.

[41] P. Song, R. Hu, D. J. H. Tng, and K.-T. Yong, "Moving towards individualized medicine with microfluidics technology", en, *RSC Adv.*, vol. 4, no. 22, pp. 11 499–11 511, 2014.

[42] E. Shapiro, T. Biezuner, and S. Linnarsson, "Single-cell sequencing-based technologies will revolutionize whole-organism science", en, *Nat Rev Genet*, vol. 14, no. 9, pp. 618–630, 2013.

[43] M. Muthaiyan Shanmugam and T. Subhra Santra, "Microfluidic Devices in Advanced Caenorhabditis elegans Research", ENG, *Molecules*, vol. 21, no. 8, 2016.

[44] J. Durieux, S. Wolff, and A. Dillin, "The Cell-Non-Autonomous Nature of Electron Transport Chain-Mediated Longevity", English, *Cell*, vol. 144, no. 1, pp. 79–91, 2011.

[45] V. Jovaisaite, L. Mouchiroud, and J. Auwerx, "The mitochondrial unfolded protein response, a conserved stress response pathway with implications in health and disease", ENG, *J. Exp. Biol.*, vol. 217, no. Pt 1, pp. 137–143, 2014.

[46] Y.-F. Lin and C. M. Haynes, "Metabolism and the UPR(mt)", ENG, *Mol. Cell*, vol. 61, no. 5, pp. 677–682, 2016.

[47] M. Cornaglia, L. Mouchiroud, A. Marette, S. Narasimhan, T. Lehnert, V. Jovaisaite, J. Auwerx, and M. A. M. Gijs, "An automated microfluidic platform for C. elegans embryo arraying, phenotyping, and long-term live imaging", *Scientific Reports*, vol. 5, p. 10 192, 2015.

[48] W.-H. Tan and S. Takeuchi, "A trap-and-release integrated microfluidic system for dynamic microarray applications", en, *PNAS*, vol. 104, no. 4, pp. 1146–1151, 2007.

[49] R. C. Cassada and R. L. Russell, "The dauerlarva, a post-embryonic developmental variant of the nematode Caenorhabditis elegans", eng, *Dev. Biol.*, vol. 46, no. 2, pp. 326–342, 1975.

[50] E. Schierenberg, "Embryological variation during nematode development", *WormBook*, 2006.

[51] R. H. Houtkooper, L. Mouchiroud, D. Ryu, N. Moullan, E. Katsyuba, G. Knott, R. W. Williams, and J. Auwerx, "Mitonuclear protein imbalance as a conserved longevity mechanism", en, *Nature*, vol. 497, no. 7450, pp. 451–457, 2013.

[52] A. M. Nargund, M. W. Pellegrino, C. J. Fiorese, B. M. Baker, and C. M. Haynes, "Mitochondrial import efficiency of ATFS-1 regulates mitochondrial UPR activation", ENG, *Science*, vol. 337, no. 6094, pp. 587–590, 2012.

[53] P. A. Andreux, R. H. Houtkooper, and J. Auwerx, "Pharmacological approaches to restore mitochondrial function", en, *Nat Rev Drug Discov*, vol. 12, no. 6, pp. 465–483, 2013.

[54] N. Moullan, L. Mouchiroud, X. Wang, D. Ryu, E. G. Williams, A. Mottis, V. Jovaisaite, M. V. Frochaux, P. M. Quiros, B. Deplancke, R. H. Houtkooper, and J. Auwerx, "Tetracyclines Disturb Mitochondrial Function across Eukaryotic Models: A Call for Caution in Biomedical Research", English, *Cell Reports*, vol. 10, no. 10, pp. 1681–1691, 2015.

[55] C. M. Haynes, Y. Yang, S. P. Blais, T. A. Neubert, and D. Ron, "The matrix peptide exporter HAF-1 signals a mitochondrial UPR by activating the transcription factor ZC376.7 in C. elegans", eng, *Mol. Cell*, vol. 37, no. 4, pp. 529–540, 2010.

[56] T. Yoneda, C. Benedetti, F. Urano, S. G. Clark, H. P. Harding, and D. Ron, "Compartment-specific perturbation of protein handling activates genes encoding mitochondrial chaperones", en, *Journal of Cell Science*, vol. 117, no. 18, pp. 4055–4066, 2004.

[57] A. K. Corsi, B. Wightman, and M. Chalfie, "A Transparent Window into Biology: A Primer on Caenorhabditis elegans", en, *Genetics*, vol. 200, no. 2, pp. 387–407, 2015.

[58] C. Cantó, K. J. Menzies, and J. Auwerx, "NAD+ Metabolism and the Control of Energy Homeostasis: A Balancing Act between Mitochondria and the Nucleus", *Cell Metabolism*, vol. 22, no. 1, pp. 31–53, 2015.

[59] L. Mouchiroud, R. H. Houtkooper, N. Moullan, E. Katsyuba, D. Ryu, C. Cantó, A. Mottis, Y.-S. Jo, M. Viswanathan, K. Schoonjans, L. Guarente, and J. Auwerx, "The NAD+/Sirtuin Pathway Modulates Longevity through Activation of Mitochondrial UPR and FOXO Signaling", *Cell*, vol. 154, no. 2, pp. 430–441, 2013.

[60] L. Avery, "The genetics of feeding in Caenorhabditis elegans", eng, *Genetics*, vol. 133, no. 4, pp. 897–917, 1993.

[61] C. M. Haynes, K. Petrova, C. Benedetti, Y. Yang, and D. Ron, "ClpP mediates activation of a mitochondrial unfolded protein response in C. elegans", eng, *Dev. Cell*, vol. 13, no. 4, pp. 467–480, 2007.

[62] A. Dillin, A.-L. Hsu, N. Arantes-Oliveira, J. Lehrer-Graiwer, H. Hsin, A. G. Fraser, R. S. Kamath, J. Ahringer, and C. Kenyon, "Rates of Behavior and Aging Specified by Mitochondrial Function During Development", en, *Science*, vol. 298, no. 5602, pp. 2398–2401, 2002.

[63] W. Y. Tsang and B. D. Lemire, "Mitochondrial Genome Content Is Regulated during Nematode Development", *Biochemical and Biophysical Research Communications*, vol. 291, no. 1, pp. 8–16, 2002.

Bibliography

[64] W. B. Wood, J. Sulston, and J. Hodgkin, *The Nematode Caenorhabditis elegans*, University of Colorado, Boulder, ser. Cold Spring Harbor Monograph Series. Boulder, University of Colorado: Cold Spring Harbor Laboratory, 1988.

[65] Ross C. Wilson and Jennifer A. Doudna, "Molecular Mechanisms of RNA Interference | Annual Review of Biophysics", *Annual review of biophysics*, vol. 42, 2013.

[66] N. Gritti, S. Kienle, O. Filina, and J. S. van Zon, "Long-term time-lapse microscopy of C. elegans post-embryonic development", *Nature Communications*, vol. 7, p. 12 500, 2016.

[67] S. Mondal, E. Hegarty, C. Martin, S. K. Gökçe, N. Ghorashian, and A. Ben-Yakar, "Large-scale microfluidics providing high-resolution and high-throughput screening of Caenorhabditis elegans poly-glutamine aggregation model", en, *Nature Communications*, vol. 7, p. 13 023, 2016.

[68] E. G. Williams and J. Auwerx, "The Convergence of Systems and Reductionist Approaches in Complex Trait Analysis", ENG, *Cell*, vol. 162, no. 1, pp. 23–32, 2015.

[69] R. Herman, "Introduction to sex determination", *WormBook*, 2005.

[70] S. M. Paul, D. S. Mytelka, C. T. Dunwiddie, C. C. Persinger, B. H. Munos, S. R. Lindborg, and A. L. Schacht, "How to improve R&D productivity: the pharmaceutical industry's grand challenge", en, *Nat Rev Drug Discov*, vol. 9, no. 3, pp. 203–214, 2010.

[71] L. X. Yu, G. Amidon, M. A. Khan, S. W. Hoag, J. Polli, G. K. Raju, and J. Woodcock, "Understanding Pharmaceutical Quality by Design", en, *AAPS J*, vol. 16, no. 4, pp. 771–783, 2014.

[72] European Medicines Agency, *ICH guideline Q8 (R2) on pharmaceutical development - Step 5*, 2017.

[73] Stavros N. Politis, Paolo Colombo, Gaia Colombo, and Dimitrios M. Rekkas, "Design of experiments (DoE) in pharmaceuticaldevelopment", *Drug Development and Industrial Pharmacy*, vol. 43, no. 6, pp. 889–901, 2017.

[74] R. Trouillon, M. C. Letizia, K. J. Menzies, L. Mouchiroud, J. Auwerx, K. Schoonjans, and M. A. M. Gijs, "A multiscale study of the role of dynamin in the regulation of glucose uptake", en, *Integr. Biol.*, vol. 9, no. 10, pp. 810–819, 2017.

[75] J. J. Collins, C. Huang, S. Hughes, and K. Kornfeld, "The measurement and analysis of age-related changes in Caenorhabditis elegans", eng, *WormBook*, pp. 1–21, 2008.

[76] M. Gossen and H. Bujard, "Tight control of gene expression in mammalian cells by tetracycline-responsive promoters.", en, *PNAS*, vol. 89, no. 12, pp. 5547–5551, 1992.

[77] W. Y. Tsang, L. C. Sayles, L. I. Grad, D. B. Pilgrim, and B. D. Lemire, "Mitochondrial Respiratory Chain Deficiency inCaenorhabditis elegans Results in Developmental Arrest and Increased Life Span", en, *J. Biol. Chem.*, vol. 276, no. 34, pp. 32 240–32 246, 2001.

[78] M. Cornaglia, G. Krishnamani, L. Mouchiroud, V. Sorrentino, T. Lehnert, J. Auwerx, and M. A. M. Gijs, "Automated longitudinal monitoring of in vivo protein aggregation in neurodegenerative disease C. elegans models", *Mol Neurodegener*, vol. 11, 2016.

[79] C. J. Kenyon, "The genetics of ageing", en, *Nature*, vol. 464, no. 7288, pp. 504–512, 2010.

[80] L. Fontana and L. Partridge, "Promoting Health and Longevity through Diet: From Model Organisms to Humans", *Cell*, vol. 161, no. 1, pp. 106–118, 2015.

[81] G. Walker, K. Houthoofd, J. R. Vanfleteren, and D. Gems, "Dietary restriction in C. elegans: from rate-of-living effects to nutrient sensing pathways", eng, *Mech. Ageing Dev.*, vol. 126, no. 9, pp. 929–937, 2005.

[82] D. Gems and D. L. Riddle, "Genetic, behavioral and environmental determinants of male longevity in Caenorhabditis elegans", eng, *Genetics*, vol. 154, no. 4, pp. 1597–1610, 2000.

[83] D. Garigan, A.-L. Hsu, A. G. Fraser, R. S. Kamath, J. Ahringer, and C. Kenyon, "Genetic analysis of tissue aging in Caenorhabditis elegans: a role for heat-shock factor and bacterial proliferation", eng, *Genetics*, vol. 161, no. 3, pp. 1101–1112, 2002.

[84] L. Fontana, L. Partridge, and V. D. Longo, "Extending healthy life span–from yeast to humans", eng, *Science*, vol. 328, no. 5976, pp. 321–326, 2010.

[85] M. Ailion and J. H. Thomas, "Dauer formation induced by high temperatures in Caenorhabditis elegans.", *Genetics*, vol. 156, no. 3, pp. 1047–1067, 2000.

[86] P. J. Hu, "Dauer", *WormBook*, 2007.

[87] J. G. Ziegler and N. B. Nichols, "Optimum Settings for Automatic Controllers", *J. Dyn. Sys., Meas., Control*, vol. 115, no. 2B, pp. 220–222, 1993.

[88] C. Beloin, A. Roux, and J.-M. Ghigo, "Escherichia coli biofilms", *Curr Top Microbiol Immunol*, vol. 322, pp. 249–289, 2008.

[89] L. A. Pratt and R. Kolter, "Genetic analysis of Escherichia coli biofilm formation: roles of flagella, motility, chemotaxis and type I pili", eng, *Mol. Microbiol.*, vol. 30, no. 2, pp. 285–293, 1998.

[90] B. K. Swan, B. Tupper, A. Sczyrba, F. M. Lauro, M. Martinez-Garcia, J. M. González, H. Luo, J. J. Wright, Z. C. Landry, N. W. Hanson, B. P. Thompson, N. J. Poulton, P. Schwientek, S. G. Acinas, S. J. Giovannoni, M. A. Moran, S. J. Hallam, R. Cavicchioli, T. Woyke, and R. Stepanauskas, "Prevalent genome streamlining and latitudinal divergence of planktonic bacteria in the surface ocean", en, *PNAS*, vol. 110, no. 28, pp. 11 463–11 468, 2013.

[91] S. Sretenovic, B. Stojković, I. Dogsa, R. Kostanjšek, I. Poberaj, and D. Stopar, "An early mechanical coupling of planktonic bacteria in dilute suspensions", *Nat Commun*, vol. 8, 2017.

[92] H. C. Berg, "Motile Behavior of Bacteria", en, *Physics Today*, vol. 53, no. 1, p. 24, 2000.

[93] Howard Berg, *E. coli in Motion*. Springer Science & Business Media, 2004.

[94] M. J. Kim and K. S. Breuer, "Enhanced diffusion due to motile bacteria", *Physics of Fluids*, vol. 16, no. 9, pp. L78–L81, 2004.

[95] J. R. Taylor and R. Stocker, "Trade-Offs of Chemotactic Foraging in Turbulent Water", en, *Science*, vol. 338, no. 6107, pp. 675–679, 2012.

[96] J. T. Locsei and T. J. Pedley, "Run and Tumble Chemotaxis in a Shear Flow: The Effect of Temporal Comparisons, Persistence, Rotational Diffusion, and Cell Shape", en, *Bull. Math. Biol.*, vol. 71, no. 5, pp. 1089–1116, 2009.

[97] Paul Frymier and Roseanne Ford, "Analysis of bacterial swimming speed approaching a solid–liquid interface", vol. 43, no. 5, pp. 1341–1347, 1997.

[98] E. Lauga, W. R. DiLuzio, G. M. Whitesides, and H. A. Stone, "Swimming in Circles: Motion of Bacteria near Solid Boundaries", *Biophysical Journal*, vol. 90, no. 2, pp. 400–412, 2006.

[99] M. A.-S. Vigeant, R. M. Ford, M. Wagner, and L. K. Tamm, "Reversible and Irreversible Adhesion of Motile Escherichia coli Cells Analyzed by Total Internal Reflection Aqueous Fluorescence Microscopy", en, *Appl. Environ. Microbiol.*, vol. 68, no. 6, pp. 2794–2801, 2002.

[100] Melissa Miller and Bonnie Bassler, "Quorum Sensing in Bacteria", vol. 55, pp. 165–199, 2011.

[101] Z. Golkar, O. Bagasra, and D. G. Pace, "Bacteriophage therapy: a potential solution for the antibiotic resistance crisis", eng, *J Infect Dev Ctries*, vol. 8, no. 2, pp. 129–136, 2014.

[102] S. Sengupta, M. K. Chattopadhyay, and H.-P. Grossart, "The multifaceted roles of antibiotics and antibiotic resistance in nature", eng, *Front Microbiol*, vol. 4, p. 47, 2013.

[103] R. Rusconi, M. Garren, and R. Stocker, "Microfluidics Expanding the Frontiers of Microbial Ecology", *Annu Rev Biophys*, vol. 43, pp. 65–91, 2014.

[104] T. Ahmed, T. S. Shimizu, and R. Stocker, "Microfluidics for bacterial chemotaxis", en, *Integr. Biol.*, vol. 2, no. 11-12, pp. 604–629, 2010.

[105] Marcos and R. Stocker, "Microorganisms in vortices: a microfluidic setup", en, *Limnol. Oceanogr. Methods*, vol. 4, no. 10, pp. 392–398, 2006.

[106] Marcos, H. C. Fu, T. R. Powers, and R. Stocker, "Bacterial rheotaxis", en, *PNAS*, vol. 109, no. 13, pp. 4780–4785, 2012.

[107] S. Lecuyer, R. Rusconi, Y. Shen, A. Forsyth, H. Vlamakis, R. Kolter, and H. A. Stone, "Shear Stress Increases the Residence Time of Adhesion of Pseudomonas aeruginosa", *Biophysical Journal*, vol. 100, no. 2, pp. 341–350, 2011.

[108] K. Anselme, P. Davidson, A. M. Popa, M. Giazzon, M. Liley, and L. Ploux, "The interaction of cells and bacteria with surfaces structured at the nanometre scale", *Acta Biomaterialia*, vol. 6, no. 10, pp. 3824–3846, 2010.

[109] A. I. Hochbaum and J. Aizenberg, "Bacteria Pattern Spontaneously on Periodic Nanostructure Arrays", *Nano Lett.*, vol. 10, no. 9, pp. 3717–3721, 2010.

[110] A. Groisman, C. Lobo, H. Cho, J. K. Campbell, Y. S. Dufour, A. M. Stevens, and A. Levchenko, "A microfluidic chemostat for experiments with bacterial and yeast cells", en, *Nat Meth*, vol. 2, no. 9, pp. 685–689, 2005.

[111] F. K. Balagaddé, L. You, C. L. Hansen, F. H. Arnold, and S. R. Quake, "Long-term monitoring of bacteria undergoing programmed population control in a microchemostat", eng, *Science*, vol. 309, no. 5731, pp. 137–140, 2005.

[112] M. Gan, J. Su, J. Wang, H. Wu, and L. Chen, "A scalable microfluidic chip for bacterial suspension culture", en, *Lab Chip*, vol. 11, no. 23, pp. 4087–4092, 2011.

[113] M. Carminati, M. Giacometti, M. Sampietro, S. Chiodini, T. Doles, and G. Ferrari, "Parallelizable Microfluidic Resistive On-Line Detector of Micrometric Aggregates of Biopharmaceutical Antibodies", *Procedia Engineering*, Proceedings of the 30th anniversary Eurosensors Conference – Eurosensors 2016, 4-7. Sepember 2016, Budapest, Hungary, vol. 168, pp. 1438–1441, 2016.

[114] Y. Song, H. Zhang, C. H. Chon, S. Chen, X. Pan, and D. Li, "Counting bacteria on a microfluidic chip", *Analytica Chimica Acta*, vol. 681, no. 1, pp. 82–86, 2010.

[115] H. Y. Ha, Y. S. Park, D. K. Park, F. I. Uba, S. A. Soper, and Y. K. Cho, "Digital counting of bacteria by using a microfluidic chip with built-in electrodes", English (US), Chemical and Biological Microsystems Society, 2014.

[116] N. Yamaguchi, M. Torii, Y. Uebayashi, and M. Nasu, "Rapid, Semiautomated Quantification of Bacterial Cells in Freshwater by Using a Microfluidic Device for On-Chip Staining and Counting", en, *Appl. Environ. Microbiol.*, vol. 77, no. 4, pp. 1536–1539, 2011.

[117] Y. Yawata, J. Nguyen, R. Stocker, and R. Rusconi, "Microfluidic Studies of Biofilm Formation in Dynamic Environments", en, *J. Bacteriol.*, vol. 198, no. 19, pp. 2589–2595, 2016.

[118] S. Jakiela, T. S. Kaminski, O. Cybulski, D. B. Weibel, and P. Garstecki, "Bacterial Growth and Adaptation in Microdroplet Chemostats", en, *Angew. Chem. Int. Ed.*, vol. 52, no. 34, pp. 8908–8911, 2013.

[119] J. H. Jung and J. E. Lee, "Real-time bacterial microcolony counting using on-chip microscopy", En, *Scientific Reports*, vol. 6, p. 21 473, 2016.

[120] M. T. Meyer, V. Roy, W. E. Bentley, and R. Ghodssi, "Development and validation of a microfluidic reactor for biofilm monitoring via optical methods", en, *J. Micromech. Microeng.*, vol. 21, no. 5, p. 054 023, 2011.

[121] Y. W. Kim, M. P. Mosteller, S. Subramanian, M. T. Meyer, W. E. Bentley, and R. Ghodssi, "An optical microfluidic platform for spatiotemporal biofilm treatment monitoring", en, *J. Micromech. Microeng.*, vol. 26, no. 1, p. 015 013, 2016.

[122] J. Kiefer, N. Ebel, E. Schlücker, and A. Leipertz, "Characterization of Escherichia coli suspensions using UV/Vis/NIR absorption spectroscopy", en, *Anal. Methods*, vol. 2, no. 2, pp. 123–128, 2010.

[123] S. Yazdi and A. M. Ardekani, "Bacterial aggregation and biofilm formation in a vortical flow", *Biomicrofluidics*, vol. 6, no. 4, 2012.

[124] J. Wan, T. K. Tokunaga, and C.-F. Tsang, "Bacterial Sedimentation Through a Porous Medium", en, *Water Resour. Res.*, vol. 31, no. 7, pp. 1627–1636, 1995.

[125] G. Zaccanti and P. Bruscaglioni, "Deviation from the Lambert-Beer Law in the Transmittance of a Light Beam Through Diffusing Media: Experimental Results", *Journal of Modern Optics*, vol. 35, no. 2, pp. 229–242, 1988.

[126] V. P. Dick, "Applicability limits of Beer's law for dispersion media with a high concentration of particles", EN, *Appl. Opt., AO*, vol. 37, no. 21, pp. 4998–5004, 1998.

[127] S. D. Buckingham, F. A. Partridge, and D. B. Sattelle, "Automated, high-throughput, motility analysis in Caenorhabditis elegans and parasitic nematodes: Applications in the search for new anthelmintics", *International Journal for Parasitology: Drugs and Drug Resistance*, Includes articles from two meetings: "Anthelmintics: From Discovery to Resistance", pp. 218–315, and "Global Challenges for New Drug Discovery Against Tropical Parasitic Diseases", pp. 316–357, vol. 4, no. 3, pp. 226–232, 2014.

[128] S. J. Husson, "Keeping track of worm trackers", *WormBook*, pp. 1–17, 2012.

[129] T. R. Jones, A. E. Carpenter, M. R. Lamprecht, J. Moffat, S. J. Silver, J. K. Grenier, A. B. Castoreno, U. S. Eggert, D. E. Root, P. Golland, and D. M. Sabatini, "Scoring diverse cellular morphologies in image-based screens with iterative feedback and machine learning", en, *PNAS*, vol. 106, no. 6, pp. 1826–1831, 2009.

[130] C. Wahlby, L. Kamentsy, and A. E. C. Lamprecht, "An image analysis toolbox for high-throughput C. elegans assays | Nature Methods", en, *natmeth*, no. 10, 2013.

[131] D. Ramot, B. E. Johnson, T. L. B. Jr, L. Carnell, and M. B. Goodman, "The Parallel Worm Tracker: A Platform for Measuring Average Speed and Drug-Induced Paralysis in Nematodes", *PLOS ONE*, vol. 3, no. 5, e2208, 2008.

[132] G. D. Tsibidis and N. Tavernarakis, "Nemo: a computational tool for analyzing nematode locomotion", *BMC Neuroscience*, vol. 8, p. 86, 2007.

[133] N. A. Swierczek, A. C. Giles, C. H. Rankin, and R. A. Kerr, "High-throughput behavioral analysis in *C. elegans*", En, *Nature Methods*, vol. 8, no. 7, p. 592, 2011.

[134] P. Krajacic, X. Shen, P. K. Purohit, P. Arratia, and T. Lamitina, "Biomechanical Profiling of Caenorhabditis elegans Motility", *Genetics*, vol. 191, no. 3, pp. 1015–1021, 2012.

[135] M. Zheng, O. Gorelenkova, J. Yang, and Z. Feng, "A liquid phase based C. elegans behavioral analysis system identifies motor activity loss in a nematode Parkinson's disease model", *Journal of Neuroscience Methods*, vol. 204, no. 2, pp. 234–237, 2012.

[136] S. D. Buckingham and D. B. Sattelle, "Fast, automated measurement of nematode swimming (thrashing) without morphometry", *BMC Neuroscience*, vol. 10, p. 84, 2009.

[137] L. Mouchiroud, V. Sorrentino, E. G. Williams, M. Cornaglia, M. V. Frochaux, T. Lin, A. A. Nicolet-dit-Félix, G. Krishnamani, T. Ouhmad, M. A. Gijs, B. Deplancke, and J. Auwerx, "The Movement Tracker: A Flexible System for Automated Movement Analysis in Invertebrate Model Organisms", en, *Current Protocols in Neuroscience*, 2016, DOI: 10.1002/cpns.17.

[138] R. Trouillon and A. G. Ewing, "Amperometric Measurements at Cells Support a Role for Dynamin in the Dilation of the Fusion Pore during Exocytosis", en, *ChemPhysChem*, vol. 14, no. 10, pp. 2295–2301, 2013.

[139] J. Stöckli, D. J. Fazakerley, and D. E. James, "GLUT4 exocytosis", eng, *J. Cell. Sci.*, vol. 124, no. Pt 24, pp. 4147–4159, 2011.

[140] S. Huang and M. P. Czech, "The GLUT4 Glucose Transporter", *Cell Metabolism*, vol. 5, no. 4, pp. 237–252, 2007.

[141] G. J. K. Praefcke and H. T. McMahon, "The dynamin superfamily: universal membrane tubulation and fission molecules?", eng, *Nat. Rev. Mol. Cell Biol.*, vol. 5, no. 2, pp. 133–147, 2004.

[142] A. Anantharam, D. Axelrod, and R. W. Holz, "Real-time imaging of plasma membrane deformations reveals pre-fusion membrane curvature changes and a role for dynamin in the regulation of fusion pore expansion", *J Neurochem*, vol. 122, no. 4, pp. 661–671, 2012.

Bibliography

[143] E. Macia, M. Ehrlich, R. Massol, E. Boucrot, C. Brunner, and T. Kirchhausen, "Dynasore, a Cell-Permeable Inhibitor of Dynamin", *Developmental Cell*, vol. 10, no. 6, pp. 839–850, 2006.

[144] S.-J. Lee, C. T. Murphy, and C. Kenyon, "Glucose shortens the life span of C. elegans by downregulating DAF-16/FOXO activity and aquaporin gene expression", eng, *Cell Metab.*, vol. 10, no. 5, pp. 379–391, 2009.

[145] A. Schlotterer, G. Kukudov, F. Bozorgmehr, H. Hutter, X. Du, D. Oikonomou, Y. Ibrahim, F. Pfisterer, N. Rabbani, P. Thornalley, A. Sayed, T. Fleming, P. Humpert, V. Schwenger, M. Zeier, A. Hamann, D. Stern, M. Brownlee, A. Bierhaus, P. Nawroth, and M. Morcos, "C. elegans as Model for the Study of High Glucose–Mediated Life Span Reduction", *Diabetes*, vol. 58, no. 11, pp. 2450–2456, 2009.

[146] M. R. Liggett, M. J. Hoy, M. Mastroianni, and M. A. Mondoux, "High-glucose diets have sex-specific effects on aging in C. elegans: toxic to hermaphrodites but beneficial to males", *Aging (Albany NY)*, vol. 7, no. 6, pp. 383–387, 2015.

[147] T. Kasahara and M. Kasahara, "Characterization of rat Glut4 glucose transporter expressed in the yeast Saccharomyces cerevisiae: comparison with Glut1 glucose transporter1", *Biochimica et Biophysica Acta (BBA) - Biomembranes*, vol. 1324, no. 1, pp. 111–119, 1997.

[148] S. L. McMillin, D. L. Schmidt, B. B. Kahn, and C. A. Witczak, "GLUT4 Is Not Necessary for Overload-Induced Glucose Uptake or Hypertrophic Growth in Mouse Skeletal Muscle", eng, *Diabetes*, vol. 66, no. 6, pp. 1491–1500, 2017.

[149] E. Teshiba, K. Miyahara, and H. Takeya, "Glucose-induced abnormal egg-laying rate in Caenorhabditis elegans", *Bioscience, Biotechnology, and Biochemistry*, vol. 80, no. 7, pp. 1436–1439, 2016.

[150] E. Svensk, R. Devkota, M. Ståhlman, P. Ranji, M. Rauthan, F. Magnusson, S. Hammarsten, M. Johansson, J. Borén, and M. Pilon, "Caenorhabditis elegans PAQR-2 and IGLR-2 Protect against Glucose Toxicity by Modulating Membrane Lipid Composition", eng, *PLoS Genet.*, vol. 12, no. 4, e1005982, 2016.

[151] S. G. Clark, D.-L. Shurland, M. E. M., C. I. Bargmann, and A. M. van der Bliek, "A dynamin gtpase mutation causes a rapid and reversible temperature-inducible locomotion effect in c. elegans", *PNAS*, vol. 94, no. 19, pp. 10 438–43, 1997.

[152] A. Abragam, *Principles of Nuclear Magnetism*, English, ser. International series of monographs on physics. Oxford: Oxford university press, 1961, vol. 32.

[153] P. Callaghan, *Principles of Nuclear Magnetic Resonance Microscopy*, English. Oxford: Oxford Science Publication, 1991.

[154] R. Ernst, G. Bodenhausen, and A. Wokaun, *Principles of Nuclear Magnetic Resonance in One and Two dimensions*, EN. New York: Oxford University Press, 1987.

[155] I. Pykett, "NMR Imaging in Medicine", En, Scientific American, vol. 246, no. 5, pp. 78–88, 1982.

[156] D. McRobbie, *MRI From Picture to Proton*. Cambridge university press, 2006.

[157] I. Tkáč, Z. Starčuk, I.-Y. Choi, and R. Gruetter, "In vivo 1h NMR spectroscopy of rat brain at 1 ms echo time", en, *Magn. Reson. Med.*, vol. 41, no. 4, pp. 649–656, 1999.

[158] I. Tkáč, P. Andersen, G. Adriany, H. Merkle, K. Uğurbil, and R. Gruetter, "In vivo 1h NMR spectroscopy of the human brain at 7 T", en, *Magn. Reson. Med.*, vol. 46, no. 3, pp. 451–456, 2001.

[159] T. L. Peck, R. L. Magin, and P. C. Lauterbur, "Design and analysis of microcoils for NMR microscopy", eng, *J Magn Reson B*, vol. 108, no. 2, pp. 114–124, 1995.

[160] D. Sakellariou, G. L. Goff, and J.-F. Jacquinot, "High-resolution, high-sensitivity NMR of nanolitre anisotropic samples by coil spinning", En, *Nature*, vol. 447, no. 7145, p. 694, 2007.

[161] J. Anders, G. Chiaramonte, P. SanGiorgio, and G. Boero, "A single-chip array of NMR receivers.", eng, *J Magn Reson*, vol. 201, no. 2, pp. 239–249, 2009.

[162] J. Anders, P. SanGiorgio, and G. Boero, "A fully integrated IQ-receiver for NMR microscopy", *Journal of Magnetic Resonance*, vol. 209, no. 1, pp. 1–7, 2011.

[163] M. Grisi, G. Gualco, and G. Boero, "A broadband single-chip transceiver for multi-nuclear NMR probes", *Review of Scientific Instruments*, vol. 86, no. 4, p. 044 703, 2015.

[164] J. Anders, J. Handwerker, M. Ortmanns, and G. Boero, "A low-power high-sensitivity single-chip receiver for NMR microscopy", *Journal of Magnetic Resonance*, vol. 266, no. Supplement C, pp. 41–50, 2016.

[165] C. L. Degen, M. Poggio, H. J. Mamin, C. T. Rettner, and D. Rugar, "Nanoscale magnetic resonance imaging", en, *PNAS*, vol. 106, no. 5, pp. 1313–1317, 2009.

[166] H. J. Mamin, M. Poggio, C. L. Degen, and D. Rugar, "Nuclear magnetic resonance imaging with 90-nm resolution", En, *Nature Nanotechnology*, vol. 2, no. 5, p. 301, 2007.

[167] J. M. Boss, K. Chang, J. Armijo, K. Cujia, T. Rosskopf, J. R. Maze, and C. L. Degen, "One- and Two-Dimensional Nuclear Magnetic Resonance Spectroscopy with a Diamond Quantum Sensor", *Phys. Rev. Lett.*, vol. 116, no. 19, p. 197 601, 2016.

[168] K. Ehrmann, N. Saillen, F. Vincent, M. Stettler, M. Jordan, F. Maria Wurm, P.-A. Besse, and R. Popovic, "Microfabricated solenoids and Helmholtz coils for NMR spectroscopy of mammalian cells", en, *Lab on a Chip*, vol. 7, no. 3, pp. 373–380, 2007.

[169] B. J. Blaise, J. Giacomotto, B. Elena, M.-E. Dumas, P. Toulhoat, L. Ségalat, and L. Emsley, "Metabotyping of Caenorhabditis elegans reveals latent phenotypes", en, *PNAS*, vol. 104, no. 50, pp. 19 808–19 812, 2007.

[170] B. J. Blaise, J. Giacomotto, M. Triba, and Bénédicte Elena, "Metabolic profiling strategy of Caenorhabditis elegans by whole organism nuclear magnetic resonance", Journal of proteome research, vol. 8, pp. 2542–2550, 2009.

[171] A. Kalfe, A. Telfah, J. Lambert, and R. Hergenröder, "Looking into Living Cell Systems: Planar Waveguide Microfluidic NMR Detector for in Vitro Metabolomics of Tumor Spheroids", *Anal. Chem.*, vol. 87, no. 14, pp. 7402–7410, 2015.

[172] J. B. Aguayo, S. J. Blackband, J. Schoeniger, M. A. Mattingly, and M. Hintermann, "Nuclear magnetic resonance imaging of a single cell", En, *Nature*, vol. 322, no. 6075, p. 190, 1986.

[173] S. C. Grant, N. R. Aiken, H. D. Plant, S. Gibbs, T. H. Mareci, A. G. Webb, and S. J. Blackband, "NMR spectroscopy of single neurons", en, *Magn. Reson. Med.*, vol. 44, no. 1, pp. 19–22, 2000.

[174] S. Grant, D. Buckley, S. Gibbs, A. Webb, and S. Blackband, "MR microscopy of multicomponent diffusion in single neurons", en, *Magn. Reson. Med.*, vol. 46, no. 6, pp. 1107–1112, 2001.

[175] C. H. Lee, J. J. Flint, B. Hansen, and S. J. Blackband, "Investigation of the subcellular architecture of L7 neurons of *Aplysia californica* using magnetic resonance microscopy (MRM) at 7.8 microns", En, *Scientific Reports*, vol. 5, p. 11 147, 2015.

[176] A. Wong, X. Li, L. Molin, F. Solari, B. Elena-Herrmann, and D. Sakellariou, "High Resolution-Magic-Angle Spinning NMR Spectroscopy for Metabolic Phenotyping of Caenorhabditis elegans", *Anal. Chem.*, vol. 86, no. 12, pp. 6064–6070, 2014.

[177] Rainer Flindt, *Amazing numbers in biology*, En, ser. Life Science. Springer Science & Business Media, 2006.

[178] M. Grisi, F. Vincent, B. Volpe, R. Guidetti, N. Harris, A. Beck, and G. Boero, "NMR spectroscopy of single sub-nL ova with inductive ultra-compact single-chip probes", En, *Scientific Reports*, vol. 7, p. 44 670, 2017.

[179] K. Kratt, V. Badilita, T. Burger, J. G. Korvink, and U. Wallrabe, "A fully mems-compatible process for 3d high aspect ratio micro coils obtained with an automatic wire bonder", *Journal of Micromechanics and Microengineering*, vol. 20, no. 1, p. 015 021, 2010.

[180] R. C. Meier, J. Höfflin, V. Badilita, U. Wallrabe, and J. G. Korvink, "Microfluidic integration of wirebonded microcoils for on-chip applications in nuclear magnetic resonance", en, *J. Micromech. Microeng.*, vol. 24, no. 4, p. 045 021, 2014.

[181]   D. A. Seeber, R. L. Cooper, L. Ciobanu, and C. H. Pennington, "Design and testing of high sensitivity microreceiver coil apparatus for nuclear magnetic resonance and imaging", *Review of Scientific Instruments*, vol. 72, no. 4, pp. 2171–2179, 2001.

[182]   C. Massin, F. Vincent, A. Homsy, K. Ehrmann, G. Boero, P. .-.-A. Besse, A. Daridon, E. Verpoorte, N. F. de Rooij, and R. S. Popovic, "Planar microcoil-based microfluidic NMR probes", *Journal of Magnetic Resonance*, vol. 164, no. 2, pp. 242–255, 2003.

[183]   C. Massin, G. Boero, F. Vincent, J. Abenhaim, P. .-.-A. Besse, and R. S. Popovic, "High-Q factor RF planar microcoils for micro-scale NMR spectroscopy", *Sensors and Actuators A: Physical*, Selected papers from Eurosenors XV, vol. 97-98, no. Supplement C, pp. 280–288, 2002.

[184]   J. A. Rogers, R. J. Jackman, G. M. Whitesides, D. L. Olson, and J. V. Sweedler, "Using microcontact printing to fabricate microcoils on capillaries for high resolution proton nuclear magnetic resonance on nanoliter volumes", English, *APPL. PHYS. LETT., Applied Physics Letters Applied Physics Letters, Applied Physics Lettrs*, vol. 70, no. 18, pp. 2464–2466, 1997.

[185]   V. Demas, A. Bernhardt, V. Malba, K. L. Adams, L. Evans, C. Harvey, R. S. Maxwell, and J. L. Herberg, "Electronic characterization of lithographically patterned microcoils for high sensitivity NMR detection", *Journal of Magnetic Resonance*, vol. 200, no. 1, pp. 56–63, 2009.

[186]   V. Malba, R. Maxwell, L. B. Evans, A. F. Bernhardt, M. Cosman, and K. Yan, "Laser-Lathe Lithography—a Novel Method for Manufacturing Nuclear Magnetic Resonance Microcoils", en, *Biomedical Microdevices*, vol. 5, no. 1, pp. 21–27, 2003.

[187]   R. Kamberger, A. Moazenzadeh, J. G. Korvink, and O. G. Gruschke, "Hollow microcoils made possible with external support structures manufactured with a two-solvent process", en, *J. Micromech. Microeng.*, vol. 26, no. 6, p. 065 002, 2016.

[188]   D. I. Hoult and R. E. Richards, "The signal-to-noise ratio of the nuclear magnetic resonance experiment", *Journal of Magnetic Resonance (1969)*, vol. 24, no. 1, pp. 71–85, 1976.

[189]   D. L. Olson, T. L. Peck, and J. V. Sweedler, "High-resolution microcoil 1h-NMR for mass-limited, nanoliter-volume samples", pp. 1967–1970, 1995.

[190]   J. Bart, J. W. G. Janssen, P. J. M. van Bentum, A. P. M. Kentgens, and J. G. E. Gardeniers, "Optimization of stripline-based microfluidic chips for high-resolution NMR", *Journal of Magnetic Resonance*, vol. 201, no. 2, pp. 175–185, 2009.

[191]   N. Spengler, J. Höfflin, A. Moazenzadeh, D. Mager, N. MacKinnon, V. Badilita, U. Wallrabe, and J. G. Korvink, "Heteronuclear Micro-Helmholtz Coil Facilitates µm-Range Spatial and Sub-Hz Spectral Resolution NMR of nL-Volume Samples on Customisable Microfluidic Chips", *PLOS ONE*, vol. 11, no. 1, e0146384, 2016.

Acronyms

C. elegans	*Caenorhabditis elegans*
E. coli	*Escherichia coli*
MS	Mean Square
SS	Sum of Squares
A	adult
ADC	analog-to-digital converter
ANOVA	Analysis of Variance
CMi	EPFL Center of MicroNanoTechnology
D(L1)	diameter at L1 stage
D(L2)	diameter at L2 stage
D(L3)	diameter at L3 stage
D(L4)	diameter at L4 stage
D(YA)	diameter at YA stage
DoE	Design of Experiment
EMA	European Medicine Agency
ETC	electron transport chain
F(L1)	fluorescent signal at L1 stage
F(L2)	fluorescent signal at L2 stage
F(L3)	fluorescent signal at L3 stage
F(L4)	fluorescent signal at L4 stage
F(YA)	fluorescent signal at YA stage
GLUT4	insulin-regulated glucose transporter

Acronyms

HCA	hierarchical cluster analysis
IPA	isopropanol
ITO	indium tin oxide
L(L1)	length at L1 stage
L(L2)	length at L2 stage
L(L3)	length at L3 stage
L(L4)	length at L4 stage
L(YA)	length at YA stage
L1	larval 1
L2	larval 2
L3	larval 3
L4	larval 4
LB	luria broth
LED	light emitting diode
LPF	low pass filter
NGM	nematode growth medium
NMR	Nuclear Magnetic Resonance
NR	nicotinamide riboside
OD	optical density
PC	principal component
PCA	principal component analysis
PD	photodiode
PDMS	polydimethylsiloxane
PGMEA	propylene glycol methyl ether acetate
PID	proportional integral derivative
PMMA	polymethylmethacrylate
RNAi	RNA interference
ROI	region of interest
SBR	signal-to-background ratio
SD	standard deviation

SEM	Scanning electron microscope
t(E1)	gastrula-bean stage
t(E2)	bean-twitching stage
t(E3)	twitching-hatching stage
t(L1)	duration of L1 stage
t(L2)	duration of L2 stage
t(L3)	duration of L3 stage
t(L4)	duration of L4 stage
t(Y4)	duration of YA stage
UPR^{mt}	mitochondrial unfolded protein response
YA	young adult

Curriculum Vitae

Address   Rue de Bassenges 2,
            1024 Ecublens (VD), Switzerland
Telephone (+41) 76 775 09 75
Email   mariacristina.letizia@epfl.ch

EXPERIENCE

2014 – Present	**Research Assistant and Engineer** – Biomedical Microsystems Swiss Federal Institute of Technology, Lausanne, Switzerland Development of miniaturized medical devices for *in vivo* drug testing and longitudinal phenotyping analyses on a *C. elegans* model for metabolic assays. Development of data analysis algorithms, statistical analysis. Tutoring of intern students and younger engineers. Scientific writing in peer-review journals and oral presentations at international conferences.
2012 – 2013	**Research Internship** – Photoacoustic Medical Imaging University of Florida, Gainesville, US Design of experimental protocols to image human and animal tumor vasculature using photoacoustic microscopy.

EDUCATION

2014 – Mar 2018	**Doctor of Philosophy (Ph.D.) in Microsystems and Microelectronics** Swiss Federal Institute of Technology, Lausanne, Switzerland
2011 – 2013	**Double M.Eng. in Biomedical Engineering** Major: Electronic Technologies for Biomedical Engineering University of Florida, US, and Polytechnic University of Milan, Italy
2008 – 2011	**B.Eng. in Biomedical Engineering** Polytechnic University of Milan, Italy

TECHNICAL SKILLS

Bio-microsystems	Miniaturized drug testing devices: from fabrication to pre-clinical experiments on *C. elegans* nematodes. Development of quality-by-design protocols to test the combined effect of drugs and nutrients on the life-span extension of living organisms; high-content-phenotyping upon pharmacological and genetic cues.
Software	Matlab (adv), ImageJ, Comsol Multiphysics
Statistical Analysis environment	Matlab, Excel, GraphPad Prism
Programming languages	C/C++ Arduino IDE
Text and graphic editors	MS Office, LATEX, Adobe Illustrator

LANGUAGE SKILLS

Italian	Native language
English	Full professional proficiency, abroad since 2012 – C2
French	Professional working proficiency – B1/B2

HONORS AND AWARDS

June 2012	Double Degree scholarship, awarded by Polytechnic University of Milan to 3 best Biomedical Engineering students, to obtain an additional master degree in US
November 2017	Art in Science Award, by NIST and Lab on a Chip Journal
December 2017	Best Poster Award, by Doctoral School in Microsystems, EPFL

PERSONAL HIGHLIGHTS

Leisure activities	Middle-distance runner (competition level); Culture of soil and aquatic plants, cooking and travelling
Bio-sketch	Italian citizenship, B permit, driving license

List of Publications

Journal papers

- **M. C. Letizia**, M. Cornaglia, R. Trouillon, V. Sorrentino, L. Mouchiroud, M. S. B. Sleiman, J. Auwerx and M. A. M. Gijs, "Microfluidics-enabled phenotyping of a whole population of *C. elegans* worms over their embryonic and post-embryonic development at single-organism resolution", *Microsystems and Nanoengineering*, manuscript accepted.
- **M. C. Letizia**, M. Cornaglia, G. Tranchida, R. Trouillon, M. A. M. Gijs, "Design of experiment approach for efficient multi-parametric drug testing using a *Caenorhabditis elegans* model", *Integr. Biol.*, Issue 10, p. 48-56, 2018.
- **M. C. Letizia**, P. G. Testa and M. A. M. Gijs, "Monitoring bacterial concentrations in micro-chambers by optical absorbance measurements", Manuscript in preparation.
- R. Trouillon, **M. C. Letizia**, K. J. Menzies, L. Mouchiroud, J. Auwerx, K. Schoonjans and M. A. Gijs, "A multiscale study of the role of dynamin in the regulation of glucose uptake", en, *Integr. Biol.*, Issue 9, p. 810-819, 2017.
- E. Montinaro, M. Grisi, **M. C. Letizia**, L. Pethö, M. A. M. Gijs, R. Guidetti, J. Michler, J. Brugger and G. Boero "3D-printed microchannel for sub-nL NMR spectroscopy", en, *PLOS ONE*, manuscript accepted.

Conference contributions

- **M. C. Letizia** and M. A. M. Gijs, "Accurate quantification of bacteria concentration as a nutrient for *C. elegans* worm culture on chip", 19th Edition of Nano Bio Tech, Montreux, Switzerland, November 2015.
  Oral and **poster** presentation
- **M. C. Letizia**, M. Cornaglia, M. A. M. Gijs, "Integrated temperature control system for microfluidic culture of nematodes". Proc. of 5th Micro and Nano Flows Conference (MNF2016), Milan, Italy, September 2016.
  Oral presentation
- **M. C. Letizia**, M. Cornaglia, V. Sorrentino, J. Auwerx and M. A. M. Gijs,

"A microfluidic platform for an automated monitoring of *C. elegans* embryo-to-adulthood development at single organism resolution". Proc. of 20th International Conference on Miniaturized Systems for Chemistry and Life Sciences (microTAS 2016), Dublin, Ireland, October 2016.
Oral presentation

- R. Trouillon, **M. C. Letizia**, M. A. M. Gijs, "Assessing electrochemically the chemical activity of cells in a cells-on-paper system". Proc. of 20th International Conference on Miniaturized Systems for Chemistry and Life Sciences (microTAS 2016), Dublin, Ireland, October 2016.
  Oral presentation

- E. Montinaro, M. Grisi, **M. C. Letizia**, M. A. M. Gijs, J. Brugger, G. Boero, "Nuclear magnetic resonance spectroscopy of subnanoliter samples by single chip detector and microfluidic channels". Symposium LATSIS, Lausanne, November 2016.
  Poster presentation

- **M. C. Letizia**, M. Cornaglia, R. Trouillon, M. A. M. Gijs, "Microfluidic high-content screening in a *C. elegans* model at single animal-resolution". Proc. of 39th International Conference of the IEEE Engineering in Medicine and Biology Society (EMBC2017), Jeju Island, Korea, July 2017.
  Oral presentation and **poster** presentation

- R. Trouillon, **M. C. Letizia**, M. A. M. Gijs, "Quantitative analysis of chemical release and uptake in cells-on-paper microsystems". Proc. of 39th International Conference of the IEEE Engineering in Medicine and Biology Society (EMBC2017), Jeju Island, Korea, July 2017.
  Oral presentation and **poster** presentation

- **M. C. Letizia**, P. G. Testa and M. A. M. Gijs, "Bacterial feeding control system for on-chip culture of the nematode *Caenorhabditis elegans*". Proc. of 21th International Conference on Miniaturized Systems for Chemistry and Life Sciences (microTAS 2017), Savannah, Georgia, US, November 2017.
  Poster presentation.